3-21-2013

Neutron Spectroscopy Using LiF Thin-Film Detectors

Michael A. Ford

NEUTRON SPECTROSCOPY USING LiF THIN-FILM DETECTORS

THESIS

Michael A. Ford, Second Lieutenant, USAF

AFIT-ENP-13-M-10

DEPARTMENT OF THE AIR FORCE
AIR UNIVERSITY

AIR FORCE INSTITUTE OF TECHNOLOGY

Wright-Patterson Air Force Base, Ohio

AFIT-ENP-13-M-10

NEUTRON SPECTROSCOPY USING LiF THIN-FILM DETECTORS

THESIS

Presented to the Faculty

Department of Engineering Physics

Graduate School of Engineering and Management

Air Force Institute of Technology

Air University

Air Education and Training Command

in Partial Fulfillment of the Requirements for the

Degree of Master of Science in Nuclear Engineering

Michael A. Ford, BS

Second Lieutenant, USAF

March 2013

AFIT-ENP-13-M-10

NEUTRON SPECTROSCOPY USING LiF THIN-FILM DETECTORS

Michael A. Ford, BS
Second Lieutenant, USAF

Approved:

LTC Stephen R. McHale (Chairman)	Date
John W. McClory, PhD (Member)	Date
Justin A. Clinton, PhD (Member)	Date

Abstract

A stacked array of segmented micro-structured semiconductor neutron detectors (MSNDs) has been fabricated to perform as a neutron spectrometer simultaneously capable of differentiating fast and thermal neutrons. The MSND devices consist of thin-film perforated diodes constructed from LiF powder back-filled into an etched silicon wafer. Geant4 simulations demonstrate than an eight-layer spectrometer consisting of alternating layers of MSND and hydrogenous moderator can successfully resolve neutron energies at a resolution dependent upon the number of layers and the thickness of the adjacent moderating materials. The simulated spectrometer response was compared to that obtained experimentally with mono-energetic neutrons from a D+D neutron generator. The commissioning tests of the spectrometer reveal that the energy of a mono-energetic neutron source can be identified to within ± 1 MeV. Following the commissioning tests, the spectrometer was used to characterize the poly-energetic neutron spectrum of a plutonium-beryllium neutron source.

Acknowledgements

I would first like to thank my wife for being supportive through all the late nights and countless hours of research. She has been my rock throughout my enlisted career, undergraduate studies, officer training school and now graduate school- pulling me away from studies when I needed a break and commandeering the duties around the house when I didn't have the time.

I would next like to thank my family for the encouragement and positive perspective over the past 18 months. I would especially like to thank my daughter, who was born a few months ago on September 21, 2012, for her endless smiles as I walk into the house; she has lifted my spirits in so many ways.

I would also like to thank my research advisor, LTC Stephen McHale, for his constant praise and confidence in me. This confidence has made me a stronger person and a better researcher. His door is always open and his motivation is inspiring.

Likewise I extend my thanks to my thesis committee members, Drs Justin Clinton and John McClory. The early mornings and late nights with Dr. Clinton (and a cup of coffee) at the neutron generator have been fun and the committee meetings have always steered to me in the right direction when I was unsure.

Lastly, I would like to thank all of my classmates here at AFIT. The last year and a half has been better because of the camaraderie and support amongst the group; the time has flown by but I will always remember it. Thank you.

Michael A. Ford

Table of Contents

Page

List of Figures

List of Tables

NEUTRON SPECTROSCOPY USING LiF THIN-FILM DETECTORS

I. Introduction

1.1 Motivation

The growth of nuclear technology on a global scale has created an emphasis for increased nuclear detection capabilities within the United States. The production and application of special nuclear material (SNM), in a weapon or otherwise, requires transportation of the materials. The transportation of SNM is often a vulnerable phase for a nation that is trying to displace the materials without being detected. Whether it is an enemy transporting a weapon to the United States or a nation trying to acquire SNM for development of a weapon, the need for detection prior to detonation is a growing concern for homeland security [4, 5].

The threat is well understood; however, countering the threat is a complex endeavor. The Defense Threat Reduction Agency (DTRA) is the U.S. Department of Defense's official Combat Support Agency for countering weapons of mass destruction; they place an emphasis on improving technical capabilities to include expanding the range of nuclear detection from several yards to stand-off distances in order to locate, track or interdict nuclear weapons and materials in the hands of adversaries [4]. Many new detection systems are a result of DTRA sponsored research.

> Today, the Cold War has disappeared but thousands of those weapons have not. In a strange turn of history, the threat of global nuclear war has gone down, but the risk of a nuclear attack has gone up. More nations have acquired these weapons. Testing has continued. Black market trade in nuclear secrets and nuclear materials abound. The technology to build a

> bomb has spread. Terrorists are determined to buy, build or steal one. Our efforts to contain these dangers are centered on a global non-proliferation regime, but as more people and nations break the rules, we could reach the point where the center cannot hold. [Speech delivered by president Barack Obama in Prague, Czech Republic, April, 2009] [4]

This quote is indicative of the importance placed on nuclear deterrence in the United States. While there is less effort directed to the conception of nuclear weapons; defending the nation against the nuclear threat is important as ever. Additionally, according to the May 2011 Department of Homeland Security report 'A National Strategy for CBRNE Standards', there is no greater danger to the nation than a terrorist attack with a weapon of mass destruction. A quote from the report underlines this importance:

> The threats are myriad: the 1995 Tokyo subway sarin attacks, the bacillus anthracis attacks of 2001, multiple ricin toxin mailings, concerns about unguarded nuclear and radiological material worldwide, and the attempted New York City Times Square bombing of 2010. The response to these threats has been robust– all levels of government have come together to coordinate and define capabilities from detection through response. [5]

The government placing a high value on deterrence and non-proliferation is essential for the safeguard of the U.S. and its allies.

1.2 Special Nuclear Material Detection

Many challenges exist in the detection of SNM. The detection distance, or proximity of the detector to the SNM can be a challenge because of a decrease in signature as distance from the material is increased. Attenuation in matter, such as materials that comprise shipping containers, exacerbates the problem. Next, the background signals can prove to further complicate an already complicated problem of identifying

SNM, which has predominantly low intrinsic activity. Background signals are a problem because they decrease the signal-to-noise ratio. Cosmic-ray induced spallation neutron background is a significant problem and is due to the cosmic ray interactions with the air and ground. This background is on the order of ≈120-150 neutrons/m^{2}s and sometimes dominates the SNM signature [3].

Special nuclear materials of interest to the U.S. Department of Homeland Security are specific isotopes of uranium and plutonium. In particular, the interest is in materials that could be used to construct a nuclear weapon, commonly uranium-235 (^{235}U) and plutonium-239 (^{239}Pu). ^{235}U is an isotope of uranium, making up about 0.72% of natural uranium. Unlike the predominant isotope (^{238}U), ^{235}U is fissile and also the only primordial isotope. ^{239}Pu is another commonly used fissile isotope, however, it is not found in nature and must be synthesized. ^{239}Pu is typically created in nuclear reactors by transmutation of individual atoms of one of the uranium isotopes. The capture of a neutron by ^{238}U creates ^{239}U, which rapidly undergoes two beta decays:

$$^{238}_{92}\mathrm{U} + ^{1}_{0}\mathrm{n} \longrightarrow ^{239}_{92}\mathrm{U} \xrightarrow[23.5min]{\beta^-} ^{239}_{93}\mathrm{Np} \xrightarrow[2.35d]{\beta^-} ^{239}_{94}\mathrm{Pu} \quad (1)$$

producing ^{239}Pu, which can then become ^{240}Pu via neutron absorption or ^{241}Pu via successive neutron absorptions. Although the SNM of interest for weapons production is ^{239}Pu, the spontaneous fission rate is often too low for this isotope to be detected from only its neutron emission. An appreciable amount of the ^{240}Pu isotope must be present in the plutonium sample for it to be detectable via spontaneous neutron emission as the neutron emission rate is ≈70,000 times larger for ^{240}Pu than it is for ^{239}Pu.

Detection typically boils down to targeting a unique signature of the material, acquiring particles via an interaction with the detector material, then collecting the resulting electrons (or photons) and measuring the amplitudes or timing properties

of the signal to determine the type and/or amount of radiation present. With this in mind, and considering that the primary decay mode of the aforementioned isotopes is α-decay (alpha decay)[6], one would immediately consider the α-particles for the primary detection mechanism. The range of the α-particles, however, is a severe limiting factor and does not permit α-particles to be an effective SNM signature. The Bethe-Bloch equation provides a theoretical relationship between range and energy and is obtained from a quantum mechanical calculation of the collision process as a result of the Coulombic force, which has an infinite range. The calculation gives the magnitude of the energy loss per unit length, also known as the stopping power [7]. In the low-energy regime ($v^2 \ll c^2$), the stopping power is determined as:

$$\frac{d\mathrm{E}}{dx} = \frac{4\pi n z^2}{m_e v^2}\left(\frac{e^2}{4\pi\epsilon_0}\right)^2\left[\ln\left(\frac{2m_e v^2}{I}\right)\right]. \tag{2}$$

Where:

v is the velocity of the α-particle,

E is the energy of the α-particle,

x is the distance traveled,

z is the charge of the particle,

e is the electron charge,

m_e is the rest mass of the electron,

n is the electron density of the target,

I is the mean excitation potential of the target and

ϵ_0 is the vacuum permittivity.

The reciprocal of stopping power gives the distance travelled per unit of energy loss so that range can be calculated by integrating the inverse of Equation (2) over the energies of the particle:

$$R = \int_T^0 \left(-\frac{d\mathrm{E}}{dx}\right)^{-1} d\mathrm{E}. \tag{3}$$

Equation (3) can be used to determine that the 4.68 MeV α particle, resulting from the primary decay α of ^{235}U with an energy of approximately 4.68 MeV, will travel an average of only 3.18 cm in air. Using the Bragg-Kleeman rule [7]:

$$\frac{R_1}{R_0} \cong \frac{\rho_0\sqrt{A_1}}{\rho_1\sqrt{A_0}} \tag{4}$$

where R is the range in a specific medium, ρ the density and A the atomic weight; the range in a common material, aluminum for example (with ρ=2.70 g/cm^3 and atomic mass of 26.98 g/mol), is calculated as 9.6 μm for the 4.68 MeV α-particle. The particles can be easily stopped with common shielding materials and are hence not a good mechanism for detecting the SNM.

The next feasible option would be to consider the photons released from the SNM. There are several discrete energy γ-rays (gamma-rays) emitted from both plutonium and uranium; however, there are also prominent problems associated with their detection. According to the National Nuclear Data Center (NNDC), γ-rays in the ranges of $\approx$13-440 and 10-400 keV are emitted in the decay of ^{235}U and ^{239}Pu, respectively [8]. Gamma-rays interact with matter primarily through three processes: photoelectric absorption, Compton scattering and pair production. The energy ranges of the γ-rays from uranium and plutonium decays indicate that the prevalent photon interaction mechanisms are photoelectric effect and Compton scattering [7]. In the photoelectric effect, a photon is absorbed by an atom and one of the atomic electrons is released. Compton scattering is the process by which a photon scatters from a nearly free atomic electron, resulting in a less energetic photon and a scattered electron carrying the energy lost by the photon [7]. These interactions cause an exponential decrease in the amount of γ-rays that can penetrate a shielding material. A photon undergoing photoelectric absorption will disappear while the Compton scattered γ-rays will scatter until their energies are low enough to be absorbed as well. A photon mass at-

tenuation coefficient (μ/ρ) dictates the attenuation of the γ-rays via the exponential attenuation law and is dependent upon photon energy and the density of the absorber material. The exponential attenuation law is:

$$I(x,i) = I_0 e^{-(\mu_i/\rho)\rho x} \tag{5}$$

Where I_0 is the incident number of particles in the i^{th} energy group of a narrow beam of photons penetrating a material with thickness x and density ρ. The resultant beam of photons will have I particles in the i^{th} energy group. The attenuation coefficients are well known and tabulated on the National Institute of Standards and Technology (NIST) website [9]. Considering 400 keV γ-rays and an attenuation coefficient from NIST, it can be calculated that over 99% of the γ-rays will be attenuated with less than 3 cm of aluminum shielding. The ease of shielding the γ-rays in addition to the high background levels of γ-radiation makes photons inadequate for long-range detection of SNM.

Electrons were also considered for the detection of SNM, however, problems similar to both the α-particles and γ-rays are shown to exist. Electrons interact through Coulomb scattering from atomic electrons just like alpha particles; however, there are several important distinctions. Electrons, primarily those emitted in β-decay, travel at relativistic speeds. The electrons will also suffer large deflections in collisions with other electrons causing them to follow chaotic paths [7]. A common pair of fission fragments from the fission of ^{235}U is xenon-140 and strontium-94. Xenon-140 has a 100% β^- decay branch ratio with a Q-value of 4060 keV. Considering a highly probable β-particle of 2632 keV penetrating aluminum with a density of 2.70 g/cm^3, the average range is only 4.77 mm. While the range is significantly larger than that of alpha particles, the radiative energy loss and scattering cause them to be easily shielded.

Table 1. Selected properties of common special nuclear material. Adapted from McHale [3].

Isotope	Half Life [years]	Primary Decay Mode	Spontaneous Fission Neutron Emission Rate[1] [n/kg-sec]
^{235}U	7.0 x 10^{8}	α	1.04 x 10^{-2}
^{238}U	4.5 x 10^{9}	α	12.6
^{239}Pu	2.4 x 10^{4}	α	19.9
^{240}Pu	6.5 x 10^{3}	α	1.38 x 10^{6}
^{241}Pu	14.4	α	2.20 x 10^{2}

The next, and arguably the last option for long range SNM detection, is to detect neutrons from uranium and plutonium. Referencing Table 1, it can be seen that the rate of spontaneous fission differs significantly among these isotopes. Neutrons can also be released as a result of active interrogation, where neutrons are intentionally ejected toward a target with the intention of inducing fission. Neutrons, because of their charge neutrality, do not undergo the same Coulombic interaction that α-particles and electrons endure. Neutrons lose energy primarily via elastic scattering from collisions with other nuclei (not the electrons). As a result, neutrons penetrate much larger distances. This penetration is valuable as it allows SNM detection at longer ranges; however, it has a side effect of creating low probability of interaction, including in the materials that detect the neutrons. Cross sections are important to consider whenever dealing with neutron interactions. Roughly speaking, the cross section is a measure of the relative probability for a reaction to occur; specific materials with high neutron capture cross sections can be used to efficiently detect neutrons. There are few of these materials and the most common in use today are particular isotopes of gadolinium, boron and lithium. The energy dependent cross sections for each of these materials are shown in Fig. 1. The thermal neutron capture cross sections

[1]Based upon average neutrons per fission of 2.44 and 2.89 for uranium and plutonium, respectively [10].

of lithium, boron and gadolinium are orders of magnitude higher than most other elements. For comparison purposes, the neutron capture cross sections of silicon-28 are also shown in Fig. 1. Each of the neutron detector materials has its own advantages and disadvantages, which will be discussed in this report in addition to the methods for detecting neutrons and the identification of their energy using neutron spectroscopy.

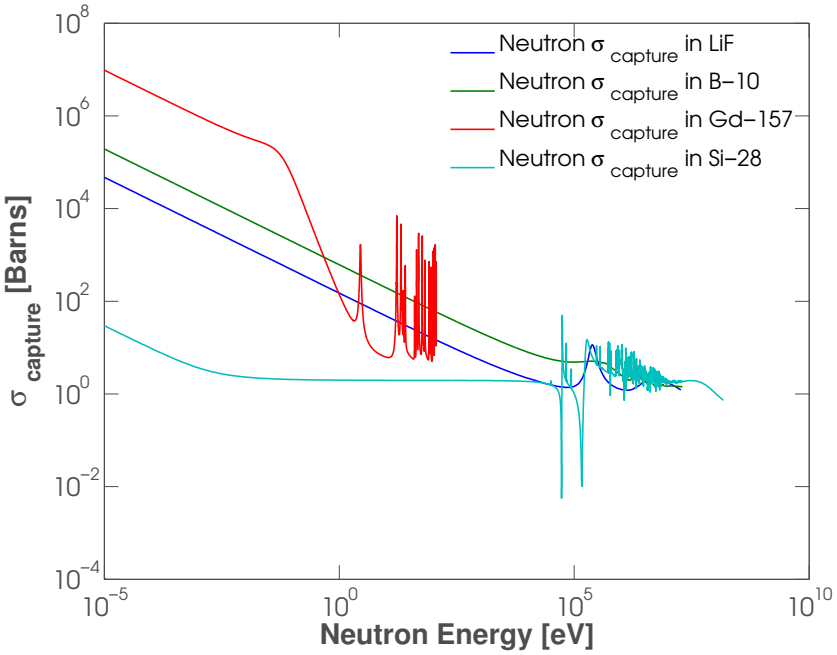

Figure 1. The energy dependent neutron capture cross sections of LiF, ^{10}B, ^{157}Gd and ^{28}Si. Compared to the thermal energy neutron absorption cross section data of silicon, the σ_{capture} are orders of magnitude higher in the lithium, boron and gadolinium.

A neutron spectrometer has been developed using lithium fluoride semiconductor detectors. Neutron spectroscopy using lithium fluoride thin-film perforated semiconductor neutron detectors has potential to aid in the detection of SNM. LiF detectors are robust and can be produced very inexpensively, enabling installation within shipping vessels for possible detection of neutron-emitting materials. The spectrometer is composed of alternating layers of hydrogenated neutron moderator and neutron-reactive LiF semiconductor wafer detectors. The spectrometer works on the idea

that if one has a detector to observe neutrons of a particular energy (in this case, thermal), and a moderating material that decelerates neutrons in a known fashion then a combination of the detectors and moderating material is sufficient to detect neutrons and characterize their energy, possibly identifying the neutron source. Neutron detection has historically been accomplished primarily using highly pressurized gas tubes and organic scintillators, both of which are reliable methods still in use today that are applicable to unique situations. ^{3}He has previously been a pioneer material in the field of neutron detection, however, recent shortages in the supply of ^{3}He have led to rationing of this isotope and reinvigorated research in alternative technologies for neutron detection [11]. Accordingly, solid state detectors have been a focal point of this research because of their higher densities and will be discussed in detail throughout this document. The development of a spectrometer utilizing solid state LiF semiconductor detectors for identification and classification of neutron sources was the end state of this research; the fabrication, testing and conclusions of the research will be discussed herein. The next chapter will discuss previous studies that have been accomplished in the field of neutron detection and spectroscopy.

II. Previous Studies

Over the past several decades, many researchers have examined the area of neutron detection and spectroscopy. Because neutrons produce no direct ionization events, neutron detectors must be based on detecting the secondary events produced by nuclear reactions such as (n,p), (n,α), (n,γ), (n,fission), or by nuclear scattering from light charged particles, which are then detected [7]. The secondary event is necessary to create a prompt charged particle(s) (or photon) such as a proton, α-particle, etc., which can be read out via front-end electronics and processed as a signal. A variety of methods have been operative such as: gaseous detectors, scintillation detectors and semiconductor detectors. When determining the technology to use for a neutron detector, several factors must be considered. First, the cross section must be as large as possible so that efficient detectors can be built with reasonable dimensions. This is particularly important for gas detectors which typically employ large detection volumes with tubes extending upwards of 30 cm in length. For the same reason, the target nuclide should be of high isotopic abundance in the natural element, or alternatively, an economical source of artificially enriched samples should be available for detector fabrication [12]. In many applications, intense fields of γ-rays are also found with neutrons and the choice of reaction relies on the ability to discriminate against these γ-ray interactions in the detection process. Of principle importance here is the Q-value of the reaction that determines the energy liberated in the reaction following neutron capture [12]. One typically looks for reactions with higher Q-values (MeV range) to assist in the discrimination from γ-ray events using only amplitude discrimination. Below is a short summary of the many methods that have been used to detect neutrons. An emphasis has been placed on slow neutrons with energies below the cadmium cutoff of $\approx$0.5 eV. Subsequently, the current research employing the neutron detectors in spectroscopy will be reviewed.

2.1 Gaseous Detectors

Gaseous boron trifluoride (BF_3) detectors have been widely used for detection of slow neutrons. Boron trifluoride serves as both a target for slow neutrons and also as a proportional gas in the detector. In nearly all commercial detectors, the gas is highly enriched in ^{10}B resulting in an efficiency up to five times greater than if the gas contained only naturally occurring boron [12]. The detection efficiency for a 30 cm long BF_3 tube (96% enriched in ^{10}B) filled to 80 kPa is upwards of 90% at thermal neutron energies, but drops down to 3.6% at 100 eV. A very important consideration in many application of BF_3 tubes has been their ability to discriminate against γ-rays. Gamma-rays interacting primarily with the walls of the counter create secondary electrons that may produce ionization in the gas. Typically, this effect is easy to discriminate in low flux γ-ray environments because the stopping power for electrons in the gas is quite low, and the electrons only deposit a fraction of their energy before reaching the opposite wall. In high flux γ-ray environments, however, the problem is not so trivial; charge pile-up and even degradation of the gas has shown to exist in very high flux γ-ray environments [12].

^3He has also been used as a detection gas. ^3He has a cross section that is $\approx$1.39 times larger than that of boron and can be operated at much higher pressures than BF_3. ^3He is preferred over BF_3 with respect to achieving the highest detection efficiency; however, this gas is nearly impossible to purchase and is under very strict ration. It is, therefore, a less viable option for the military or otherwise.

2.2 Scintillators

A disadvantage of gaseous detectors is that the point of interaction cannot be known more precisely than 'somewhere in the tube'. In addition, typical pulse heights will have rise times that vary by as much as 3-5 μs [12]. Typical tubes are as much

as 10-30 cm long in order to provide reasonable detection efficiency and therefore the path length uncertainties can be large. The limitations of gaseous detectors have been largely circumvented using scintillators. Scintillators made by fusing B_2O_3 and ZnS have found wide application in neutron time-of-flight measurements [12]. These scintillators are usually kept quite thin at 1-2 mm due to the relative opaqueness of this material to its own scintillation light and also to minimize path length uncertainty. A large problem is that these scintillators are much less effective in γ-ray background discrimination compared with BF_3 tubes. Photon production as a result of secondary electrons from γ-ray interactions is difficult to discriminate from the photon production as a result of the neutron interactions. Amplitude discrimination is no longer sufficient and pulse shape discrimination must be employed [13].

While a lithium equivalent of the BF_3 tube is not available because a stable lithium-containing proportional gas does not exist, lithium has been very successful as a scintillating material. A common application has been in the form of crystalline lithium iodide because of its chemical similarity to sodium iodide [12]. While highly hygroscopic, a solution has been to keep it contained in hermetically sealed cans with a thin optical window. The high density of the material means that crystal sizes need not be very large for very efficient slow neutron detection. In fact, a 1 cm thick crystal prepared from highly enriched ^{6}LiI is nearly 100% efficient in capturing slow neutrons though the Cd cutoff [12].

Scintillation materials for neutron detection have been somewhat of a highlight for the past two decades. Vast research has been done with each of the materials previously highlighted (Li, B and Gd) [14, 13, 15, 16]. Recent studies with gadolinium aimed at loading plastic with Gd containing additives have been successful, despite the discrimination sensitivities [16]. The aim was in developing inexpensive and efficient thermal neutron detectors with low γ-ray sensitivity that can be produced in large (or

complex) arrays. The study concluded with a metallo-organic compound gadolinium isopropoxide used as an additive to synthesize polystyrene-based plastic scintillators with a relative light output of 76% transmissivity with only 3% Gd (by weight). A 13 mm thick scintillator loaded with 0.5% Gd detects approximately 46% of thermal neutrons that enter the detector volume [16].

2.3 Neutron-Induced Fission Detectors

The fission cross sections of ^{233}U, ^{235}U and ^{239}Pu are relatively large at low neutron energies and thus these materials can be used as the basis of slow neutron detectors [12]. One characteristic that stands out with fission detectors is the uniquely high Q-value of ≈ 200 MeV, relieving many of the discrimination issues prevalent with other neutron detectors. Neutron-induced fission detectors are often ionization chambers with their inner surfaces coated with a fissile deposit, and the dimensions of the counters tend to be similar to those of α-particle detectors (the average range of the fission fragments are approximately half the range of a 5 MeV α-particle). The two fission fragments are always oppositely directed for slow-neutron-induced fission, and therefore detectors with a solid coating of fissionable material will respond only to the single fragment that is directed toward the active volume of the chamber [12]. Some fission counters have been built with extremely thin backing material underneath a thin fissile deposit so that both of the fission fragments can be detected, however, the very thin supports required for the fissile deposits are quite fragile and consequently, this type of fission chamber is not widely used in routine neutron detection applications [12]. Problems have also been discovered with charge pile-up as a result of the primary α-decay with the fissionable materials used in the detectors.

2.4 Activation Detectors

The concept behind activation neutron detection is the use of induced activity in one of more specially chosen materials to infer the neutron flux and energy spectrum at a particular location. Activation detection has the advantages of low cost, superior physical form and ease of calibration. It is possible to find materials with linear response even to very high rates of fusion and fission reactions. This method has the primary disadvantage of being both passive and inactive; the foils must be manually checked and measured, creating a logistical nightmare in a fast-paced and incessant atmosphere of some shipping ports where their use is highly applicable.

2.5 Proton Recoil Instruments

The proton recoil method works by measuring the energy and direction of protons that have been recoiled by a neutron (generally higher energy neutrons). The material in which the recoiling takes place is typically a thin layer of hydrogenous substance. The relative accuracy with which the recoiled proton properties can be measured allows an acquisition of high resolution neutron spectra over a wide energy range. Resolutions of 1-3% are typical for 14.1 MeV neutrons [12]. Also, energies from below 1 MeV up to more than 1 GeV have been measured. The short range of the recoiled protons and the need for higher resolutions limit the possible recoil material thickness and thus reduce the detection efficiency.

2.6 Moderating Detectors

Moderating detectors work by utilizing a moderator to slow neutrons down to a region where they can be more efficiently detected using conventional methods. Hydrogen rich materials such as paraffin or polyethylene typically surround the detector.

The slow neutron detector is frequently a BF_3 or ^3He tube, ^6Li doped scintillator or, as used for the basis of this report, a thin-film solid-state semiconductor detector. The Bonner Sphere is a well-known moderating detector.

2.7 Thin-Film Semiconductor Detectors

Semiconductor detectors, in their most basic application consist of a planar diode supplemented with a neutron conversion layer that has been deposited on its surface. Neutrons are captured in the converter and secondary particles are produced. The secondary charged particles create electron-hole pairs in the diode that are swept to the surface of the diode and collected as a current. A limitation to the semiconductor detector is that the efficiency depends on the thickness of the conversion layer, however, if made too thick, the conversion layer may not allow the changed particles to escape into the semiconductor to create the electron-hole pairs [17, 12]. Figure 2 shows the basic geometry of a thin-film semiconductor detector with annotation of a neutron interaction in the thin-film.

Significant research has been conducted to improve the geometry of the semiconductor thin-film detector in order to improve the neutron detection efficiency. Several aspects of the semiconductor detector make it desirable, hence motivating the broad range of research being conducted. They can be built very inexpensively and be mass produced, have very low power requirements, can be built to virtually any size and are extremely rugged.

The basic configuration consists of a common Schottky barrier or p-n junction diode, upon which any of the aforementioned neutron reactive coatings is applied [18]. The current restriction to the wide-spread use of these devices is the sub-par efficiency compared to the many alternatives listed above such as scintillation detectors and gas tubes. Material choice requires a strong neutron absorbing reactive

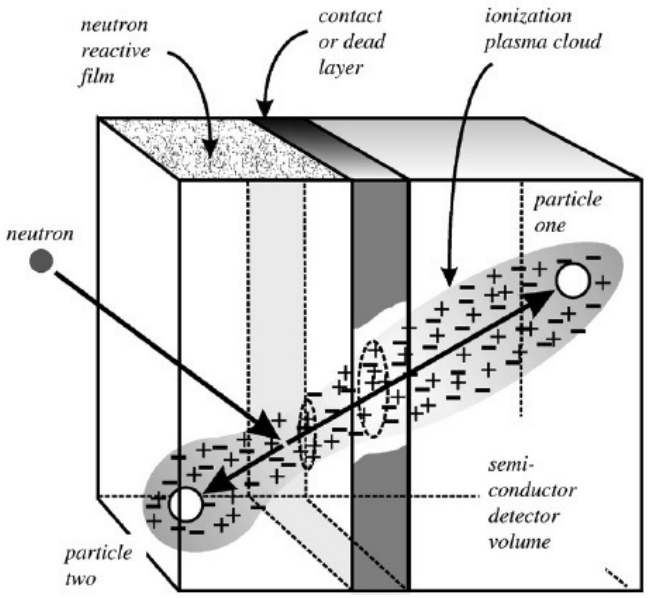

Figure 2. The fundamental approach to a thin-film coated semiconductor neutron detector. The film thickness should not exceed the maximum range of the 'long-range' reaction product. The reaction products are emitted in opposite directions [17]. ©2003 with permission from Elsevier.

coating that emits ionizing reaction products, preferably charged particles rather than photons [18]. Some attractive materials that have been examined for solid state neutron detection include gadolinium, boron and lithium. The thermal neutron (v=2200 m/s) capture cross section for ^{157}Gd is 240,000 barns, for ^{10}B the cross section is 3840 barns and for ^{6}Li, the thermal neutron absorption cross section is 940 barns.

Thin-Film Conversion Materials.

Several materials have been explored as thin-film neutron conversion layer materials. The thermal neutron capture cross section for ^{157}Gd is 240,000 barns. This allows for efficient absorption of thermal neutrons in a thin-film of material. Unfortunately, gadolinium has the side effect of producing low energy internal conversion electrons, as well as a cascade of associated Auger electrons, x-rays and γ-rays ranging in energy

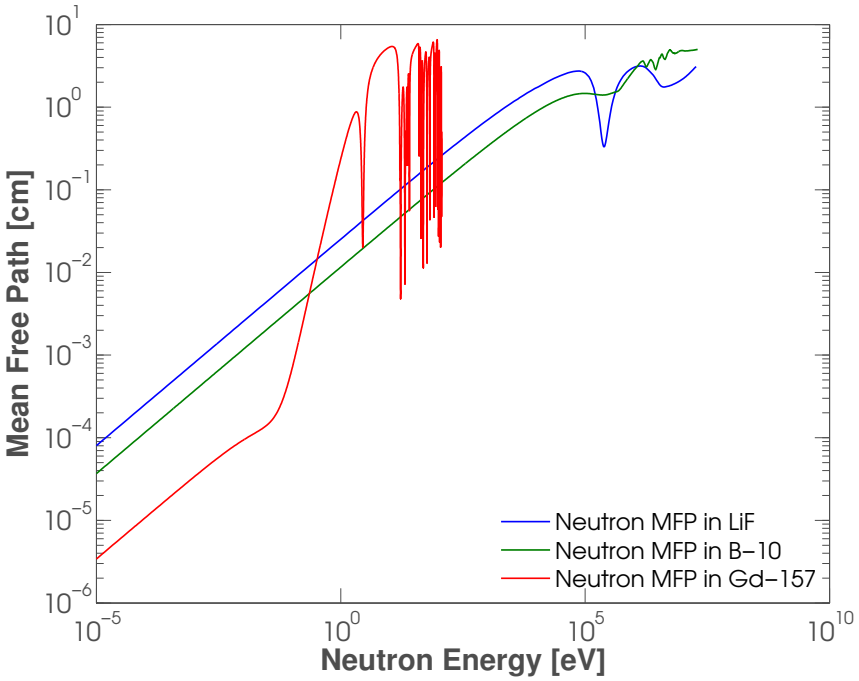

Figure 3. The mean free path (mfp) of neutrons in ^{157}Gd, ^{10}B and LiF. As the neutron's energy is increased, the mean free path is larger. At high energies, it becomes increasingly probable that the neutron will pass directly through the thin-film and not be detected.

from a few eV to several MeV making it almost impossible to discern a neutron event from background [16]. Boron, as a more practical substitution for gadolinium has also been applied to semiconductor detectors; the thermal neutron absorption cross section is not as high, but still respectable at 3840 barns. Boron has been used for decades with great success; however, the charged particles emitted from the ${}^{1}_{0}\mathrm{n}+{}^{10}_{5}\mathrm{B}$ reaction are lower energy than those emitted from the ${}^{1}_{0}\mathrm{n}+{}^{6}_{3}\mathrm{Li}$ reaction (and there are two reaction paths in boron, whereas there is only a single reaction in lithium). The energy dependent mean free path in each material is shown in Fig. 3. The mean-free-path (mfp) has many qualitative applications in detectors, for example, if the mfp of the neutrons is long compared to the dimensions of the sample (or thin-film in this case), it is likely that most will escape from the sample. This is an important concept in a spectrometer in relation to the thermalization of neutrons and will be discussed

later in more detail. Notice that the mfp is lowest in gadolinium, as expected, due to the significantly larger cross sections. This document will focus on the use of a ^{6}Li containing neutron conversion layer, which has a cross section of 940 barns and just one neutron reaction branch. A brief description of the three most common reaction materials follows.

Gadolinium.

Gadolinium is a naturally occurring element which has two isotopes with very high thermal neutron cross-sections: ^{155}Gd (14.7% natural abundance) and ^{157}Gd (15.7% natural abundance) with 6.1x10^{4} barns and 2.6x10^{5} barns, respectively [16]. These cross sections are higher than every other isotope, which makes gadolinium an attractive material for a variety of neutron detectors. In a solid state neutron detector, one large disadvantage of gadolinium is that the absorption of a thermal neutron results in the emission of low energy internal conversion electrons, Auger electrons and an array of gamma and x-rays. Unfortunately, a majority of the products are on the low-energy end of the spectrum (below 70 keV) or high energy γ-rays, which can be easily confused with background γ-rays or escape the detector without interacting in the semiconductor. If the reaction products do not interact in the semiconductor, a current is not produced and no reaction is signaled. For this reason, gadolinium coatings are generally not used as a converter for coated semiconductor neutron detectors [18].

Boron.

The ^{10}B(n,α)^{7}Li neutron reaction yields two possible decay branches from the excited ^{11}B compound nucleus:

$$ {}^{1}_{0}\mathrm{n} + {}^{10}_{5}B \longrightarrow \begin{cases} {}^{7}_{3}\mathrm{Li}^{*}(1.4721\mathrm{MeV}) + {}^{4}_{2}\mathrm{He}(0.8398\mathrm{MeV}) & (93.7\%) \\ {}^{7}_{3}\mathrm{Li}(1.7762\mathrm{MeV}) + {}^{4}_{2}\mathrm{He}(1.0133\mathrm{MeV}) & (6.3\%) \end{cases} $$

where the Li ion in the 94% branch is ejected in an excited state and normally de-excites through the emission of a 480 keV γ-ray [18]. In either case, the Q-value of the reaction for thermal neutron interactions is very large (2.310 or 2.792 MeV) compared with the incoming energy of the neutron. Thus, the incoming kinetic energy of the neutron is convoluted in the much larger reaction energy and it is impossible to extract any information about the initial neutron energy [12]. Also, because the incoming linear momentum is very small, the reaction products must have a net momentum of near zero. As a consequence of this, the reaction products are ejected in opposite directions with the energy of the reaction shared between them. This is demonstrated via the following equations (for the 93.7% reaction):

$$E_{\mathrm{Li}} + E_{\alpha} = Q = 2.31\mathrm{MeV} \tag{6}$$

and

$$m_{\mathrm{Li}}\nu_{\mathrm{Li}} = m_{\alpha}\nu_{\alpha}. \tag{7}$$

Using the basic equation for energy ($E = \frac{1}{2}mv^2$), this can be converted to:

$$\sqrt{2m_{\mathrm{Li}}E_{\mathrm{Li}}} = \sqrt{2m_{\alpha}E_{\alpha}}. \tag{8}$$

Solving Equations (6) and (8) simultaneously, using masses for the Li=6535.13 MeV/c^2 and α=3727.38 MeV/c^2 yields:

$$E_{Li}=0.84 \text{ MeV and } E_{\alpha}=1.47 \text{ MeV}.$$

^{10}B has a microscopic absorption cross section for thermal neutrons of 3840 barns (substantially less than that of Gd). With a mass density of 2.15 g cm^{-3}, the solid structure of ^{10}B has a macroscopic thermal cross section of 500 cm^{-1} and the cross section follows a $1/v$ dependence [18].

Lithium Fluoride.

The ^{6}Li(n,t)^{4}He neutron reaction yields a single product branch emitting high energy charged particles:

$$^1_0\text{n} + ^6_3\text{Li} \longrightarrow ^3_1\text{H (2.7276MeV)} + ^4_2\text{He (2.0553MeV)}. \quad (9)$$

Similar to the boron products, the triton and α-particles are ejected in exactly opposite directions. The higher energy reaction products make them easier to discriminate from background γ-rays. ^{6}Li has a relatively large thermal neutron absorption cross section of 940 barns and also follows a $1/v$ dependence [18]. A disadvantage of working with lithium is that it is highly reactive and difficult to prevent from decomposing, even when using encapsulates. It is the stable compound LiF that is often used. The mass density of LiF is $\approx$2.54g cm^{-3}, and the resulting macroscopic thermal neutron absorption cross section is 57.5 cm^{-1} [18].

2.8 Perforated Thin-Film Semiconductor Detectors

Quick, accurate and inexpensive neutron detection and spectroscopy has been an enduring goal in the detection community. Thin-film semiconducting neutron

detectors show potential for solving this problem; however, basic planar thin-film coated diode detectors can only achieve practical maximum thermal neutron detection efficiencies of approximately 4.5% [17]. McGregor et al., along with many others, have conducted significant research into the perforation of diodes to improve the detection efficiency of thin-film semiconductor detectors [17, 19, 18, 20, 21, 22, 23, 24, 25, 26].

Recent advances with high-aspect ratio deep etching (HARDE) techniques have allowed unique perforated neutron detector structures to be realized [18]. Using HARDE, the diode is able to be permeated with perforations which are then backfilled with neutron reactive materials such as ^{10}B or ^{6}Li. As a result, the intrinsic thermal neutron detection efficiencies of single layer devices can be increased above 25%, more than five times that of a common, planar thin-film coated diode [18]. The stacking of these devices can increase detection efficiency to that of scintillators and gas tubes.

An incoming neutron will produce a measurable detector signal if the following two events occur. First, the neutron must interact in the conversion layer and produce one or more charged particles. Second, the reaction product charged particles must enter the detector volume to excite electron-hole pairs. Employing only planar thin-films means that, at most, only one of the charged particles can be detected. Worse yet, in the event that the particles are ejected at angles nearly parallel to the semiconductor surface, the event can go without getting detected at all. Perforations serve the main purpose of increasing the probability that the charged particles created in the conversion layer make it into the semiconductor layer of the detector to be potentially recorded.

Several different perforation geometries have been studied; an in-depth comparison was conduced by J.K. Shultis et al. and the results are investigated in the following sections. The spectra were obtained by Monte Carlo simulations and are ideal in the sense that no energy straggling, large-angle ion scattering or detector noise and

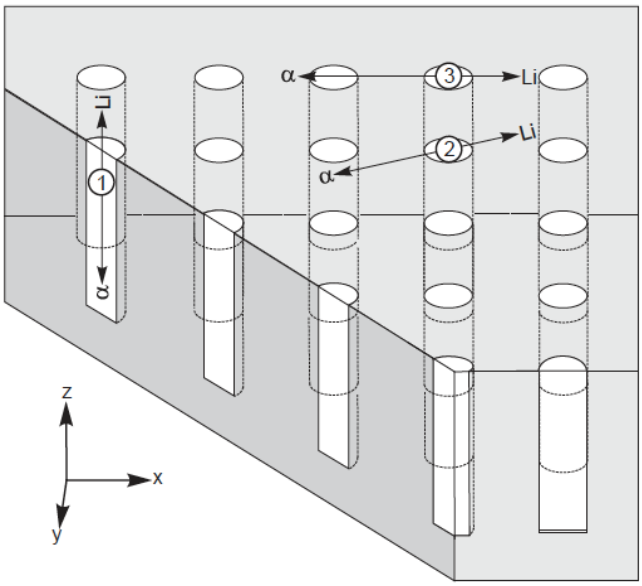

Figure 4. There are many trajectories for reaction products in a perforated hole structure. The main trajectories of interest are shown here: (1) A complete miss occurs if the ions travel in the z-direction, (2) one or both of the ions are absorbed in the semiconductor, and (3) with small dimensions, one or both ions can reach another absorber (LiF column), which effectively causes some ion energy to be lost and not absorbed in the semiconductor [25]. ©2009 with permission from Elsevier.

resolution effects are considered [25]. The three geometries covered are the cylindrical hole shaped perforations, straight trench-shaped perforations and pillars.

Cylindrical Hole Shaped Perforations.

This design offers a high probability of sensing ionizing reaction products, provided that the hole diameter is less than the cumulative ranges of both product ions. Fig. 4 shows a depiction of the cylindrical hole shaped perforation geometry.

The basic possible trajectories that reaction ions from either the ^{10}B(n,α)^{7}Li (as shown) or the ^{6}Li(n,t)^{4}He reaction can follow are shown in Fig. 4. Recall that the trajectories are in opposite directions for both reactions. In trajectory (1), the particles are emitted longitudinally along the perforation and do not enter into the semiconductor; hence they would not be recorded. Trajectories (2) and (3), and

variants, would result in one or both particles entering into the semiconductor and possibly record a count. Should an event occur in which the distance between the holes is shorter than an ion's range, then the particle may enter into another hole and thereby deposit less energy in the semiconductor, as depicted in trajectory (3). The probability of these various trajectories and resultant energy deposition profiles are a function of the fill material, hole diameter and cell pitch [25].

Straight Trench-Shaped Perforations.

Another structure investigated as a perforated detector is one with trench-shaped perforations etched into the semiconductor and filled with a neutron reactive material [25]. This design offers a high probability of capturing ion reaction products, provided that the trench width is less than the sum of the ranges of both reaction ions. A depiction of this geometry is shown in Fig. 5.

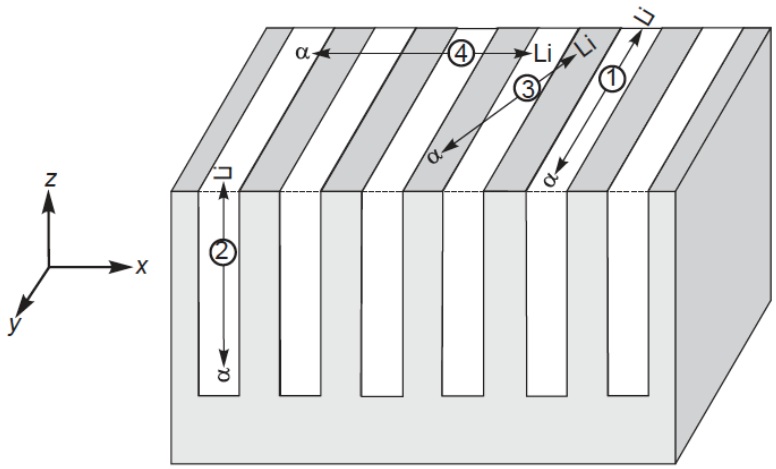

Figure 5. There are many trajectories for reaction products in a perforated trench design. The main trajectories of interest are shown here, where (1) a complete miss occurs if the reaction products travel in the y-direction, (2) a complete miss occurs if the reaction products travel in the z-direction, (3) one or both charged particles are absorbed in the semiconductor, and (4) with small dimensions, one or more charged particle reaction products can traverse another absorber trench which reduces the energy absorbed in the semiconductor [25]. ©2009 with permission from Elsevier.

Again, the basic possible trajectories have been outlined. In trajectory (1), ions are emitted parallel to the perforation axis (y-direction) and do not enter into the semiconductor; hence, they are not recorded. Also in trajectory (2), the particles are emitted longitudinally along the perforation (z-direction) and do not enter into the semiconductor, hence, again are not recorded. However, trajectories (3) and (4), and their variants, would in-fact result in both particles entering the semiconductor and will possibly produce a count. Should an event occur in which the distance between trenches is smaller than the ion range, then the ion may enter the adjacent trenches and deposit less energy in the semiconductor, as depicted in trajectory (4). The probability of these various trajectories and resultant energy deposition are a function of fill material, trench width and pitch [25]. A close-up picture of a trench perforated, LiF packed device is shown in Fig. 6.

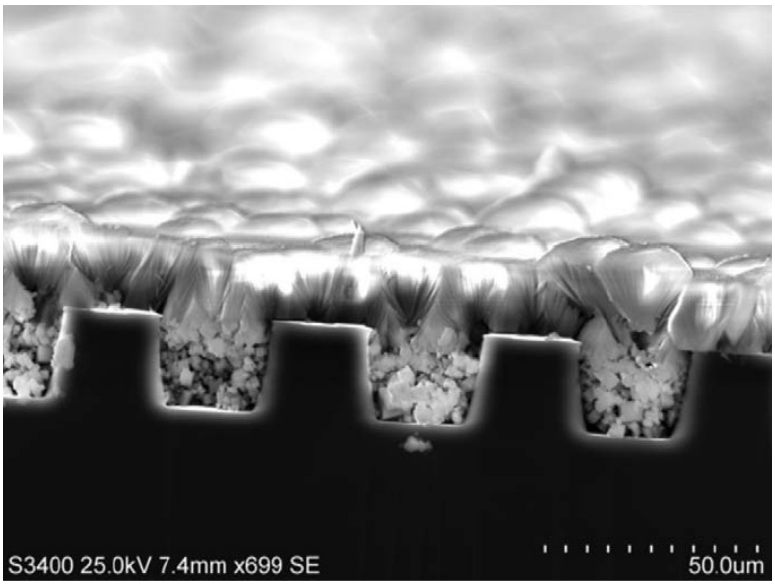

Figure 6. Picture was taken at S.M.A.R.T. Lab and is a close-up image of the LiF powder-packed trench perforations. The powder has been physically pressed into the 30 μm diameter by 20 μm deep holes with an evaporated LiF cap film [18]. ©2009 with permission from Elsevier.

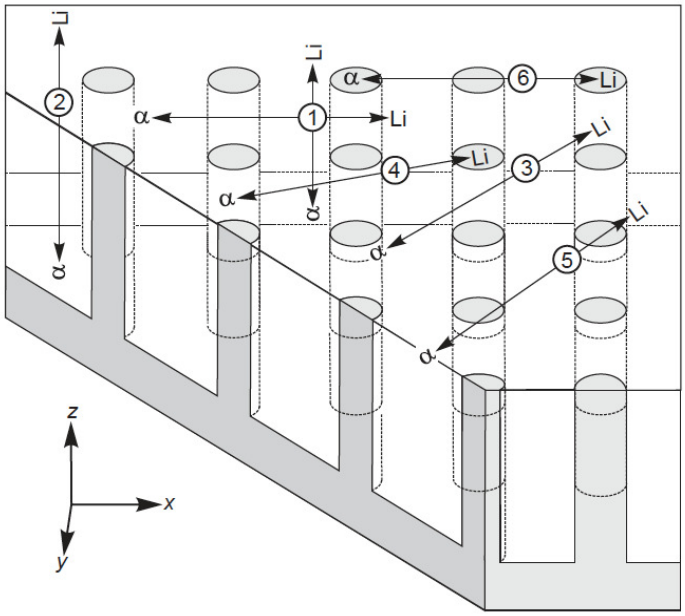

Figure 7. There are many more different trajectories for reaction products in a pillar structure than for the hole and trench structures. The main trajectories of interest are shown here, where (1) a complete miss can occur if the reaction products travel along the x or y-directions, (2) a complete miss occurs if the reaction products travel in the z direction, (3) a miss occurs if the reaction products travel in certain critical angles to the Si columns, (4) only one charged particle reaches the semiconductor, (5) both charged particles reach the semiconductor, and (6) with small dimensions, one or more charged particle reaction products can traverse more than one Si pillar, which increases the energy absorption in the semiconductor [25]. ©2009 with permission from Elsevier.

Pillar Devices.

To fabricate a pillar device, a large perforation is etched into the semiconductor to form a square matrix of miniature cylindrical columns [25]. The space around the columns is then backfilled with neutron reactive material, leaving only pillars of semiconductor to detect the reaction products. R.J. Nikolic et al. claim that a silicon device with 2 μm diameter pillars with a center-to-center pitch of 4 μm has an efficiency greater than 65% for 50 μm high pillars surrounded by enriched ^{10}B. An example of the geometry is shown in Fig. 7.

In this geometry, 80.3% of the surface is covered by the neutron reactive material

and 91.8% of the thermal neutrons normally incident on the 50 μm thick neutron reactive surface will be absorbed [25]. Hence, only 73.71% of neutrons normally incident on the surface of such a device are absorbed. The claim of 65% thermal neutron detection efficiency would indicate that over 88% of the reactions produce a count.

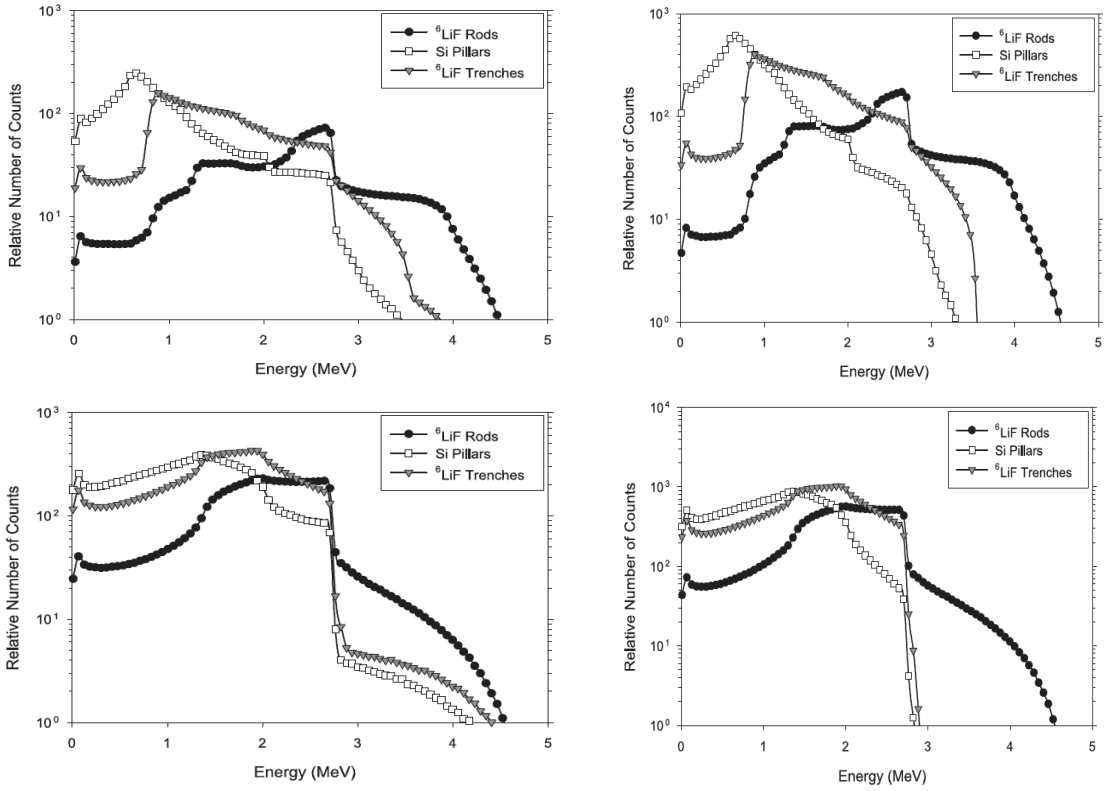

Figure 8. Provides a comparison of the geometries discussed above. Both the unit cell dimension and the feature depth are altered. Fig. A (top-left) is a comparison of energy deposition spectra for hole, trench and pillar designs with unit cell dimensions of 25 μm and feature ratios of 50%. The feature depths are 90 μm and are backfilled with LiF [25]. Fig. B. (top-right) is a comparison of energy deposition spectra for hole, trench and pillar designs with unit cell dimensions of 25 μm and feature ratios of 50%. The feature depths are 500 μm and are backfilled with LiF [25]. Fig. C. (bottom-left) is a comparison of energy deposition spectra for hole, trench and pillar designs with unit cell dimensions of 50 μm and feature ratios of 50%. The feature depths are 90 μm and are backfilled with LiF [25]. Fig. D. is a comparison of energy deposition spectra for hole, trench and pillar designs with unit cell dimensions of 50 μm and feature ratios of 50%. The feature depths are 500 μm and are backfilled with LiF [25]. ©2009 with permission from Elsevier.

Figure 8 displays the simulation results side-by-side for each of the geometries with different sized features. The unit cell dimension is the size of each feature, for example, the unit cell for the cylindrical geometry in Fig. 4 is the distance from the center of one pillar to the center of another pillar (along the x or y axis). Even considering the large deviation between the features, there is not a large difference realized at the lower energies. An obvious attribute to the figures is a drop-off of the relative counts at higher energies for the deeper trenches. This is likely due to the α-particle not escaping the neutron reactive layer. Another feature common to each of the figures is that the highest count rate belongs to the silicon pillar devices for the triton particle and to the LiF rod devices for the dual particle continuum (higher energies). Simulations such as these are necessary to maximize the detection efficiencies of the devices, taking into considerations both materials and geometries.

A conclusion of the research conducted by Shultis et al. is that the effective ranges of the reaction products from the ^{6}Li(n,t)^{4}He reaction are much greater than the effective ranges of reaction products from the ^{10}B(n,α)^{7}Li reaction, as expected [25]. This also has the consequence that the feature sizes with lithium can be larger and that the features must be deeper. In addition, regarding the semiconductor detector in use, silicon appears to be the best choice as a substrate because of its low γ-ray and neutron interaction cross sections. This serves to reduce the background radiation interactions; in addition, the processing technology of silicon is very mature, making it less expensive to use and very reliable. It is also noted that higher efficiencies can be achieved by stacking the detectors. The efficiencies for trench and hole devices can be nearly doubled, whereas the efficiency for pillar devices will increase only slightly due to neutron absorption in the first device of the stack [25].

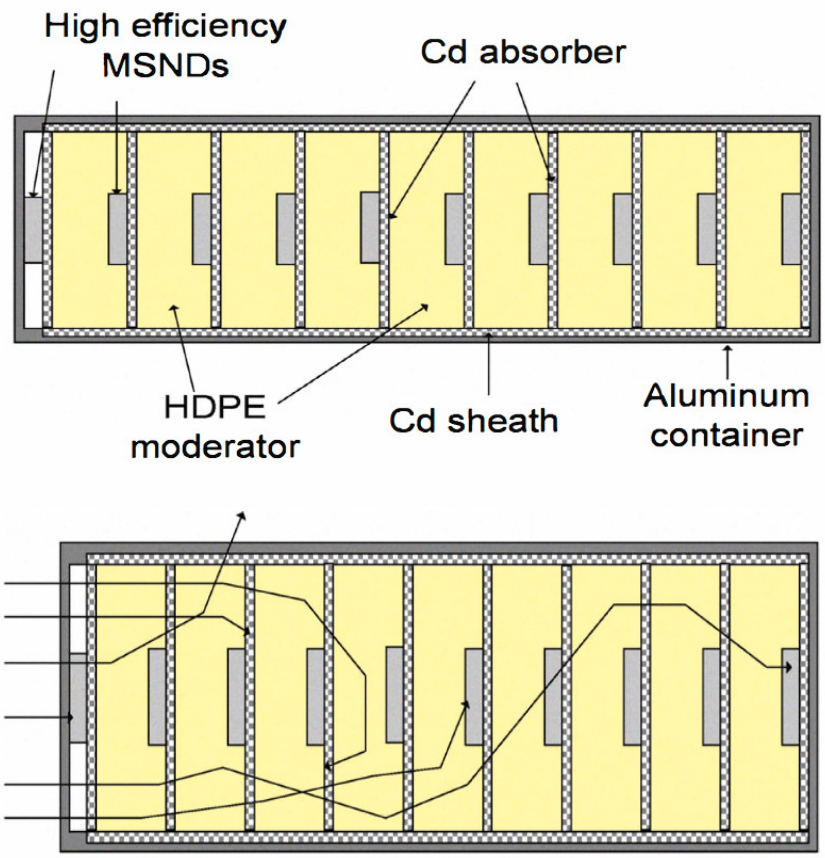

Figure 9. Fig. A (top) shows Cooper's neutron spectrometer arrangement. The moderator stack is capable of thermalizing 14 MeV neutrons. Cadmium shielding is used to block backscattered moderated neutrons [27]. Fig. B. (bottom) shows some possible trajectories and interactions within the neutron spectrometer as epithermal and fast neutrons lose energy by scattering through the moderator material [27]. ©2011 IEEE.

2.9 Semiconductor Neutron Detector-Spectroscopy

Spectroscopy with MSNDs has been limited over the past decade because of the limited efficiency of the devices. Bonner spheres have historically been the front runner with respect to moderating neutron spectrometers. While Bonner spheres are effective, they are not practical as a portable detection mechanism. A 2011 publication by Brian W. Cooper explores a MSND spectrometer for neutron energies up to 14 MeV using trench-structured ^{6}LiF detectors [27]. A cut-out view of the spectrometer

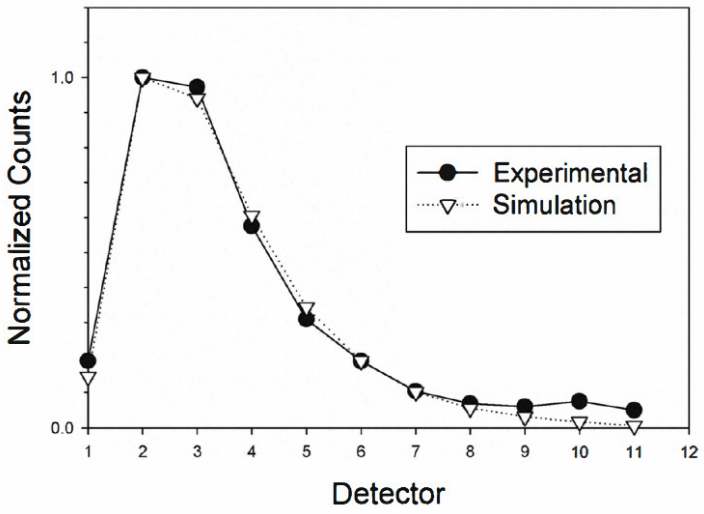

Figure 10. Experimental and simulated spectrometer spectrum of ^{252}Cf [27]. ©2011 IEEE.

is shown in Fig. 9A (top). Cadmium has a very high thermal neutron absorption cross section and is used to block backscattered moderated neutrons between each layer and around the perimeter of the entire stack.

The moderating material in use is high-density polyethylene (HDPE); it is placed before each subsequent detector and cadmium layer to partially moderate the neutron beam. Between each layer are two 1 cm^2 high-efficiency MSNDs [27]. A depiction of a few possible outcomes as a neutron beam travels through the spectrometer is shown in Fig. 9B (bottom).

In Fig. 9B, some of the thermalized neutrons will enter a detector and be counted. Theoretically, higher energy neutrons will penetrate further into the spectrometer (before losing enough energy to become thermalized and be detected). Other neutrons will scatter and can be lost to the spectrometer casing or get absorbed by the cadmium separating each layer. MCNP simulations were performed to model the response of a californium-252 (^{252}Cf) spectrum. A comparison between the simulated and experimental response is shown in Fig. 10.

Cooper states that the neutron energy spectrometer was able to match the simulated reference response for ^{252}Cf well. The first eight detector locations followed the expected spectrum closely whereas the last three started to deviate more. He hypothesizes that the differences are likely due to room-scattered neutrons entering deeper regions of the spectrometer from the side and undergoing sufficient moderation to thermalize and interact with the detector's neutron conversion material.

The next chapter will discuss the theory behind the neutron spectrometer, including the slowing of the neutrons in the moderating material and the collection of charge in the silicon semiconductor.

III. Theory

3.1 Neutron Detection

The primary thermal neutron interaction mechanism in lithium results in energetic triton and alpha particles liberated in opposite directions as depicted in Fig. 11. An important consideration in thin-film conversion materials is the probability of a neutron capture occurring and where in the material the reaction occurs. A layer too thick will not allow the energetic charged particles to escape and if this layer is too thin, the probability of a capture taking place in the layer will not allow a sufficient number of neutron captures. This section addresses the probability of capture in the conversion material and the physics governing charge generation in semiconductor detectors.

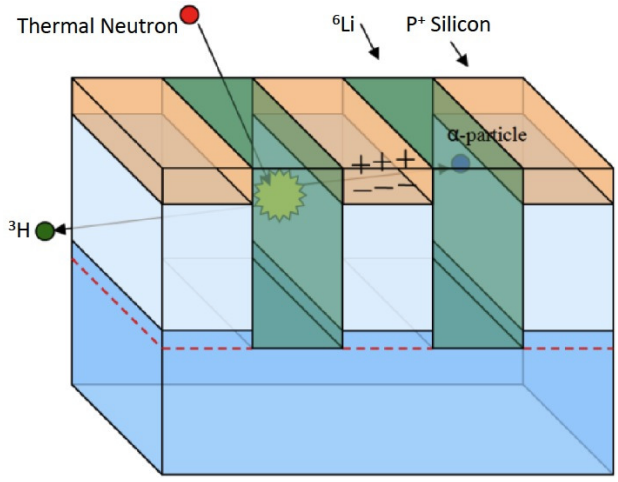

Figure 11. $^{1}_{0}\mathrm{n}+^{6}_{3}\mathrm{Li}\longrightarrow^{3}_{1}\mathrm{H}+^{4}_{2}\mathrm{He}$ **reaction in a trench perforated thin-film p-n diode consisting of p^{+}-type silicon adjacent to n-type silicon. The region between the two types of silicon is known as the depletion region and is represented by the *light blue* fill color [28].**

Neutrons may interact anywhere within the reactive film. The energy transferred to the semiconductor is dependent upon where in the conversion film the neutron interacts. Although it may appear that a thicker layer of neutron reactive material

is ideal, the voltage signal measured in the semiconductor is directly proportional to the e-h pairs liberated by the charged particles that cross the reactive material/semiconductor interface. If the neutron reactive layer is too thick, the charged particles can lose most or all of their energy before making it to the active volume of the semiconductor, hence not creating sufficient e-h pairs for detection. The finite specific energy loss in the reactive film limits the usable film thickness that can be deposited over the semiconductor device. The neutron flux transmitted through the film as a function of distance x can be described by [17]:

$$I(x) = I_0 e^{-x\sigma_F N_F} = I_0 e^{-x\Sigma_F}, \tag{10}$$

where

I_0 is the initial neutron flux,

N_F is the atomic density of the neutron reactive isotope in the film,

σ_F is the microscopic thermal neutron absorption cross-section of the film and

Σ_F is the film macroscopic thermal neutron absorption cross-section.

It follows that the fraction of neutrons absorbed in the film through distance x is [17]:

$$1 - \frac{I(x)}{I_0} = 1 - e^{-x\Sigma_F}. \tag{11}$$

The neutron absorption probability per unit distance is described by [17]:

$$p(x)dx = \Sigma_F e^{-x\Sigma_F} dx. \tag{12}$$

The angular contribution to self-attenuation must also be addressed. For example, a reaction product ejected perpendicular to the semiconductor surface will get detected with a higher probability than a particle ejected at an angle other than perpendicular due to the larger range and the decreased energy loss of the charged

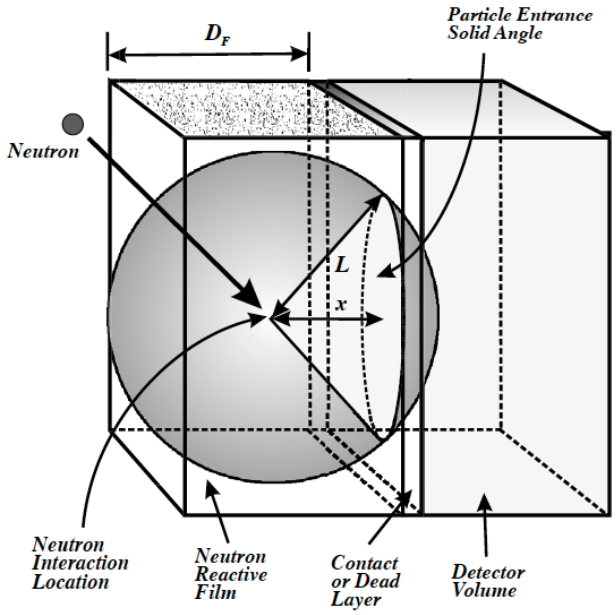

Figure 12. The solid angle formed by the reaction product range that subtends the detector at the interface predetermines the detection probability [17]. ©2003 with permission from Elsevier.

particles as they traverse through the neutron reactive film.

Once a neutron is absorbed and the reaction products are emitted, the probability that a reaction product will enter the detector is determined by the solid angle subtending the surface within the effective range (L) of the particle interaction [17]. Fig. 12 represents the solid angle of a neutron interaction taking place a distance x from the semiconductor/film interface. The fractional solid-angle can be described by [17]:

$$P_p(x) = \frac{\Omega(x)}{4\pi} = \frac{2\pi}{4\pi}\left(1 - \frac{x}{L}\right) = 0.5\left(1 - \frac{x}{L}\right), \quad x \leq L, \tag{13}$$

where the subscript 'p' relates to the reaction product of interest. Note that since the reaction of interest produces two different reaction products per event, it is necessary to add the detection probabilities of both reaction products. It is also worthy to note, as depicted in Fig. 13, that there is a finite probability (dependent on the neutron

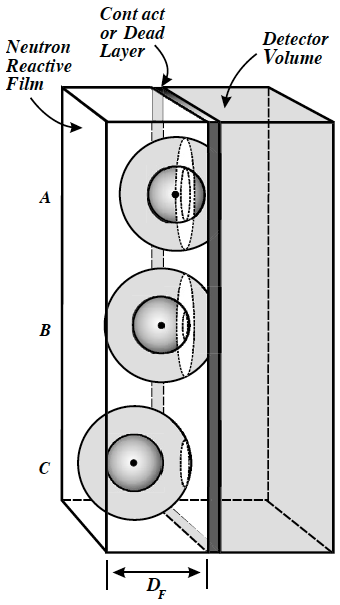

Figure 13. The solid angle subtending the detector at the interface is greatest for reactions occurring at the film/detector interface. Shown are cases where (A) either particle may enter the detector with high probability, (B) the short-range product has diminished detection probability, and (C) the short-range product will not be detected and the long-range product has diminished detection probability [17]. ©2003 with permission from Elsevier.

interaction depth) of one or none of the reaction products reaching the semiconductor active volume.

Interactions occurring near the detector contact result in either particle entering the detector with high probability as the solid angle approaches 2π. As the neutron interaction distance x increases, the probability of interaction of the short-range particle decreases more rapidly than that of the long-range particle, resulting in an overall decrease in detection sensitivity [17]. At neutron interactions greater than L_{LR}, which is the range of the long-range particle, the long-range particle can no longer reach the detector and the neutron absorptions are undetected. Ultimately, it serves no purpose to increase the thickness of the neutron reactive film beyond L_{LR}.

The ^{6}Li(n,α)^{3}H reaction emits a 2.73 MeV triton and a 2.05 MeV α-particle upon the absorption of a thermal neutron. Considering the stable compound ^{6}LiF as a

neutron reactive layer with a molecular density of 6.12×10^{22} molecules/cm^3 and a mass density of 2.54 g/cm^3, the ionization of the charged particles can be calculated via the Bethe-Bloche equation (Equation (2)). The results of this calculation are shown in Fig. 14. Although error bars are not shown, the actual range fluctuates from particle to particle due to deviations in the number of Coulombic scatters per unit distance and deviation in energy loss per collision [17].

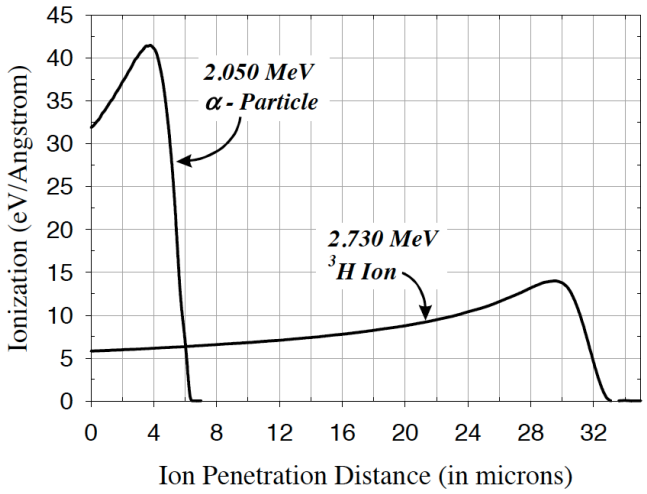

Figure 14. Bragg ionization distributions for the 2.73 MeV triton and the 2.05 MeV α-particles as they transit through a film of LiF. The ranges significantly differ for the two reaction products. The average range for the 2.73 MeV triton in LiF is 32.1 μm and the average range for the 2.05 MeV α-particle in LiF is 6.11 μm [17]. ©2003 with permission from Elsevier.

An interesting characteristic of the Bragg ionization curve for both the α-particle and the ^{3}H ion is the increase in columnar ionization per unit volume as the ion energy decreases. This is an important feature when considering the lower-level discriminator (LLD) value of the electronics detecting the charged particles. Although the range of a charged particle may be sufficient to reach the semiconductor, the particle may or may not generate enough charge to be ultimately detected. The particle must deposit enough energy in the semiconductor to surpass the noise level and trigger a response of the read-out electronics. The fact that a large portion of the particle's energy is

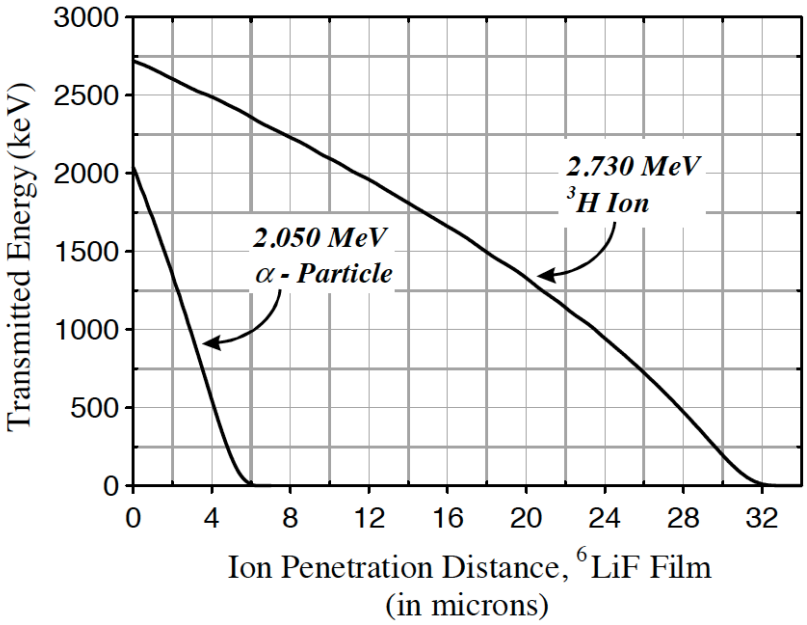

Figure 15. Energy deposited into the detector is the original particle energy minus the energy lost through self-absorption. Shown are the particle energies remaining from the ^{6}Li(n,α)^{3}H reaction as a function of transit distance through LiF [17]. ©2003 with permission from Elsevier.

deposited at the end of its range means that there is a higher probability of triggering the electronics if it can penetrate past the contact and into the semiconductor material. The energy remaining that is absorbed in the semiconductor is simply the initial energy minus the energy lost in the LiF film during transit, assuming that the energy loss in the contact is negligible. This remaining energy is shown in Fig. 15.

The next section will discuss how the charged particles are collected and read out as a current.

3.2 Semiconductor Detectors: Electron-Hole Pair Generation and Separation

The capture of a thermal neutron in the conversion layer is unfortunately not the last step in the generation of a read-out signal from the detectors. The charged particles must make their way to the semiconductor where electron-hole (e-h) pairs can be

liberated and output as a current. In order to develop a thorough understanding of the e-h pair generation and read-out current, it is necessary to outline the statistics governing the processes and physics controlling the generation of current from charged particle interactions: generation, recombination, diffusion and drift. The following section will first examine the semiconductor physics then proceed with a review of the processes that control the generation and movement of the e-h pairs within the semiconductor.

The success of semiconductor detectors is due to several unique properties that are not available with other types of detectors. Examples of these properties are: the combination of extremely precise position measurements and high readout speed, direct availability of signals in electronic form, the simultaneous precise measurement of energy and position and the possibility of integrating detector and readout electronics on a common substrate [29]. Semiconductor detectors usually provide only the primary ionization as signal charge. This mode of operation is possible because of the low energy needed for producing a signal electron (3.6 eV in silicon compared with ≈30 eV in gases) and the availability of very low noise electronics. The measurement of the primary ionization avoids the dependence on gain variation of the detector and therefore leads to stable operation in spectroscopic measurements [29].

Most commonly used semiconductors are single crystals with diamond or zinc blende lattice types. Both lattices may be viewed as being composed of two interpenetrating face-centered cubic sub-lattices that are displaced by one quarter of the distance along the diagonal of the cube. A more in-depth treatment of solid-state physics may be found in the text by Charles Kittel, 'Solid State Physics' [31]. Fig. 16 shows the first two energy levels in silicon, which have been calculated using quantum mechanics. Silicon semiconductors were used for the construction of the detectors used in this document, however research is being performed for many

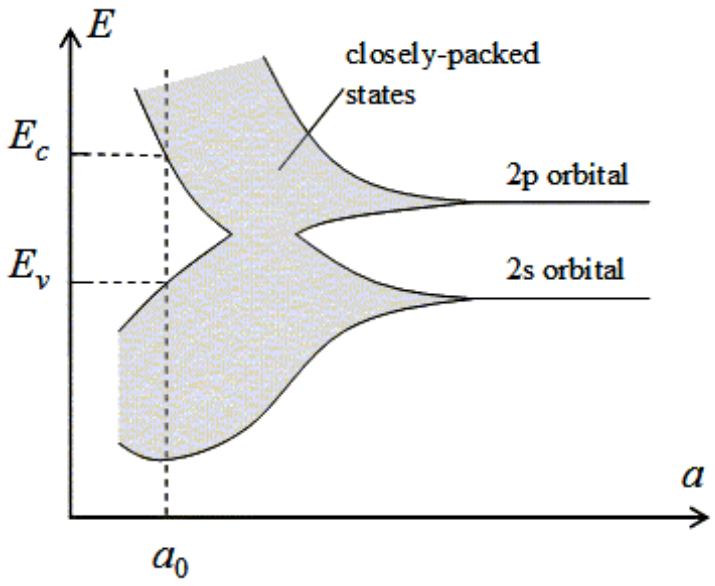

Figure 16. Energy levels of silicon atoms arranged in a diamond structure, as a function of lattice spacing [30].

alternative materials.

Laying the foundation for the movement of electrons and holes in a semiconductor requires a general understanding of the crystal, and also the distribution of energy states. It is possible for many purposes to treat electrons in the conduction band and holes in the valence band similar to free particles, but with an effective mass (m_n or m_p, respectively) different from elementary electrons not embedded in the lattice. The occupation probability for an electronic state with energy E is given by the Fermi-Dirac function [29]:

$$F(E) = \frac{1}{1 + exp\left(\frac{E - E_F}{kT}\right)}, \tag{14}$$

where E_F, the Fermi Energy, is the energy at which the occupation probability of a (possible) state is $\frac{1}{2}$, k is the Boltzmann constant and T is the absolute temperature.

After the occupation probability of a specific electronic state is known, the density

of states (DOS) in the semiconductor must be found in order to determine the density of holes and electrons which interact with the incident charged particles. The density of states in the conduction and valence bands is obtained in the standard way by considering standing waves in a unit volume of physical space, from which the number of states in a spherical layer of momentum space, corresponding to a range of kinetic energies is obtained [29]. Multiplying by two for the two electron spin directions leads to the number of states $N_{states}(E_{kin})$ in the unit volume in a small kinetic energy interval dE_{kin} around E_{kin} [29]:

$$N_{states}(E_{kin})dE_{kin} = 4\pi \cdot \left(\frac{2m}{h^2}\right)^{3/2} E_{kin}^{1/2}\, dE_{kin}, \tag{15}$$

where m is either the effective mass of the electrons or holes (m_n or m_p, respectively), h is Planck's constant and the kinetic energy is measured from the bottom of the conduction band for electrons and from the top of the valence band for holes. The density of free electrons n is obtained by integrating the carrier concentration given by the product of the density of states N and the occupation probability $F(E)$ over the conduction band [29]:

$$n = 2\left(\frac{2\pi m_n kT}{h^2}\right)^{3/2} e^{-\frac{E_C - E_F}{kT}} = N_C e^{-\frac{E_C - E_F}{kT}}. \tag{16}$$

Similarly for holes [29]

$$p = 2\left(\frac{2\pi m_p kT}{h^2}\right)^{3/2} e^{-\frac{E_F - E_V}{kT}} = N_V e^{-\frac{E_F - E_V}{kT}}, \tag{17}$$

where N_C and N_V are the effective densities of states in the conduction and valence bands, respectively. The Fermi level for intrinsic semiconductors, E_i, can be found from the requirement that the number of electrons and holes are equal ($n_i = n = p$). One thus finds that [29]:

$$n_i = \sqrt{N_C N_V} e^{-\frac{E_C - E_V}{2kT}} = \sqrt{N_C N_V} e^{-\frac{E_G}{2kT}} \tag{18}$$

and

$$E_i = \frac{E_C + E_V}{2} + \frac{3kT}{4} ln\left(\frac{m_p}{m_n}\right). \tag{19}$$

Now that the basis has been laid for the electron and hole concentrations in an intrinsic semiconductor, it is necessary to look at the extrinsic case (where the semiconductor has been doped to an excess concentration of electrons or holes). This is an important case because the diodes used for the collection of the α-particles and tritons in this research consist of a p-doped semiconductor adjacent to an n-doped semiconductor. The two oppositely doped semiconductors, when adjoined to each other in a specific configuration, create a p-n diode with a depletion region which becomes an efficient device for detecting charged particles.

The configuration of a semiconductor can be changed using the practice of doping. In silicon this can be accomplished using an atom such as arsenic (n-type). If one silicon atom is replaced with an atom of arsenic (five valence electrons), only four of the electrons are used for the formation of the covalent bond while the fifth is not bound to a specific atom and is free for conduction (donor). Silicon doped with arsenic creates an n-type material. Alternatively, if a silicon atom is replaced by an atom with only three valence electrons, one electron is missing in the covalent bond and a hole is thus created (acceptor), creating a p-type material. For n-type semiconductors, the situation that the donor levels are almost completely ionized can be described by a movement of the Fermi level (E_F) from the intrinsic level (E_i) towards the conduction band. Up to fairly high doping concentrations, the value of E_F can be attained by setting the electron concentration in the conduction band, n, equal to the donor concentration (N_D) [29]:

$$E_C - E_F = kT\ ln\frac{N_C}{N_D}. \tag{20}$$

Similarly, one obtains for p-type material and acceptor concentration (N_A) [29]:

$$E_F - E_V = kT\ ln\frac{N_V}{N_A}. \tag{21}$$

Using the previous results, the number of electrons and holes can be calculated:

$$n = n_i e^{\frac{E_F - E_i}{kT}} \tag{22}$$

and

$$p = n_i e^{\frac{E_i - E_F}{kT}}. \tag{23}$$

The increase of majority carriers (electrons in the case of n-type material) is accompanied by a decrease of minority carriers according to the mass-action law [29]:

$$n \cdot p = n_i^2. \tag{24}$$

Arguably, the most important electronic structure is the p-n junction, which is obtained by joining together extrinsic semiconductors of opposite doping. Such a structure shows diode characteristics, meaning it will conduct current mainly in one direction. Starting with the hypothetical condition that the homogeneously doped p and n regions are initially separated and electrically neutral in thermal equilibrium with electrons and holes evenly distributed in their respective volumes, once the bodies are brought into contact, electrons will diffuse into the p region and holes into the n region. A surplus of negative electric charge in the p region and positive electric charge in the n region will be created due to diffusion of the electrons across the

p-n junction. This diffusion also results in the creation of an electric field that ends up counteracting the diffusive movement of the electrons, creating what is known as a depletion, or space-charge, region between the two materials where excess charge from the dopant atoms is not neutralized by the movable carriers [29].

Penetration of charged particles into the semiconductor's depletion region creates ionizations; the two processes that subsequently dictate the density of electrons and holes in the diode are generation and recombination. Free electrons and holes may be generated by the promotion of electrons from the valence band into the conduction band, thus creating simultaneously equal numbers of electrons and holes. It is also possible to inject free carriers of a single type only, e.g. through a forward-biased diode, or to deplete the semiconductor of its free carriers by application of a reverse bias. The transition back to equilibrium is due to recombination, which happens as a result of drift and diffusion.

If an electric field is present, the charge carriers will be accelerated between random collisions in a direction determined by the electric field and a net average drift velocity will be obtained of [29]:

$$\nu_n = -\mu_n \mathcal{E} \tag{25}$$

for electrons and [29]:

$$\nu_p = -\mu_p \mathcal{E} \tag{26}$$

for holes, where μ_n and μ_p are the mobility of the electrons and holes, respectively and $\mathcal{E}$ is the electric field, which can be an applied voltage or a built-in voltage.

Diffusion is the transport mechanism which serves to smooth out the distribution of both the holes and the electrons in order to establish an equilibrium concentration in the diode. It is mathematically described by the diffusion equations [29]:

$$\mathbf{F}_n = -D_n \nabla n \tag{27}$$

and

$$\mathbf{F}_p = -D_p \nabla p. \tag{28}$$

Here $\mathbf{F_n}$ is the flux of electrons, D_n is the diffusion constant and ∇n is the gradient of carrier concentrations. The corresponding symbols for holes are represented by a p or a p subscript.

Combining the effects of drift and diffusion, one obtains the current densities [29]:

$$\mathbf{J}_n = q\mu_n n\mathcal{E} + qD_n \nabla n \tag{29}$$

for electrons and

$$\mathbf{J}_p = q\mu_p p\mathcal{E} - qD_p \nabla p \tag{30}$$

for holes, where mobility and diffusion are related to each other by the Einstein equation [29]:

$$D = \frac{kT}{q}\mu. \tag{31}$$

Charged particles traversing material lose part of their energy through elastic collisions with electrons, creating e-h pairs, as governed by the Bethe-Bloche equation (Equation (2)) [29]. The generation rate of electrons and holes can be solved via integration of the Bethe equation, however, not every e-h pair generated will make it to the electrodes. The electric field in the diode is important because it prevents the created e-h pairs from recombining, and pulls the respective charge to the energy bands, where contacts have been formed on the diode and the charge can be collected as a current. Although timing properties are not discussed herein, it should be noted that

generation and recombination lifetimes are important properties in a semiconductor that greatly affect their ability to be used as efficient radiation detectors.

Defining G_n and G_p as the generation rate of electrons and holes, respectively and R_n and R_p as the recombination rate of electrons and holes, respectively; it is now possible to write the continuity equations. The continuity equations describe the transport of charge carriers, maintaining that the carriers must be conserved [29]:

$$\frac{\partial n}{\partial t} = \mu_n n \nabla \mathcal{E} + D_n \nabla^2 n + G_n - R_n \tag{32}$$

and

$$\frac{\partial p}{\partial t} = -\mu_p p \nabla \mathcal{E} + D_p \nabla^2 p + G_p - R_p. \tag{33}$$

A final treatment of the subject in this quick overview looks at finding the voltage induced by radiation in a diode. Integrating the contribution of radiation to the current density in the depletion region yields:

$$J_R = -qG_R d_0 \tag{34}$$

where d_0 is the width of the depletion region. In reality, the width of the depletion region must also take into account the diffusion lengths of both the n and p sides of the diode, however, that will not be considered here and d_0 is an acceptable approximation. The total current density can then be written as:

$$J = J_s \left(e^{-\frac{qV}{kT}} - 1 \right) - J_R, \tag{35}$$

where J_s, the reverse bias saturation current, is part of the reverse current in a diode that is caused by diffusion of minority carriers (holes in the n-type or electrons in the p-type) from the neutral regions to the depletion region. J_s is not given a quantitative definition here, but is dependent on the intrinsic carrier concentrations, the diffusion

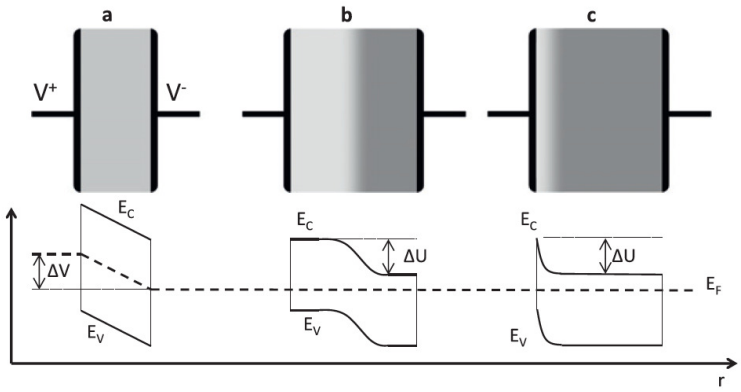

Figure 17. Three heterostructure electric field configurations through which e-h pairs may be separated: (a) resistive junction, (b) p-n junction and (c) Schottky junction. E_f is the Fermi level, and E_c and E_v are the conduction and valence band edges, respectively. The resistive junction requires an external voltage to establish an internal electric field within the semi-insulating material, while the p-n and Schottky junctions have a built-in scalar potential capable of separating e-h pairs without an external voltage. The graded area in (b) and (c) represents a space charge region created at the p-n and metal semiconductor interface [15]. ©2010 IOP Publishing.

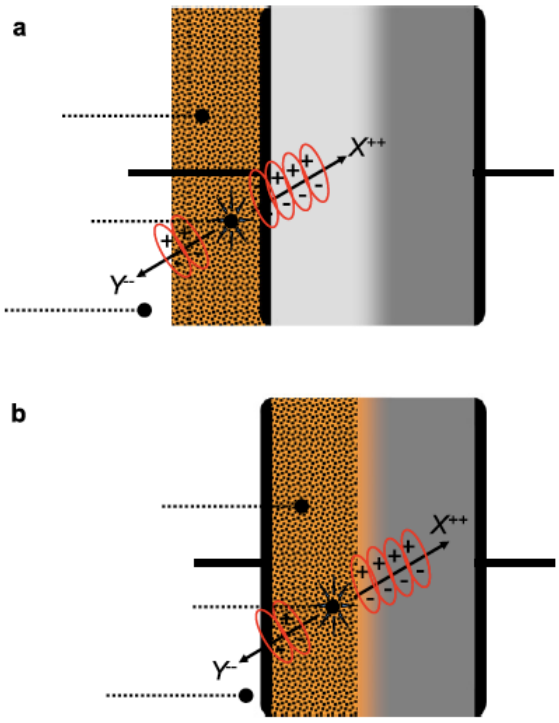

Figure 18. Representation of neutron transduction from (a) indirect-conversion (or conversion layer) and (b) direct conversion (or solid-form) solid-state p-n junction heterostructures [15]. ©2010 IOP Publishing.

coefficients, the donor and acceptor concentrations and the carrier lifetimes. Finally, the voltage induced by the charged particles in the diode can be written:

$$V = \frac{kT}{q} \ln \left[1 + \frac{qG_R d_0}{J_s} \right]. \tag{36}$$

Notice that the an increase in either the size of the depletion region or the amount of radiation will increase the voltage across the diode. It should be noted that the size of the depletion region can be increased, up to a point, by increasing the V_{RB}, or reverse bias voltage.

All solid-state devices that generate and separate e-h pairs do so through a heterostructure geometry [15]. Fig. 17 shows three configurations for potential use with neutron reactive coatings. Specifically, Fig. 17(b) shows a representation of the p-n junction previously discussed. The p-n junction diode acts as a radiation detector by use of either an externally applied neutron reactive layer (indirect-conversion) or by doping the semiconductor wafer with a neutron reactive isotope, hence creating a direct conversion detector. This is represented in Fig. 18. The direct conversion detectors will not be discussed in detail, however, they have their advantages and disadvantages. The technology is still immature and the efficiency of the detector is still well below that of an indirect-conversion device; however, the devices do not have the same limitations on collecting the charged particles from the n+Li reaction as there is a 4π solid angle. This advantage removes the need for perforations.

3.3 Neutron Moderators

The layered neutron spectrometer is dependent upon the use of a moderator between each layer so that the neutrons can be slowed to thermal velocities where they can then be detected with higher efficiency by the LiF neutron detectors. The concept is that the higher energy neutrons will need to penetrate a larger amount of mod-

erator (more scatters) before being thermalized. The physical process is, of course, stochastic, in that the behavior of the neutron (and reaction products) is intrinsically non-deterministic. Estimating the behavior of the system is possible with the use of simulations (as will be discussed later), however, it is still important to know the physics behind the energy loss of the neutrons. The following section will cover how the neutrons are decelerated.

Neutron Kinematics.

Neutrons react with the detector medium (the moderator or the neutron reactive material) via either elastic or inelastic scattering. A collision is elastic when kinetic energy is conserved and inelastic otherwise. For example, if some of the energy has gone towards modifying the internal state of the 'target', the reaction is inelastic. In the present case, inelastic effects are mostly negligible. The primary mechanism of slowing the neutrons through the hydrogenated neutron moderator is elastic scattering. Elastic scattering has no threshold, which means that it can occur with neutrons of any energy.

Since a neutron has no charge, it can enter into the nucleus and cause a reaction. This is where the cross section has a large effect on the signal of a detector. Simply because the interaction can easily occur does not mean that it has a high probability of occurring. Neutrons interact primarily with the nucleus of an atom except in the special case of magnetic scattering where the interaction involves the neutron spin and the magnetic moment of the atom, however, the absorption cross section of a neutron with a nucleus is negligible unless it is slowed sufficiently.

The use of highly hydrogenated materials to slow the neutrons to thermal energies is no coincidence. The physics is well known and understood, in fact, the most efficient moderator is hydrogen because a neutron can lose up to all of its energy in a

Table 2. Maximum fractional energy transfer in neutron elastic scattering.

Target Nucleus	A	$E_{R,max}$
$^{1}_{1}$H	1	1
$^{2}_{1}$H	2	0.889
$^{3}_{2}$He	3	0.750
$^{4}_{2}$He	4	0.640
$^{12}_{6}$C	12	0.284
$^{16}_{8}$O	16	0.221
$^{208}_{82}$Pb	208	0.019

single collision with a hydrogen nucleus [12]. Below is a brief explanation of neutron kinematics. The formulas are quite elementary, however, they accurately describe the motion of a neutron as it scatters from surrounding nuclei. Some necessary symbols are:

A = mass of target nucleus/neutron mass,

E_n= incoming neutron kinetic energy (laboratory system),

E_R= recoil nucleus kinetic energy (laboratory system),

Ψ= scattering angle of the neutron in the center-of-mass coordinate system and

θ= scattering angle of the recoil nucleus in the lab coordinate system.

The laws of elastic collisions can be established using the assumptions of a purely classical mechanical problem. If the incoming neutrons are well below the relativistic speeds ($E_n << 939$ MeV), conservation of momentum and energy define the energy of the recoil nucleus as:

$$E_r = \frac{2A}{(1+A)^2}(1 - cos(\Psi))E_n. \tag{37}$$

To convert to the more familiar laboratory coordinate system in which the original

target nucleus is at rest, we use the following transformation:

$$cos(\theta) = \sqrt{\frac{1 - cos(\Psi)}{2}}. \tag{38}$$

Combining Equation (38) with Equation (37) yields a new equation for the recoil nucleus energy in terms of its own angle of recoil:

$$E_R = \frac{4A}{(1+A)^2}(cos^2\theta)E_n. \tag{39}$$

As determined by the dependence on the $cos^2\theta$, a head on collision ($\theta = 0$) of the incoming neutron will lead to a recoil in the same direction resulting in maximum energy transfer:

$$E_{R,max} = \frac{4A}{(1+A)^2}E_n. \tag{40}$$

Table 2 lists the maximum energy that can be transferred to specific target nuclei. As the mass of the target nuclei increases, the maximum amount of energy that can be transferred decreases. This is expected due to the A^{-2} dependence in Equation 40. Notice that the $E_{R,max}$ value for the $^1_1$H nucleus is 1, meaning that an incoming neutron can potentially transfer all of its energy to the nucleus, immediately thermalizing it.

The next chapter will discuss the construction of a neutron spectrometer using alternating layers of LiF detectors and moderating materials, the instrumentation used for the experiment and also some of the preliminary results and modeling outcomes.

IV. Experiment

The experimental end-state is the construction and analysis of an eight-layer spectrometer to characterize unknown neutron sources. Eleven trench-perforated LiF micro-structured neutron detectors (MSNDs) were received from Kansas State University in February 2011. The detectors were each manufactured differently and had unique neutron responses. The first task in the spectrometer construction was to calibrate each of the individual LiF detectors to determine which of the detectors was operational and to normalize the responses to a known flux of thermal neutrons. Following detector calibration, the spectrometer was modeled using Geant4 computer simulations to determine appropriate spectrometer dimensions. The spectrometer was then constructed and commissioned using a D+D mono-energetic neutron source. An advanced data acquisition instrumentation system was assembled using a four channel analog-to-digital converter (ADC) and LabVIEW® for the simultaneous signal collection and discrimination of each detector in the spectrometer. The data from the commissioning run was unfolded using MAXED to determine the energy of the neutron spectrum from the mono-energetic neutron source. Following the commissioning runs, the spectrometer was used to identify the neutron energy spectrum of an unshielded PuBe poly-energetic neutron source.

4.1 LiF Detector Calibration

Initial testing consisted of characterizing each of the detectors individually and determining their response to a known flux of neutrons. The initial tests were conducted using a PuBe source and a moderating thermal neutron pile in the basement of building 470 on Wright Patterson Air Force Base, Ohio (shown in Fig. 19). Each of the detectors was initially tested for 60 minutes with an applied reverse bias of

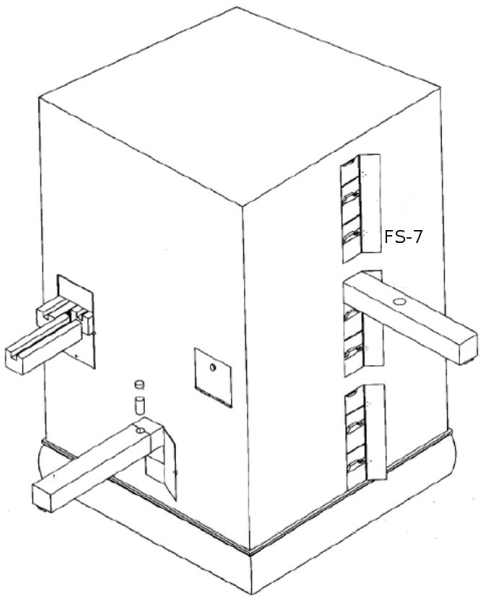

Figure 19. Model of the thermal neutron pile in the basement of building 470, WPAFB, OH. FS-7, the drawer used for calibration of the LiF detectors, is annotated in the figure [32].

2 V in the same location with a flux of approximately 2800 thermal neutrons/cm^{2}s. The spectra in Fig. 20A (top) were produced, showing the thermal neutron response of each detector. Additional testing found that of the initial 11 devices, two did not respond to the neutrons and only four of the devices produced the 'expected spectrum'. A spectrum produced by S.M.A.R.T. Laboratories at Kansas State University (the manufacturer of the devices) is shown in Fig. 20B (bottom). There should be a plateau-like feature where only a fraction of one reaction product is captured in the semiconductor, then a drop-off and dual particle continuum where both reaction products deposit some or all of their energy in the semiconductor.

The experimental setup used for the inaugural testing is shown in Fig. 21. An ORTEC 996 counter was initially used to verify that the detectors had a response to neutrons and that the response varied from the background counts. The counts received during the initial testing with the ORTEC 996 are shown in Table 3. The

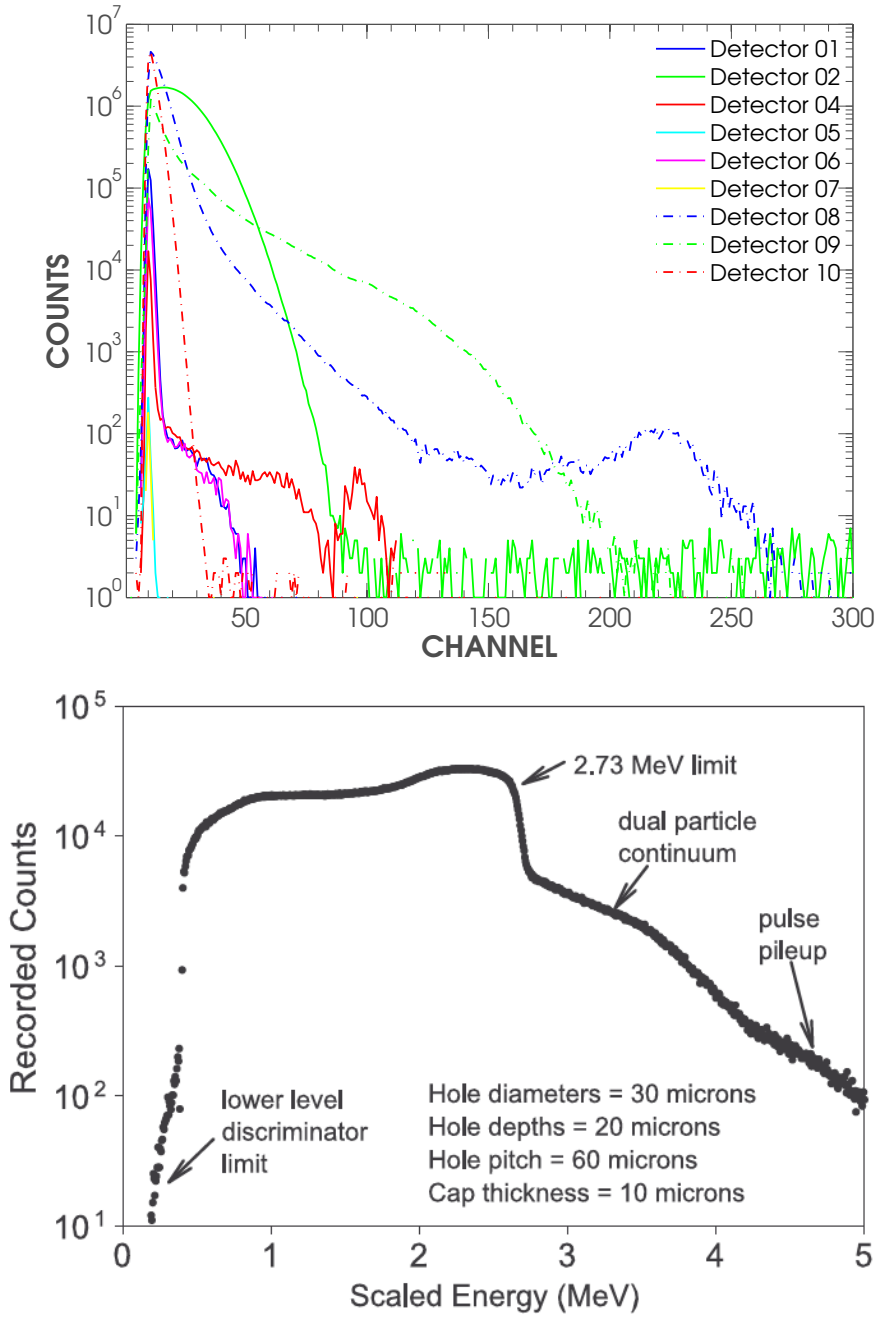

Figure 20. Fig. A (top) shows preliminary tests of each LiF semiconductor detector. As can be seen, each of the detectors has a different response. Data was accumulated for 60 minutes with each detector placed in drawer FS-7 of the thermal neutron pile with the PuBe source installed. Fig. B. (bottom) shows results obtained by D.S. McGregor et al. from Kansas State University's S.M.A.R.T. Laboratory. This is the resultant spectrum from a perforated Si device having 30 μm diameter holes, each 20 μm deep and backfilled with LiF powder. The device was covered with a 10.8 micron thick LiF layer and has a hole pitch of 60 μm. The major expected spectral features are clearly visible [18].

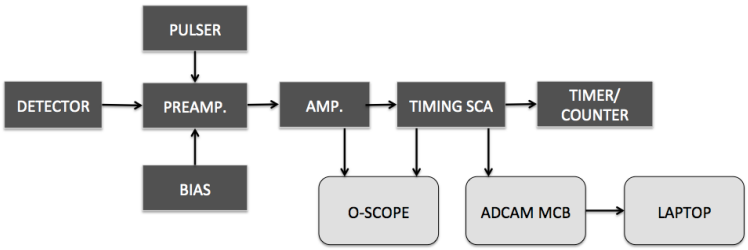

Figure 21. Experimental setup used for the preliminary testing of the LiF detectors. Both the ADCAM and the counter were used at different phases of testing. The discriminator was not used for preliminary testing, but was used to remove the noise and background counts on all subsequent tests. The amplifier was used to gain match the detectors.

objective of the test was to look for the detectors possessing a low background count and a large number of counts when introduced to the PuBe source. This test allowed for the automatic rejection of several detectors, such as #7 and #10, which did not react to the PuBe source at all.

Table 3. Results of initial 60 minute tests in FS-7 of the thermal neutron pile with a PuBe source.

Detector	LLD	Background	PuBe
1	500	387	2017
2	977	659	2059
3	43	63	3226
4	109	209	1798
5	144	153	544
6	128	0	22089
7	NA	0	0
8	292	178	42779
9	26	26	8051
10	NA	9	10
11	262	2	4472

In order to calibrate the detectors, each was placed in a neutron field for 36 hours (three different tests for 12 hours each). For consistency, three different neutron environments were used for the calibration. First, the PuBe thermal neutron pile

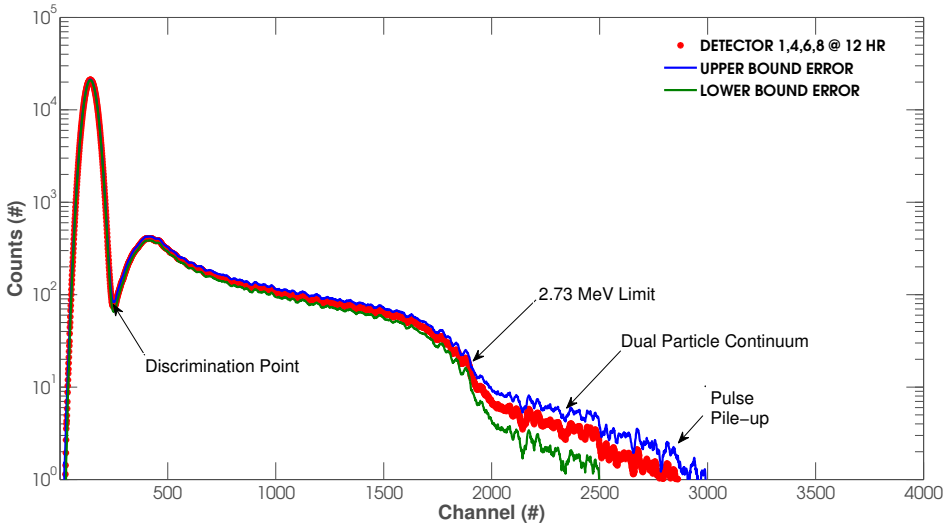

Figure 22. Spectrum as a result of superimposing detectors 01, 04, 06 and 08 in parallel. The spectrum was smoothed using the Savitzky-Golay smoothing method and the counting error has been accounted for. The spectrum is as-expected and closely resembles McGregor's spectrum as seen in Fig. 20B (bottom). The primary features have been labeled on the plot.

was used where the detectors were placed in the same location for each test, next the deuterium-deuterium (D+D) neutron generator was used (this was the source of neutrons for the spectrometer commissioning), and finally the D+D generator was used again, but with each detector wrapped in cadmium to determine each detector's response to only the fast neutrons. For the calibration tests in the D+D neutron generator, the detectors were each placed equidistant from the source with the front face of the detectors orthogonal to the 'beam'. With each detector placed in an identical setup for the same amount of time, the response of each detector can be normalized. The results of the normalization run from the D+D cavity without the cadmium shield are posted in Table 4. Note that only detectors 01, 04, 06 and 08 were normalized. These were the only detectors deemed operational and would therefore be the detectors used for construction of the spectrometer.

The spectrum of detectors 01, 04, 06 and 08 connected in parallel is shown in

Table 4. Normalization results with detectors 01, 04, 06 and 08. Each of the detectors has a unique discrimination level to discount the noise and the background radiation. After counting for twelve hours, a scalar value was used to normalize each of the detectors to the least performing detector, this was done to keep the statistics on the conservative side.

Detector	LLD [Arbitrary]	Counts	Normalization Factor
01	8900	6842	0.289
04	10400	3599	0.550
06	9800	1980	1.0
08	10800	7098	0.279

Fig. 22. The spectrum is as-expected and closely resembles McGregor's spectrum as shown in Fig. 20B. The discrimination point is located at approximately channel 400, the cutoff of the 2.73 MeV triton is located close to channel 2000 and the dual particle continuum is from channel 2000 upwards. This spectrum has been smoothed using the Savitzky-Golay smoothing method in order to remove the sharp fluctuations from the high resolution of the electronics and the noise (an example of a spectrum not smoothed is shown in Appendix A, Fig. 69). The spectrum was simply used to qualitatively verify the operation of the detectors. The values used for calibration of the detectors were obtained from raw data and not from Savitzky-Golay smoothed data.

After determining which of the detectors were operational, it was then necessary to analyze that the signal was indeed a result of thermal neutrons interacting within the detector volume. This analysis was accomplished using a 1 mm layer of cadmium which blocks the majority of the thermal neutrons from reaching the detector. The first 12-hour test was conducted with the detector in drawer 7 of the thermal neutron pile with no shielding. The next test would be conducted in the same manner, but with an enclosure of cadmium surrounding the detector. The results of the test are shown in Fig. 23. The *blue* line represents the standard testing conditions with

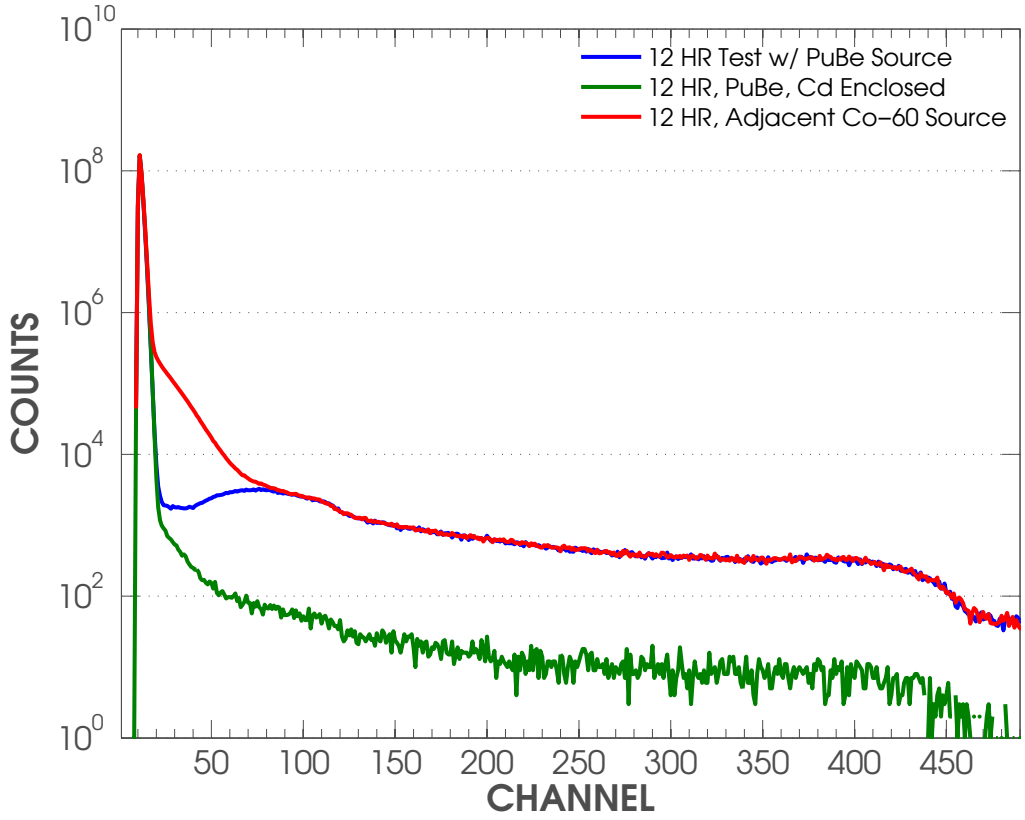

Figure 23. Response of the LiF thin-film detectors with the addition of a Co-60 γ-ray source and enclosed by a 1 mm thick cadmium sleeve. The detector was in the thermal neutron flux for all three configurations. The addition of the Cd sleeve reduces the detector signal to negligible levels giving confidence that the counts are indeed from the thermal neutrons. The addition of the cobalt-60 source (1.1732 and 1.3325 MeV γ-rays), additionally, did not affect the signal of the detector beyond the discrimination level.

detector placed in drawer 7 of the pile (PuBe source present) and no applied shielding. The *green* line represents the detector signal with cadmium shielding. A decrease in counts with the application of the cadmium is a solid indication that the signal being produced is a result of the thermal neutrons. The addition of the cadmium shell decreased the counts in nearly all channels $\geq$100 by approximately two orders of magnitude.

The next experiment examined how γ-rays are discriminated from neutrons in the detectors. The *red* line in Fig. 23 shows the detector response with the addition of a

cobalt-60 source to the thermal neutron flux. As shown, the 1.1732 and 1.3325 MeV γ-rays can be discriminated from the thermal neutron flux while still maintaining a low LLD level at around channel 80 (the cadmium shield was not in place for the γ-ray testing).

In addition to calibrating the detectors, an attempt was also made to determine the neutron detection efficiency. Knowing the detection efficiency of the detectors is not essential for the construction of the spectrometer, however, it is a valuable calculation in that the efficiency of the detectors governs the amount of time for data collection in order to identify a source of neutrons with good statistics. A higher neutron detection efficiency results in less data collection time.

Detector Efficiency.

Determining the efficiency of the LiF detectors requires knowledge of the flux that the detectors are being irradiated with. The thermal neutrons used for the initial testing were generated from a ^{239}Pu-Be source in a subcritical graphite pile. A model of the thermal neutron pile is shown in Fig. 19. The detector was tested in drawer 7 (FS-7), where the flux was determined via ^{115}In foil dosimetry in 2009 to be 2664 neutrons cm^{-2}-sec^{-1} with an anticipated increase of $\approx$ 2% per year [32]. A more detailed explanation of the foil activation process is presented in Appendix B.

Using this information, the approximate thermal neutron flux on the day of testing can be calculated:

$$\Phi_{th} \approx 2664 \times 1.02^{x} = 2827 cm^{-2} s^{-1} \tag{41}$$

where x is the number of years since 2009.

If the approximation is made that the active detection area of the detectors is 0.5 cm x 0.5 cm, and accounting for the counting error, the efficiency of detector 04 was

calculated to be 7.4 ± 1.1%. This number was only used for verification that the detectors worked as prescribed. According to a publication written by the provider of the detectors, the minimum detection efficiency (non-perforated) is ≈ 4.5% whereas the efficiency was shown to increase up to 25% with perforations [25]. The calculated efficiency is well within this range.

4.2 Spectrometer Construction

Initial testing showed that that highest performing detectors were detector 01, detector 04, detector 06 and detector 08. Each of these detectors performed with an efficiency higher than 5% and resulted in the expected spectrum. Resolving neutrons of common fissile materials using as few layers as possible was the overarching goal, however, it was determined using simulations that four layers would not be enough to resolve these energies with an appreciable accuracy. Using the four operational detectors, an eight layer design was experimentally tested to determine if this minimalistic approach could successfully differentiate different sources of neutrons. The first run was conducted using the first four layers (moderator, detector, moderator, ...), and the second run consisted of the first four layers with a 5 cm thick block of moderating paraffin wax (1.25 cm for each layer) placed in front of the first layer. This 5 cm block of wax replicated another four layers of the spectrometer, with the assumption that the neutron interactions with the silicon and LiF are negligible at higher energies. Merging the results of both simulations is the closest approximation to testing with an eight layer spectrometer. A representation of the eight layer spectrometer is shown in Fig. 24. This is the resultant concept of the spectrometer, as the 'eight layer spectrometer' was never built.

The layers of the spectrometer were constructed using a printed circuit board (PCB). This PCB was specifically designed to allow for easy construction of the

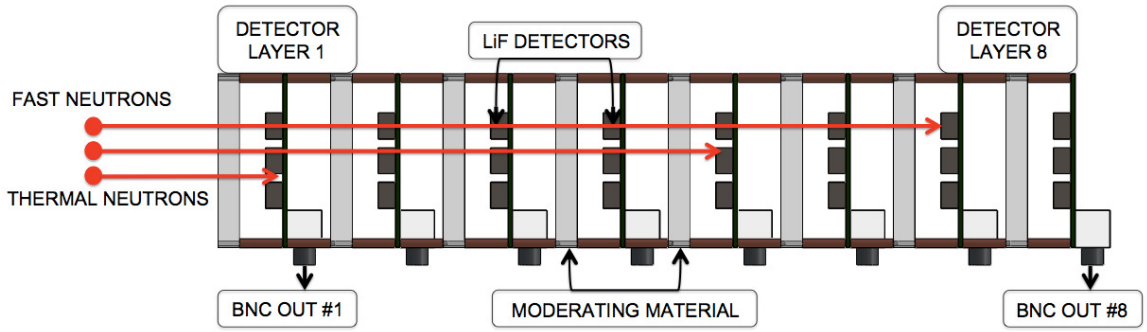

Figure 24. Model of the eight-layer spectrometer created in Solidworks®. The model shows nine detectors in each layer (3 x 3). The nine-detector design was the original concept to achieve higher detection efficiency with each detection layer, however, only one detector was mounted in the center of each detector layer due to lack of operational detectors.

spectrometer and to ensure that on-the-spot changes would be simple; the board is shown in Fig. 25. The board allowed the detectors to be moved from one layer and replaced in another layer using friction inserts. The boards were stacked adjacent to one another using only mechanical standoffs and the moderating materials were simply slid between each of the layers, again, using only friction inserts.

Use of the D+D neutron generator, which yields 2.45 MeV mono-energetic neutrons, was necessary in order to validate the initial construction of the spectrometer. Each set of experimental data was compared to an output spectrum generated from Geant4 simulations, as will be discussed in Section 5.1. For the commissioning tests, the front face of the detectors were placed perpendicular to the D+D source with the preamplifiers placed adjacent to the spectrometer. Testing with the PuBe source over an extended period of time proved the preamplifiers to be mostly insensitive to the neutrons of the D+D source; after 14 consecutive 12-hour tests with the PuBe source which has similar neutron energy, no significant degradation of the output spectra was evident. The coaxial cables from the output of the preamplifiers were each run to their corresponding ORTEC 572A shaping amplifiers. The output of each amplifier was then run to a corresponding channel of the NIMBox for data acquisition.

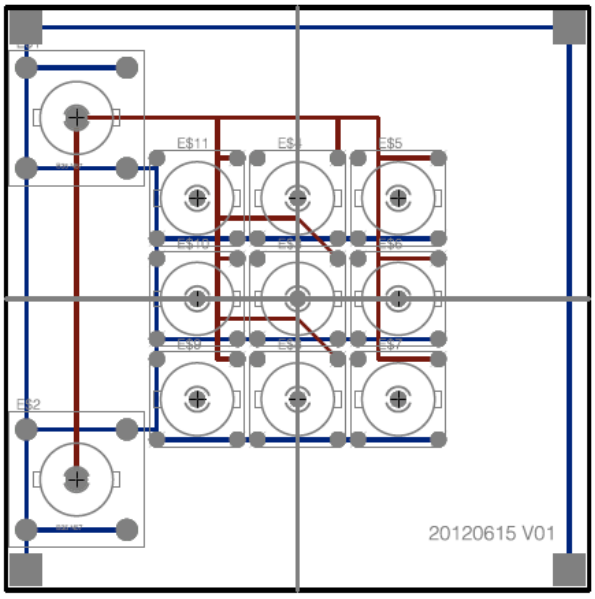

Figure 25. Top-view of the printed circuit board (PCB) schematic used for each layer of the spectrometer. The schematic was created in Eagle, which is a software program for designing PCBs. The design allows for nine detectors on each layer of the spectrometer (four pins each, in the center of the board) and has the ability to output the signal via two BNC connectors (five pins each, on the left edge of the board). The *blue* lines represent the grounding signals and the *red* lines represent the signal of each detector wired in parallel.

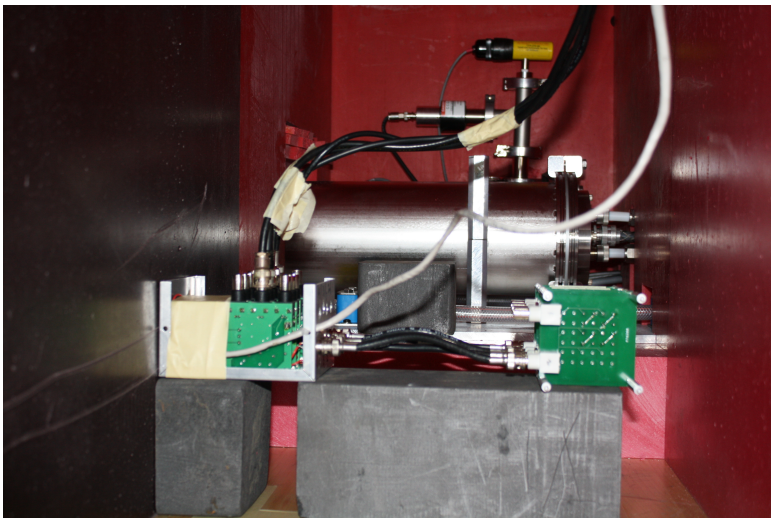

Figure 26. View of the D+D test setup. The D+D generator is visible extruding from the shielding on the left side of the picture and the spectrometer is the array on the lower-right side.

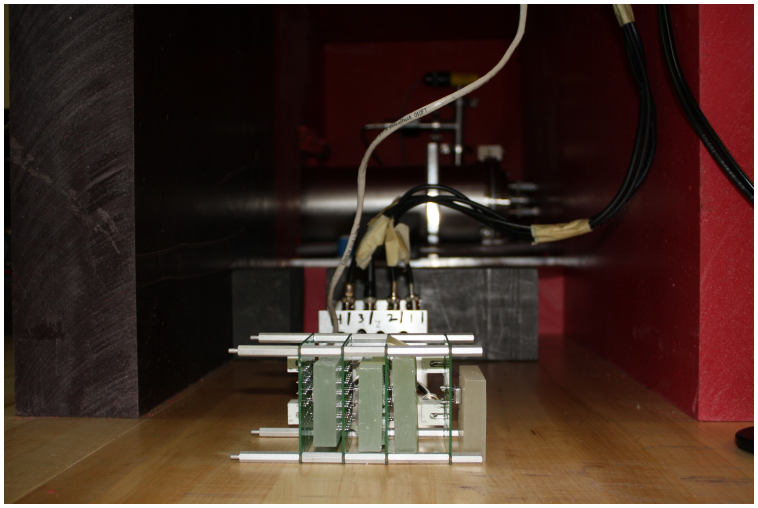

Figure 27. Side-view of the spectrometer. Notice the stand-offs and the alternating layers of moderator and detector (four layers).

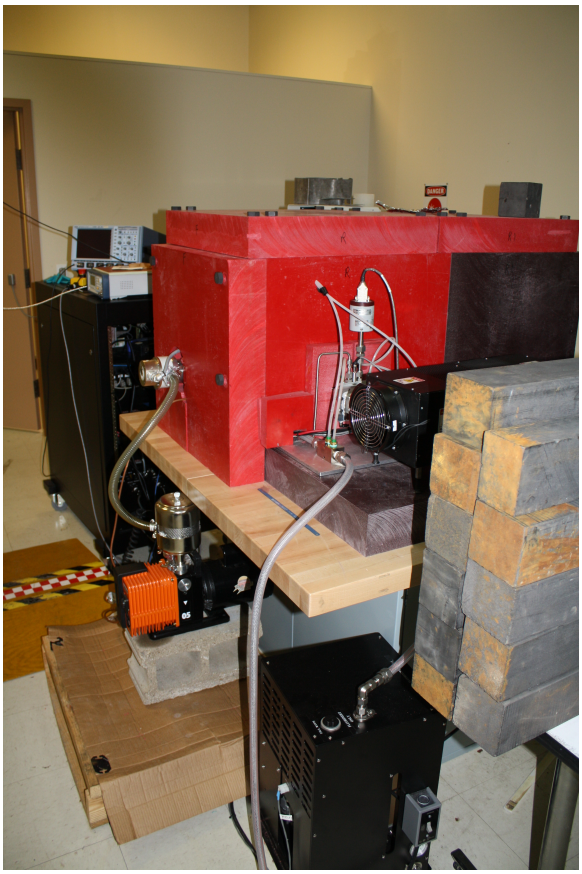

Figure 28. Exterior view of the D+D testing environment. The red blocks are borated polyethylene for blocking neutrons from escaping the generator assembly and penetrating into the surrounding rooms.

The four shaping amplifiers and NIMBox were each mounted in a NIM bin, which also provided a clean power source for each of the instruments. For the safety of the operator, in order to provide isolation from the active neutron source, a 50' USB cable with a repeater mounted at the 25' point was used to export the signal from the NIMBox to the laptop computer. Several commissioning runs were conducted. A picture of the testing environment is shown in Fig. 26. The stainless-steel tube protruding from the left side of the shielding is the D+D neutron source, which emits neutrons isotropically (there is a slight favor of momentum in the direction that the deuterons are accelerated, however the initial momentum is small compared to the Q-value of the reaction). The metal enclosure to the left of the picture is an array of preamplifiers; the grey power cable and four coaxial cables output the signal to the data acquisition system. The spectrometer assembly is shown to the right side of the picture. The visible circuit board on the bottom layer of the spectrometer is the board represented in Fig. 25. A side-view of the spectrometer is shown in Fig. 27 and an exterior view of the spectrometer is shown in Fig. 28.

4.3 Modeling

Simulations were necessary to model the response of the spectrometer without doing extensive testing. The purpose of the simulations during this research were twofold: first, they provided an indication that the spectrometer was operating as anticipated through comparison of experimental and simulated results. Second, the simulations were necessary in order to generate a library of response curves that were used to unfold the resultant experimental spectrum of the spectrometer.

Two simulation packages were considered for the detector simulations: Geant4, which is based on a Monte Carlo algorithm [33, 34] and MCNPX [35]. MCNPX, while considered to be the de facto standard for neutron transport, has a major disadvantage

for this application: a lack of attestation for heavy charged particle transport (Z>2) [28]. The shortcoming has been addressed in the latest version of MCNPX (2.7.0), however, this is still a Beta version and has not been verified. Following is a short overview of Geant4, a description of the program that was written, and finally the results.

Geant4 Overview.

Geant4, short for particle **GE**neration **AN**d **T**racking, was originally developed to meet an ever increasing demand for accurate and comprehensive physics simulations. The Geant4 simulation toolkit provides comprehensive detector and physics modeling capabilities embedded in a flexible C++ structure [33]. It serves primarily to simulate the passage of particles through matter and is used by a large number of experiments and projects in a variety of application domains including: high energy physics, astrophysics and space science, medical physics and radiation protection.

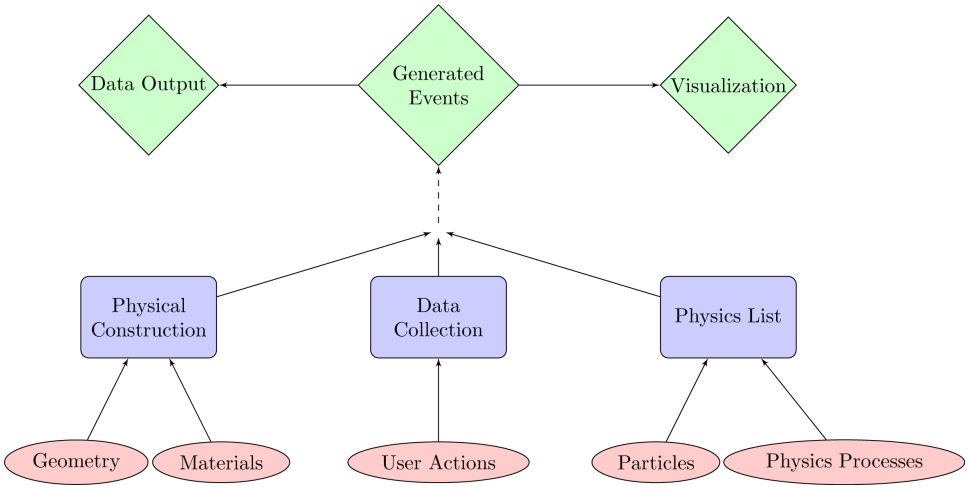

Figure 29. Flow chart representation of a Geant4 simulation. The lowest level represents the basic simulation building blocks, the second level consists of the user defined parameters, and the topmost level represents simulation execution and output [28].

Geant4 was chosen as the simulation package for this research because of its flexibility and robustness. Its kernel encompasses tracking, geometry description and

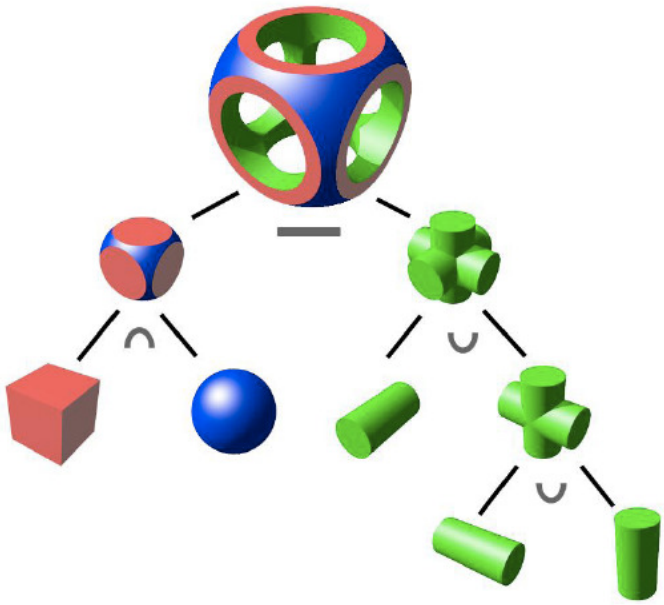

Figure 30. Boolean operations on constructive solid geometries (CSGs). The volumes on the left are combined via intersections, those on the right via union, and the final solid is a difference of the left and right [28].

navigation, material specification, abstract interfaces to physics processes, management of events, run configuration, stacking for track prioritization, tools for handling the detector response and interfaces to external frameworks, graphics and user interface systems [34]. Fig. 29 is a flow chart representing the hierarchal structure of Geant4. A few of the more-important processes are described below.

The first necessary step is to define the materials and geometry of the experimental setup. Constructive Solid Geometry (CSG) was used to define the apparatus, wherein volumes are described by a collection of simple three-dimensional volumes such as spheres, cubes, cones, etc. Using CSG, volumes have a much smaller memory footprint than if they were represented using Boundary Represented Solids (BREPS). BREPS and CSG are the two basic methods of describing geometries in Geant4 [28]. A representation of complex geometries that can be created using CSG is shown in Fig.

30.

```
//Enriched LiF
G4Isotope* Li3_6 = new G4Isotope(name="Li6", iz=3, n=6, a=6.00*g/mole);
G4Isotope* Li3_7 = new G4Isotope(name="Li7", iz=3, n=7, a=7.00*g/mole);
G4Element* ELithium = new G4Element(name="EnrichedLithium", symbol="Li",ncomponents=2);
ELithium->AddIsotope(Li3_6,abundance=95.*perCent);
ELithium->AddIsotope(Li3_7,abundance=5.*perCent);
G4Element* F = man->FindOrBuildElement("F");
G4double Ldensity = 2.37*g/cm3;
G4Material* LiF = new G4Material(name="LithiumFluoride", Ldensity, ncomponents=2);
LiF->AddElement(ELithium, natoms=1);
LiF->AddElement(F, natoms=1);
```

Figure 31. Example script from the 'DetectorConstruction.cc' file in Geant4. This selection of script defines the enriched LiF material for the simulation of the spectrometer.

Fig. 31 represents C++ script for defining a material in Geant4. The last two lines of the script show LiF consisting of one atom of fluorine and one atom of enriched lithium, where the enriched lithium is composed of 95% ^{6}Li and 5% ^{7}Li. The simulation is able to be customized and material definitions are often necessary in order to get more accurate results that closely resemble actual testing conditions. The materials defined herein include: air, paraffin wax, cadmium, silicon, aluminum, borated polyethylene and enriched LiF. After assembling the simulation, the next step is specifying the necessary particles and physics processes. In contrast to MCNPX, where most of the transport physics and secondary particle generation is automatic, Geant4 requires the user to explicitly define all particles and processes necessary for a particular setup; with 19 different physics models, spanning an energy range of meV up to the TeV region, not all particles and processes are valid for a given application [28]. When carefully implemented, the ability to select specific processes can substantially reduce the simulation time.

The execution of Geant4 can be broken down into four components [28].

- A *step*, which is the path of a particle between interaction and/or geometric boundaries.

- A *track* representing the sum of all steps for a particle.
- An *event* which tracks the history of a single original incident particle. This includes the tracks of any and all secondary particles.
- A *run* consisting of all events in the simulation.

Once all parameters of a simulation have been defined, Geant4 will construct the geometry and begin to simulate particle interactions as specified by the user. The particles will interact in a manner consistent with the physics defined by the user, with Geant4 calculating the steps as the particle traverses through the user defined geometries. A step is the shortest distance through the simulation that a particle travels, its length being the distance from one interaction to another. Each successive step is calculated by the particle's trajectory, with the energy, change in trajectory and other changes used to update the particle's state in order to calculate a new step. The process is iterated until zero kinetic energy remains, the particle is absorbed, or it escapes the simulation boundary [28]. It is important to consider, however, that there is not only one possible trajectory of a particle. Each successive step is determined using a Monte Carlo random sampling method. For each particle interaction, the mean free path is found from the individual cross sections and the material number density for the volume being traversed [28]:

$$\lambda_i = \frac{1}{\sigma_i N}, \tag{42}$$

where λ is the mean free path and i indicates the particular reaction. The mean free path is the average distance a particle will travel before interacting, but, there is a probability that the particle will traverse a much shorter or larger distance than the average. The true interaction distance l_i is sampled for each reaction using [28]:

$$n = 1 - e^{-\lambda_i l_i} \Rightarrow l_i = -\frac{\ln(1-n)}{\lambda_i}, \tag{43}$$

where n is a random number uniformly distributed in the range (0,1). This is done for each physics process assigned by the user; the interaction distances are then compared, with the shortest one chosen as the step length. If the distance to the volume boundary is less than the calculated step length, the step length is reduced to the boundary distance, where a new step is calculated [28]. Each step for a particular particle in a volume can then be stored in a track, where the particle's properties can be recalled. This gives the ability to sum all energy deposited in a volume, either directly or by secondary particles of an incident particle.

The energy deposited by each original incident particle is then binned at the run level using the Abstract Interface for Data Analysis (AIDA) [36]. AIDA was initiated at the HepVis 1999 workshop in Orsay and has since evolved into a robust histogramming utility allowing output of the data in several formats, most notably in the extensible markup language (XML) that can be read by many cross-platform applications such as MATLAB®. The user must instantiate the AIDA interface, specify the number of histograms required and the parameters of the histogram(s) [28]. Data is collected using the AIDA utility, allowing easy readout by the end-user. The next section discusses the simulation results obtained using Geant4.

Geant4 Results.

Simulations were used at several points in the spectrometer construction and evaluation process. Initially, simulations were conducted to determine the appropriate thickness of moderator in order to correctly resolve neutrons in the range of approximately 2.5 MeV. If the moderator was made too thick, many of the neutrons would be stopped before penetrating several layers of the spectrometer and energy informa-

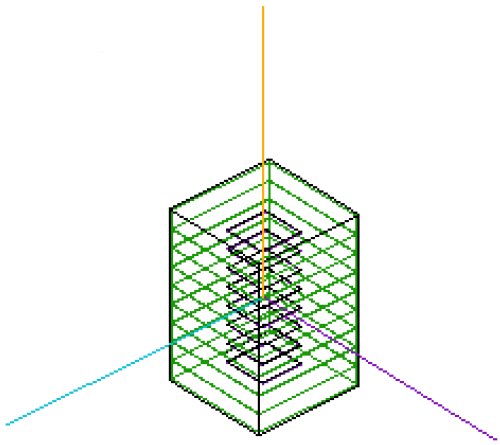

Figure 32. Geometry of the Geant4 simulation used to determine the appropriate thickness of moderator necessary to resolve the energy of 2.5 MeV neutrons. The *green* represents the boundaries of the individual moderating layers, the internal *black* lines are the boundaries of the LiF detectors and the exterior *black* lines represent boundaries of the cadmium layer surrounding the spectrometer.

tion would not be attainable. If the moderator thickness was too small, the reverse problem would occur and the neutrons would not be thermalized enough to interact with the LiF thermal neutron detectors. Fig. 32 represents the geometry used to determine the appropriate thickness of moderator to resolve the neutrons from the D+D source ($\approx$ 2.5 MeV).

As shown in Fig. 33, introduction of 2.45 MeV neutrons (using a planar source perpendicular to spectrometer's longitudinal axis) show that a paraffin wax moderator thickness of 1.25 cm is sufficient to resolve neutrons with energies on the order of 1 MeV. In the figure, 100 neutrons were incident upon layer 01 of the spectrometer (the top, from the figure); while only 5% of them ended up being thermalized and captured by a LiF detector, 100% ended up interacting in the moderator. The *blue*

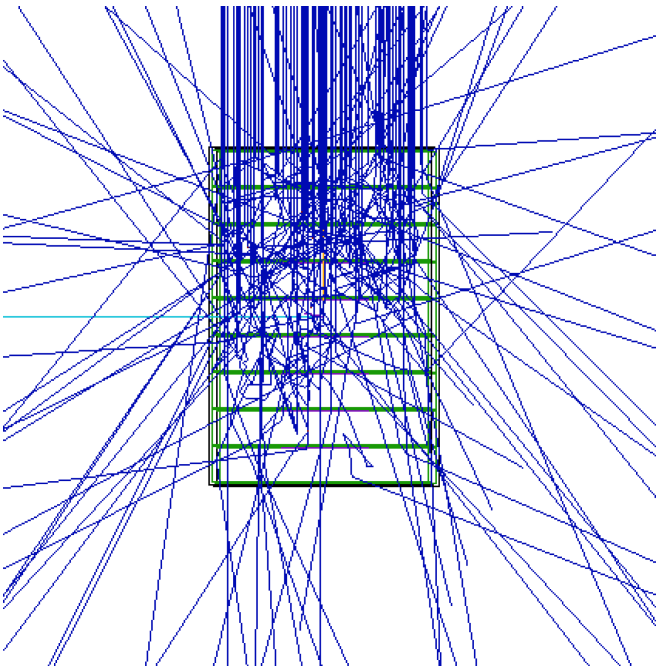

Figure 33. Introduction of neutrons to the spectrometer model. The neutron trajectories are shown with *blue* lines. 100 neutrons were introduced to the spectrometer, none of the original 100 penetrated all eight layers without interacting with the moderator. While only 5% interacted with an actual detector, the interactions occurred over many layers. More neutrons would improve the statistics.

lines indicate the trajectories of the neutrons. As specified previously, the neutrons must undergo a certain number of interactions (stochastic, based on scattering angle) before finally being thermalized and detected. Low energy neutrons have a high probability of being detected in the first layer and neutrons of higher energy will scatter many more times and have a probability of being detected further from the source of neutrons.

After determining the appropriate thickness of moderator, the next step was to add the D+D spectrometer environment into the simulation. The D+D spectrometer is surrounded by borated polyethylene which serves to shield the neutrons from escaping into the ambient atmosphere; however, it has a side effect of scattering the neutrons back toward the spectrometer and creates a flux that is not perpendicular to the front face of the spectrometer. Modeling this unique flux is necessary in order to

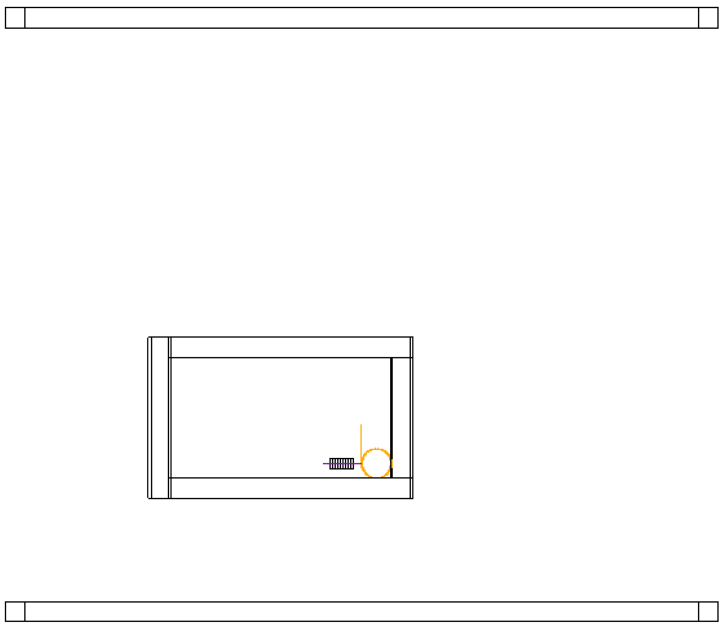

Figure 34. Geometry of the Geant4 simulation used to model the response of the spectrometer to the D+D neutrons. The geometry is representative of the structure housing the D+D generator, including the generator itself. The ceiling and floor of the room is represented by the top and bottom-most *black* rectangles. The generator is represented by the *orange* circle and the spectrometer is perpendicular to the generator. The four sides encompassing the generator are the borated polyethylene neutron shields and the entire structure is shown from a side view.

understand the effect of the scattered neutrons. The simulated environment can be seen in Fig. 34.

In Fig. 34, a side view of the generator housing is shown. This geometry can be compared to Figs. 26, 27 and 28; the simulation very closely represents the actual testing conditions. In Fig. 35, neutrons are introduced to the D+D enclosure. Many reflections take place within the borated-polyethylene shielding, some of the neutrons are directed back toward the spectrometer while some of them escape the enclosure altogether. The neutrons are tracked through the generator housing as well as through the spectrometer. If modeled correctly, the simulation results should closely relate to the experimental data.

Within Geant4, it is possible to track an infinite number of parameters. For the

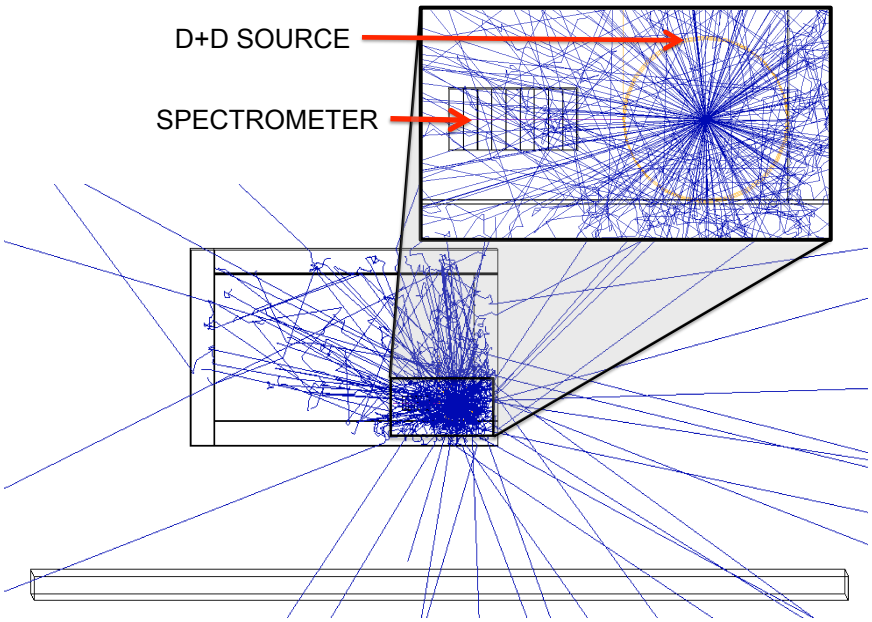

Figure 35. Introduction of neutrons to the shielded D+D model. The neutron interactions are tracked through the structure using Geant4 and AIDA. The neutron paths are represented by *blue* lines. Significant scattering occurs around the D+D source as shown by the inset, the *orange* circle represents the generator and the spectrometer is perpendicular to the source.

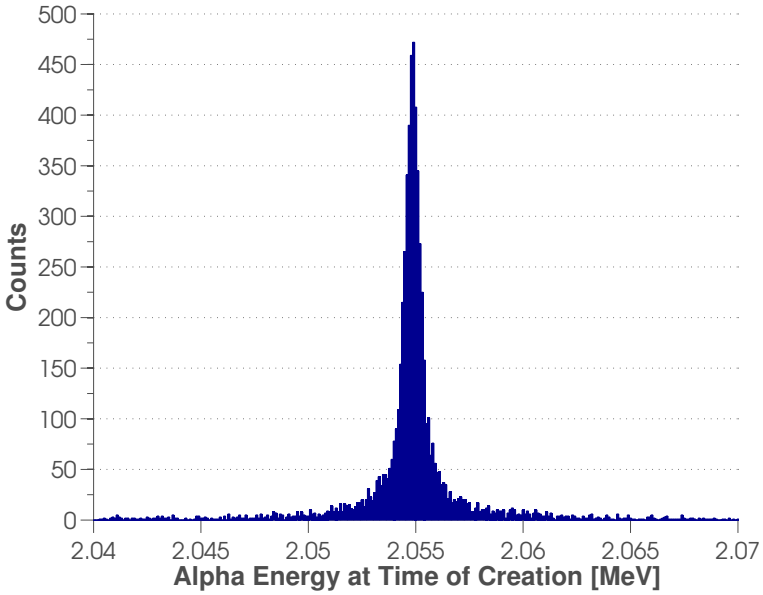

Figure 36. Simulation results of α-particle energies created in the neutron reactive material as a result of 1.0×10^7 2.45 MeV particles emitted isotropically and incident upon the front face of the spectrometer as shown in Fig. 33.

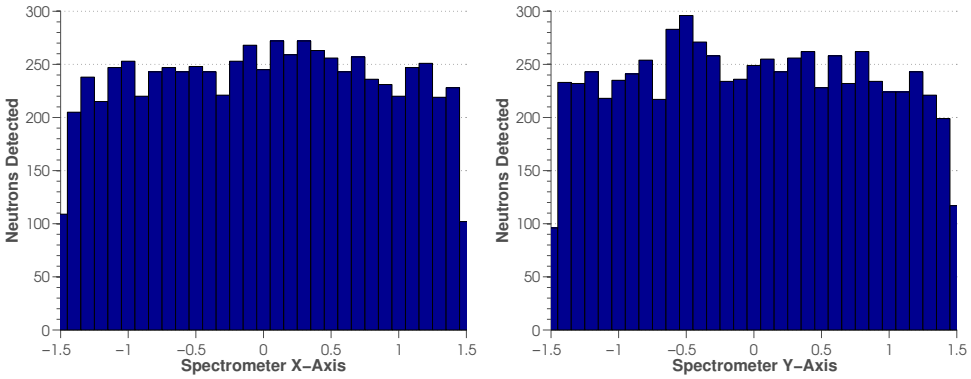

Figure 37. Reaction locations on the x-y plane within the detectors in the simulation. The x-y plane is defined on the face of the planar detectors with the z-axis being defined parallel to the beam and perpendicular to the front face of the detectors. Fig. A (left) shows the reactions along the x-axis and Fig. B. (right) shows the reactions along the y-axis. Notice that the reactions are evenly distributed over the entire face of the detector. This is expected from an isotropically emitting neutron source.

purpose of the spectrometer, the most important parameter is the layer in which the neutron reacts with the LiF, creating an α-particle and a triton. A trial simulation was run with 5.0×10^7 particles, consisting of 1.0×10^7 neutrons at five different energies (0.50 MeV, 1.00 MeV, 1.50 MeV, 2.00 MeV and 2.45 MeV). Several results of the simulation run are shown in Figs. 36, 37 and 38.

Fig. 36 shows the α-particle creation energy for every α-particle initialized during the interaction of the 1.0×10^7 2.45 MeV simulated neutrons. As previously shown in Equation (9), the expected α-particle energy is $\approx$2.055 MeV. The simulation appears to be consistent, hence giving confidence that the simulation physics is accurate. The two figures shown in Fig. 37 are plots of where the neutrons are reacting in the detector (Fig. A showing interactions on the x-axis and Fig. B showing interactions on the y-axis, the beam being projected parallel to the z-axis). The reactions are evenly distributed along the entire face of the detector, as would be expected from an isotropic source of neutrons. Lastly, Fig. 38 shows the interactions per layer for all five simulated energies. This, in essence, is a small library of response functions. A response function is a response of the spectrometer layers for a specific energy as shown

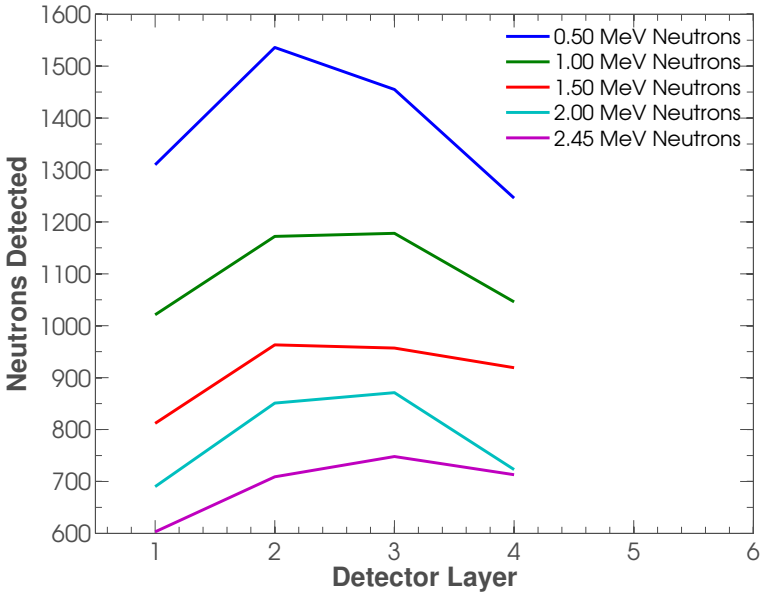

Figure 38. Basic library of response functions as a result of 1.0×10^7 neutrons emitted at each of the five listed energies. The library was created using the geometry shown in Fig. 33 and depicts the different spectrometer response as a function of neutron energy. Visual inspection of the data sets shows that the response functions are qualitatively similar with energies of the same order of magnitude.

in Fig. 38 or a response of a specific layer for a range of energies. A more exhaustive library of response functions has been compiled to unfold the spectrometer response curve and will be reported in the *Results* chapter. Unfolding the spectrometer data is necessary because each energetic neutron reacts in the spectrometer and penetrates slightly differently (as shown in Fig. 38); in a poly-energetic source where the emitted neutron spectrum contains a multitude of closely related energies, it is necessary to unfold the spectrum in order to discern sources which may have closely related spectra. Figure 38 demonstrates a point made previously that the lower energy neutrons are more likely to be detected and that the higher energy neutrons will stop less in the layers of the spectrometer closest to the source. This is a result of the higher number of collisions necessary to thermalize the higher-energy neutrons. Looking at the *blue* line, representing the 0.5 MeV neutrons, many more are stopped in the first two layers than the last layer. However, looking at the purple line, the 2.45 MeV neutrons,

more are stopped in the last layer than in the first two. This example shows neutrons with energies on the same order of magnitude; as the energy difference become more significant, so does the difference in features.

4.4 Data Acquisition

The data acquisition system used to gather the experimental data from the spectrometer started with an ORTEC 926-M32-USB Multichannel Analyzer and a laptop. With only one ADC, however, this was not a viable option for the multilayered spectrometer. The system then advanced to a NIMBox with a LabVIEW® interface as four channel simultaneous data acquisition became necessary.

Instrumentation.

The instrumentation started with an ADCAM MCB for data acquisition as shown previously in Fig. 21, then advanced to a Wiener NIMBox in order to support the simultaneous data acquisition of four channels. The instruments used are listed in Table 5.

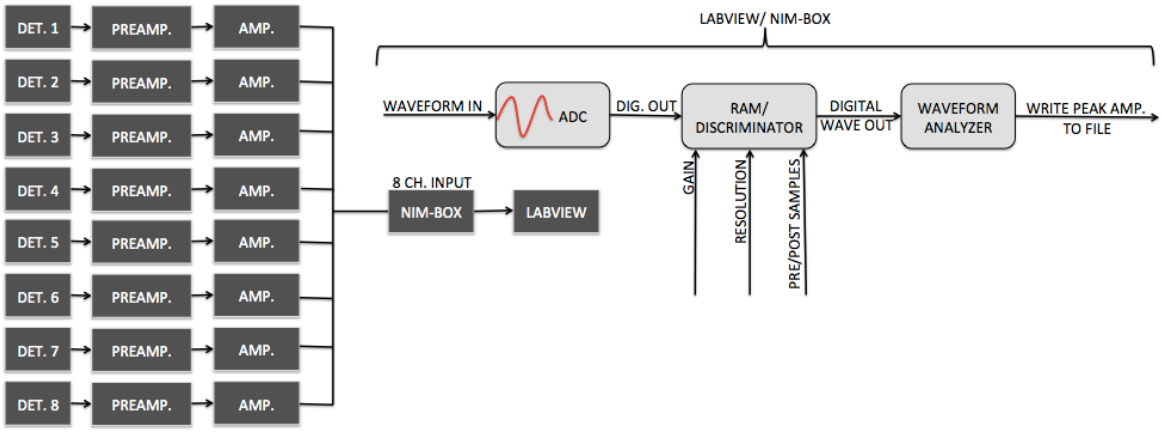

Figure 39. Instrumentation capable of simultaneous data acquisition of four channels. The heart of the system is the Wiener NIMBox. A LabVIEW® program was written for simultaneous visualization, discrimination and data storage.

Table 5. Instruments used for data acquisition in both the ADCAM and the NIMBox configurations. The SETUP column depicts whether the instrument was used for the ADCAM MCB DAQ setup (#1) or the NIMBox setup (#2).

Instrument	Model #	Serial #	SETUP
NINBin	4006 MiniBin	537-1	1,2
Bias Supply	ORTEC 478	041978	1,2
Pulser	ORTEC 480	2391	1,2
Amplifier	ORTEC 572A	253A	1,2
Amplifier	ORTEC 572A	536	2
Amplifier	ORTEC 572A	717	2
Amplifier	ORTEC 572A	7	2
Timing SCA	ORTEC 551	3880	1
Timer/ Counter	ORTEC 996	125	1
ADCAM MCB	ORTEC 926	10197413	1
Oscilloscope	Tektronix DP07104	B079400	1,2
PreAmplifier	ORTEC 142	1987	1
PreAmplifier (x4)	CREMONT 150	NA	2
Computer	Gateway	0040313918	1,2
NIMBox	NAD4	3789044	2

A diagram of the advanced instrumentation is shown in Fig. 39. The experimental setup is only four channels, however, the concept is identical to the eight channel representation. Each of the detectors connects directly to a preamplifier, then to a shaping amplifier. The output signals from each of the amplifiers connects directly to the front face of the NIMbox (each NIMBox is capable of 4 channel input). The signal is read out of the NIMBox via a USB cable connected to a computer running LabVIEW®. A LabVIEW® program was written for simultaneous visualization, discrimination and data storage of each channel.

NIMBox.

The NIMBox is a programmable NIM module based on a field-programmable gate array (FPGA) board with four slots for I/O submodules that serve as an interface between the FPGA I/O signals and the signals in the external environment [37]. It is

equipped with a USB port for programming and read out and a connector for direct FPGA programming/debugging. A FPGA is a semiconductor device containing programmable logic components and programmable interconnects. The programmable logic components can be programmed to duplicate the functionality of basic logic gates such as AND, OR, XOR, NOR or more complex combinational functions such as decoders or mathematical functions. In most FPGAs, these programmable logic elements (or logic blocks, in FPGA parlance) also include memory elements which may be simple flip-flops or more complete blocks of memories [37].

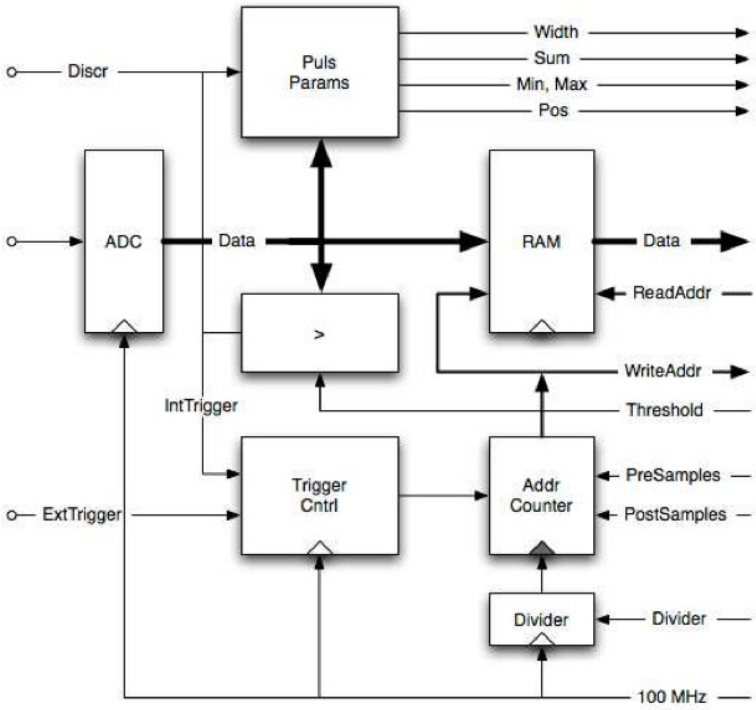

Figure 40. ADC block diagram for the NIMBox.

The manufacturer of the NIMBox, Wiener, has pre-compiled NIMBox/NEMBox Logic Pool VIs for ease of use with LabVIEW®, yet nothing was readily available that fit the requirements of the spectrometer. An accomplishment of this research was the construction of a LabVIEW® program for the individual and simultaneous control of each channel. A block diagram of the NIMBox is shown in Fig. 40. Using

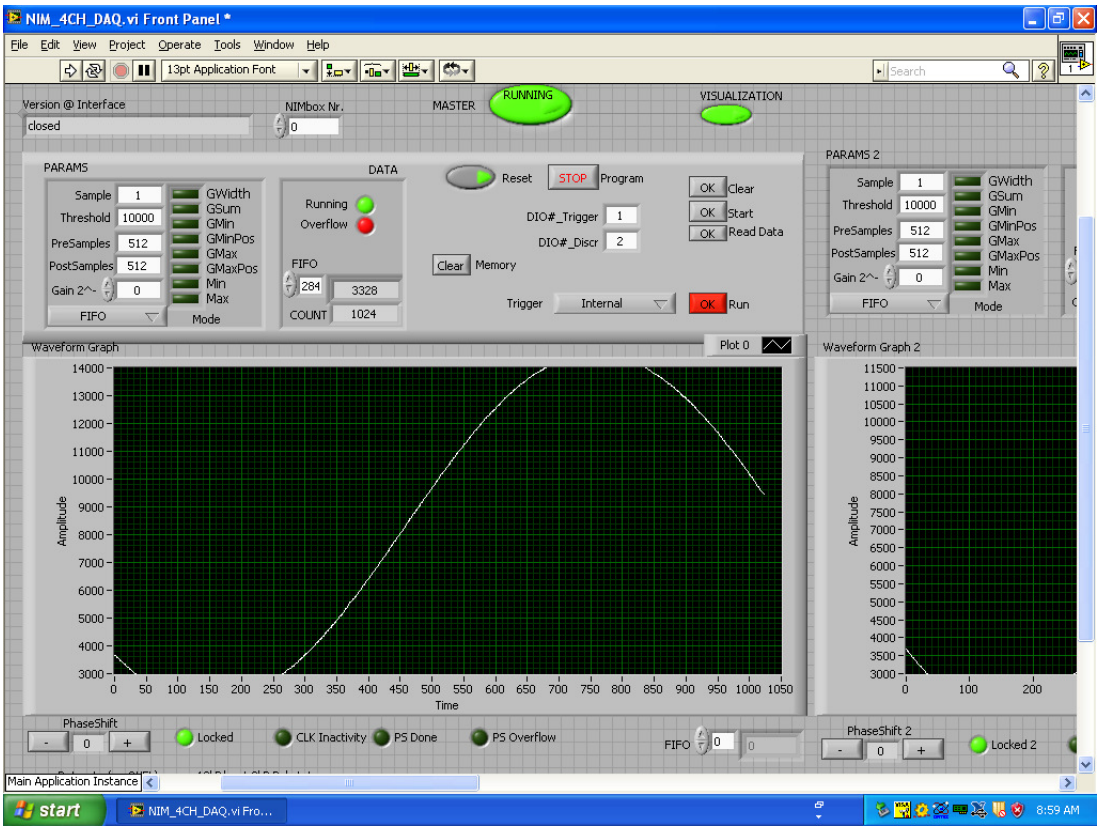

Figure 41. LabVIEW® interface for controlling the NIMBox. This figure only shows one complete interface, however three identical interfaces exist adjacently to the right on this panel. At the top of the figure is a MASTER run switch which controls all four channels simultaneously. There is also an option to turn the visualization on or off to save computing power and the *Samples*, *Threshold Value*, *PreSamples*, *PostSamples* and *gain* can be adjusted individually for each channel as shown in the upper left quadrant of the figure.

LabVIEW®, this diagram was expanded to four channels, allowing all four channels to start collecting data simultaneously while maintaining independent triggers and discrimination levels. The user-interface for controlling the NIMBox is shown in Fig. 41. This figure only shows one complete panel, however, three identical panels exist adjacently to the right. The visualization portion of the panel is the black grid. The four channels can be simultaneously controlled using the *MASTER* run switch at the top of panel one (as shown) and the visualization can be turned on or off. Turning the visualization off reduces computing power and allows the program to run faster.

The *Samples*, which is essentially the resolution can be adjusted as shown on the upper left quadrant of Fig. 41, as well as the *Threshold* (or discrimination level), *PreSamples* and *PostSamples* (how much of the waveform is saved) and the *Gain*.

LabVIEW®.

LabVIEW® (Laboratory Virtual Instrument Engineering Workbench) is a graphical programming language (known as G) that uses icons instead of lines of text to create applications. In contrast to text-based programming languages, where instructions determine the order of program execution, LabVIEW® uses data-flow programming where the flow of data through the nodes on the block diagram determines the execution order of the VIs (virtual instruments) and functions. Virtual instruments are LabVIEW® programs that imitate physical instruments [38]. VIs can perform operations as simple as taking two numbers and outputting their sum, or as complex as communication with an instrument, 'handshaking' and finally writing the data to a file. The imagination is the limit. An example G program is shown in Fig. 42. This program is written to gather data from an instrument using the *DAQ Assistant* (the left-most block), analyze the data using the *Amplitude and Level Measurements*, then finally export the measurement to a file using the right-most block. The G programming is intuitive because of the visual and diagrammatical modeling process.

Because LabVIEW® graphical G code is easy to comprehend, common programming tasks like debugging also become more intuitive as well. For example, LabVIEW® provides unique debugging tools that allow the user to watch as data interactively flows through the wires and nodes of a program and reports data values as they pass from one function to another along the wires. This is known within the LabVIEW® environment as *execution highlighting*. An example of execution highlighting is shown in Fig. 43. Notice the values are shown at the appropriate nodes.

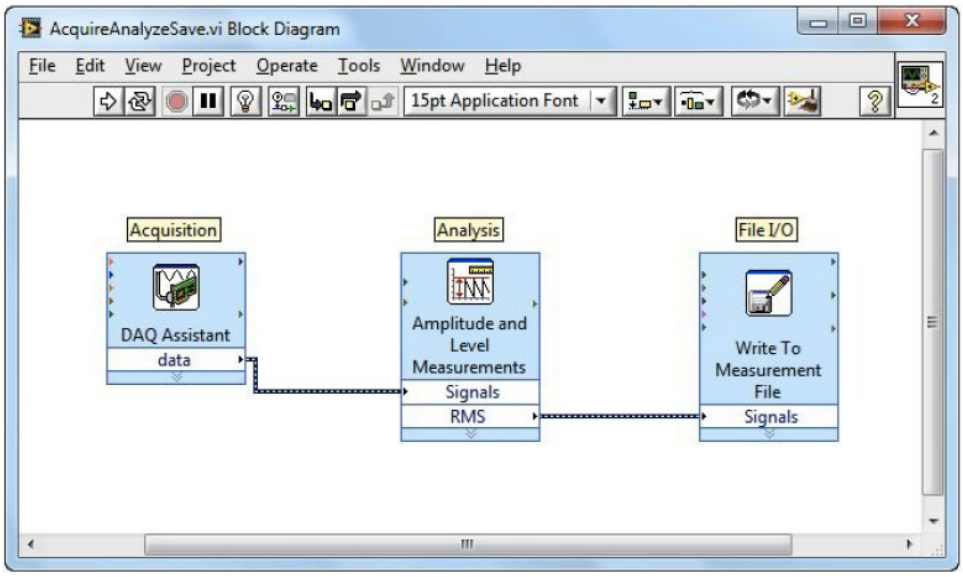

Figure 42. LabVIEW® program for data acquisition, analysis and writing to a file. Data originates in the acquisition function and then flows intuitively to the analysis and storage function through wires.

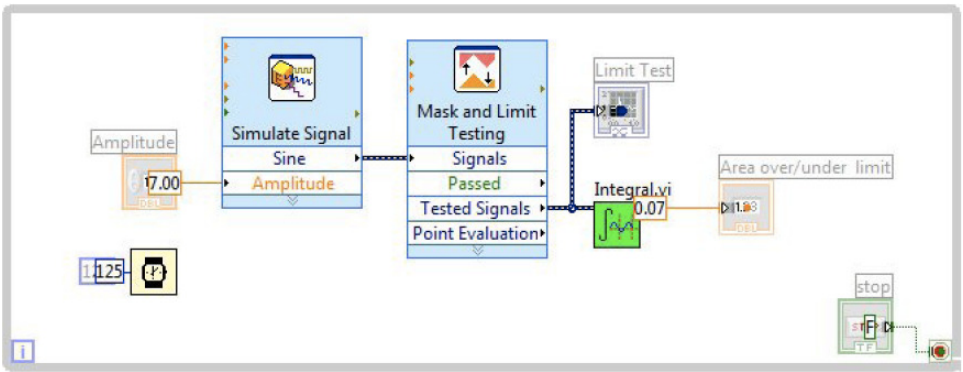

Figure 43. LabVIEW® interactive debugging environment allows visualization of data values as they pass from function to function along wires, reporting datum as they are analyzed real-time. This option is known as *execution highlighting* and it provides an intuitive way to understand the execution order of G code.

When execution highlighting is turned on, it allows the user to essentially watch the program execute in real-time; allowing for easy debugging.

4.5 Spectrometer Commissioning

Commissioning of the spectrometer occurred over four trials in the deuterium-deuterium neutron generator. For each run, the analysis was altered in some way to improve the fit of the experimental results with the Geant4 simulation data. The final commissioning assessment was performed by taking two sets of data for 10 hours (20 hours total) with the spectrometer placed in a 1 mm thick cadmium case within the neutron environment of the generator. The data was compared to simulations and unfolded to reveal the resultant spectrum.

D+D Generator.

Because α-particles are the only heavy charged particles with low-Z conveniently available from radioisotopes, reactions involving incident protons, deuterons, and so on must rely on artificially accelerated particles [12]. Two of the most common reactions of this type used to produce neutrons are:

$$ {}^{2}_{1}\mathrm{H} + {}^{2}_{1}\mathrm{H} \rightarrow {}^{3}_{2}\mathrm{He} + {}^{1}_{0}\mathrm{n} + 3.26\mathrm{MeV} \qquad (D+D) \tag{44} $$

and

$$ {}^{2}_{1}\mathrm{H} + {}^{3}_{1}\mathrm{H} \rightarrow {}^{4}_{2}\mathrm{He} + {}^{1}_{0}\mathrm{n} + 17.6\mathrm{MeV} \qquad (D+T). \tag{45} $$

Because the coulomb barrier between the incident deuteron and the light target nucleus is relatively small, the deuterons need not be accelerated to a very high energy in order to create a significant neutron yield. These reactions are widely exploited in neutron generators where deuterium ions are accelerated by a potential of about

100-300 kV. Since the incident particle energy is then small compared to the Q value of either reaction, all the neutrons produced have the same energy (near 2.45 MeV for DD and 14 MeV for DT). A 1 mA beam of deuterons will produce about 10^9 n/s from a thick deuterium target and about 10^{11} n/s from a tritium target. Somewhat smaller yields are produced in compact neutron generators consisting of a sealed tube containing the ion source and target, together with a portable high voltage generator [39].

An Adelphi Technology Incorporated DD108 Neutron Generator was used to produce the neutrons for the data collection and validation of the spectrometer, shown previously in Fig. 27. The system is actively vacuum-pumped and uses a continuous trickle supply of non-radioactive deuterium gas. The DD108 works well as a neutron source for testing the spectrometer because the emitted lower-energy neutrons are of the same order of magnitude as those released by spontaneously fissioning SNM, and it additionally does not produce higher energy neutrons which may be more difficult to shield and moderate.

The system consists of three main parts: the accelerator head, a power supply and control rack, and a separate heat exchanger/chiller. The rack consists of a 2 kW high-voltage power supply running at a maximum of 120 kV with vacuum and gas controlling gauges and interface controls. The entire system is computer controlled by a user-friendly program and has optional capabilities and controls for pulsed operation where a variety of parameters can be selected by the user (pulse length, rise/fall times, dwell time, etc.). The system control unit constantly monitors the system condition and also employs many interlocks for user safety; the interlocks are both mechanical (e.g., on the doors of the generator room) and functional (e.g., if the beam current gets too high) [39]. A few primary specifications of the D+D generator, as operated, are shown in Table 6.

Table 6. Specifications of the Adelphi Technology Incorporated DD108 Neutron Generator.

Property	Value
DD neutron yield	1×10^8 n/second maximum
Neutron energy	≈2.45 MeV
Operating mode	Continuous
Accelerator voltage	100 kV
Operating beam current	3 mA

Testing the Spectrometer.

Four runs were performed with the spectrometer in the D+D generator. Each run consisted of two parts: the first part corresponding to layers 01-04 and the second part consisting of layers 05-08 (which are identical to layers 01-04) with the 5 cm block of paraffin wax moderator placed in front of the assembly. The first run was performed for two hours on each half of the spectrometer (totaling four hours) and the second run was conducted for a total of eight hours. This second test was conducted to get a higher value of counts and to improve statistics; the cadmium shield was not used for the first series of tests. The third and fourth tests were both performed with the spectrometer placed inside a cadmium shell, lasting eight hours and twenty hours, respectively. An outline of the tests is shown in Table 7.

Table 7. Overview of the four tests performed to commission the neutron spectrometer in the D+D neutron source.

Test #	Date Performed	Run Time [HRS]	Cadmium Shell
1	10/20/2012	(2+2)=4	NO
2	10/23/2012	(4+4)=8	NO
3	11/07/2012	(4+4)=8	YES
4	11/19/2012	(10+10)=20	YES

During testing, the spectrometer was placed as close to the tube head as possible in order to get the highest flux of directional neutrons perpendicular to the front

face of the detectors. The next chapter will report the results of the spectrometer commissioning runs, the resulting unfolded spectrum and an overview of the unfolding method.

V. Results

The results of the commissioning runs are discussed below. The spectrometer data is reported and compared to simulated Geant4 values. Finally, the spectrometer data is unfolded with MAXED to determine if the resultant spectrum has an acceptable fit with the known energy of the mono-energetic neutron source.

5.1 Commissioning Test Results

The results of commissioning runs 01, 02, 03 and 04 are shown below in Figs. 44, 45, 46 and 47, respectively. With the exception of the second commissioning run, the peak value of the simulated data in each of the plots has been scaled to match the

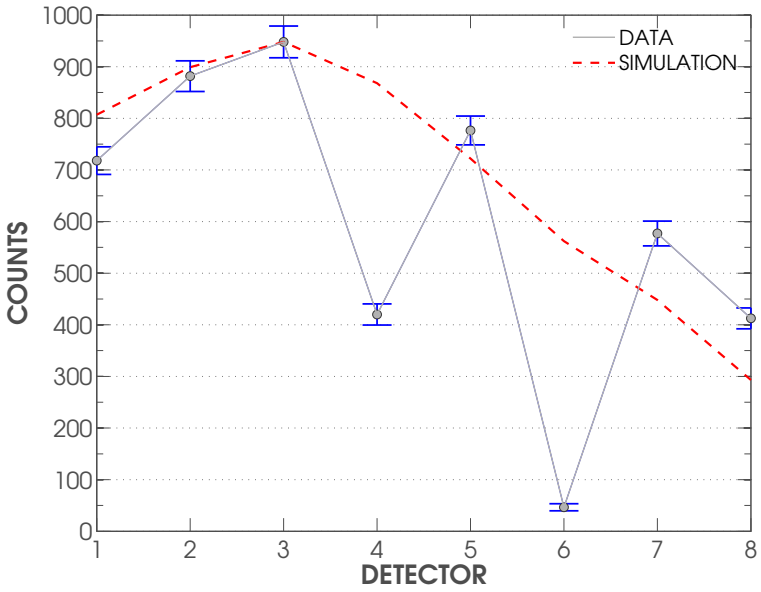

Figure 44. Results of the first commissioning run of the spectrometer. The run was conducted twice: the first time for two hours, then again for another two hours with the appropriate thickness of moderator in front of the assembly to represent the first four layers. This setup was run twice in order to simulate an eight-layer spectrometer and to increase the resolution of the output spectrum. The counts in each detector versus the layer number (or detector number) are plotted. The peak of the simulated data has been scaled to match the peak of the experimental values. The experimental plot appears to follow the general shape of the simulated curve with the exception of two values that are significantly lower than expected.

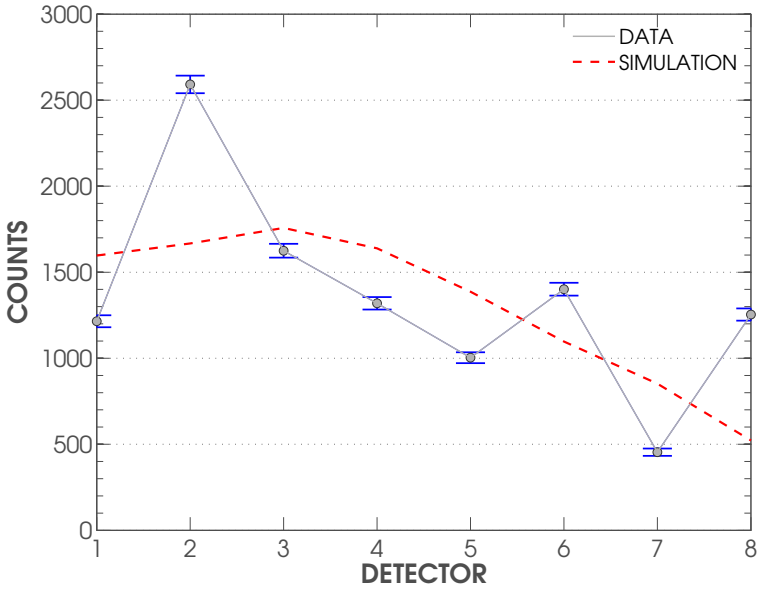

Figure 45. Results of the second commissioning run of the spectrometer with the D+D neutron source. The run was conducted twice: the first time for four hours, then again for another four hours with the appropriate thickness of moderator in front of the assembly to represent the first four layers. This setup was run twice in order to simulate an eight-layer spectrometer and to increase the resolution of the output spectrum. The counts in each detector versus the layer number (or detector number) are plotted. The detector was not surrounded by cadmium for this test run, which according to simulations, is the cause for the poor fit to the simulated data.

peak value of the experimental data. The second run was not peak matched because of the spike in layer 02 of the experimental data. Following the second commissioning run, and as a result of the spike in layer 02, the subsequent commissioning runs were conducted with the spectrometer wrapped in a 1 mm thick cadmium shell. As the particle visualization reveals in Fig. 35, significant levels of thermalization and reflection occur within the shielded environment of the D+D generator. The neutrons that are reflected within the shielded environment of the D+D generator and make it back to a LiF detector are not a result of thermalization occurring as a consequence of the moderator in the spectrometer and can therefore give results that do not agree with the simulations.

Commissioning run #1 was the first attempt at operating the spectrometer in

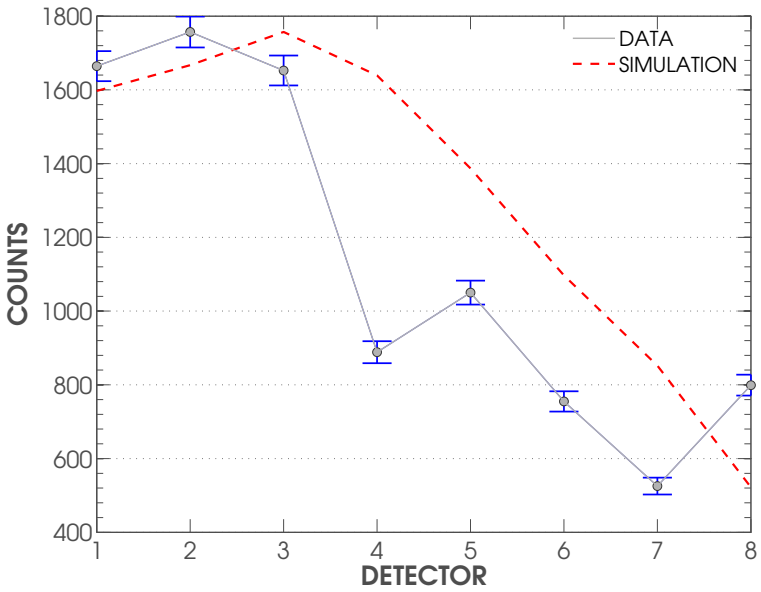

Figure 46. Spectrum was created following eight hours of testing the spectrometer with a cadmium shell and shows the results of the third commissioning run. The peak of the simulated data has been linearly scaled to match the peak of the spectrometer data. The entire curve appears to be shifted slightly to the left of the simulated data.

a known neutron environment. The experimental data followed the shape of the simulated curve, however, the experimental data from both layer 04 and layer 06 registered well below expectations. The adjusted R-squared value of the fit registered at 0.1798, and hence was not acceptable. Although R-squared values are arbitrary and largely depend of the testing parameters, only values over 0.70 were considered acceptable for the validation of the spectrometer.

Run #2 was accomplished in order to get better statistics; the run was accomplished with a total collection time of eight hours as opposed to four and the spectrometer was moved as close to the D+D generator as possible to maximize the directional component of the neutrons parallel to the long-axis of the spectrometer. The results of the second commissioning run are shown in Fig. 45. The adjusted R-squared value of the fit was maximized at 0.2008 and the peaks of the experimental and simulated data were not matched to each other. After the commissioning run #2, the Geant4

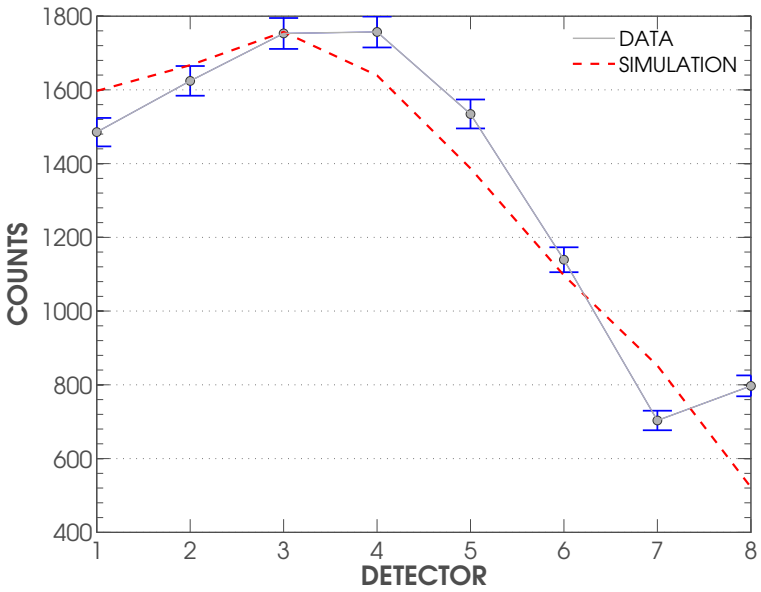

Figure 47. Spectrum was created following 20 hours of data collection with the D+D neutron generator and the spectrometer surrounded by a 1 mm thick cadmium shell and shows the results of the final commissioning run. The peak of the simulation results has been linearly scaled to match the peak of the spectrometer data; the two data sets were then plotted side-by-side. It can be seen that the experimental spectrum is slightly shifted with respect to the simulation results and that there is an unfounded spike in the counts of layer 08.

simulations were altered in order to determine why the simulations were deviating significantly from the experimental results. Troubleshooting the poor fits began with improving the simulations as opposed to altering the test setup because the preliminary simulations were very elementary and did not incorporate the environment of the D+D generator. Improving the simulations by adding the borated polyethylene into the simulation revealed the problem of the thermal neutrons scattering back toward the spectrometer and creating additional counts in select detectors. The results of the first two commissioning runs led to a review of the simulations and resulted in the conclusion that a cadmium shell around the spectrometer is crucial to block the scattered neutrons from the borated polyethylene shielding in the D+D generator.

Commissioning run #3 (shown in Fig. 46) matched the simulated data better, however, it still had a low adjusted R-squared value of only 0.39. While the adjusted

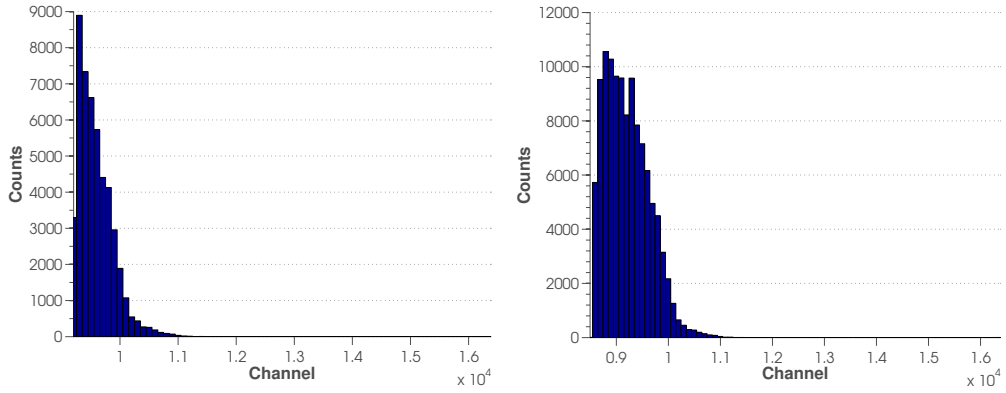

Figure 48. Difference in the discrimination levels between commissioning runs #3 and #4. The x-axis of the plots show the channel (or magnitude) of pulse from the shaping amplifier. Fig. A (left) shows the histogram from layer 03 of commissioning run #3 and Fig. B. (right) shows the histogram from layer 03 of commissioning run #4 with a lower discrimination value. Notice the larger total area of Fig. B as a result of the lower value.

R-squared value improved from the first two commissioning runs, it was still not acceptable. After looking into the experimental instrumentation, it was found that some of the discrimination values were much higher than they should have been and some of the neutron counts were therefore being considered noise and disregarded. The MATLAB® script written to evaluate the spectrometer data allowed for easy adjustment of the discrimination levels, even post-data collection. Figure 48 shows the difference between the discrimination of layer 03 from run #3 to run #4. Discrimination of the detectors was originally set by the user, however the value changes over time because of the varying noise levels around the generator. Upon discovering the problem with the discrimination levels, the MATLAB® code was re-written to automatically adjust the discrimination levels based on where the counts start from the higher-energy reaction products. This trough is shown experimentally in Fig. 22; the higher-energy reaction products are beyond the noise level far enough that a cusp is created where the noise ends and the neutron signal begins. Evaluating Fig. 48, the discrimination value was set far beyond the noise (Fig. A). After fine-tuning the MATLAB® analysis code to automatically adjust the discrimination levels, the

experimental data fit the simulations much better and the adjusted R-squared value of 0.89 in the fourth commissioning run (20 hours total), shown in Fig. 47, supports the conclusion. The most significant deviation between the experimental and simulation data in the fourth commissioning run occurred in layer 08, where the experimental counts were over 25% larger than expected. The deviation in layer 08 could not be accounted for within the simulations or otherwise and was taken as erroneous measurement in the unfolding procedure. In the following section, the resultant experimental spectrum of run #4 is unfolded to reveal the associated energy spectrum.

5.2 MAXED Spectrum Unfolding

An important consideration for the spectrometer data is that the resultant spectrum is a convolution of the contribution from neutrons of multiple energies. In order to determine the energy spectrum of a neutron source, it is necessary to 'unfold' the resultant spectrum. The program MAXED (MXD_FC33), obtained from the Radiation Safety Information Computational Center (RSICC), was used to unfold the spectrum. MXD_FC33 applies the maximum entropy principle to the unfolding problem and has the ability to be run in 'few-channel' mode (FC) or 'multi-channel' mode (MC). The FC program can analyze sets with up to 100 measurements and can handle fluence vectors with up to 1000 energy bins. The MC program can analyze data sets with up to 4096 measurements and can handle fluence vectors with up to 4096 energy bins. The unfolding procedure taking place herein, for the validation of the spectrometer, has only eight detectors with less than 100 energy bins; the FC program will therefore be sufficient and is referred to for the purpose of this document [40].

Table 8. Control file line designators.

Line Number	Description	Value Used
1	Name of file with input data	dat_spec.ibu
2	Name of file with response functions	resp_fun.fmt
3	Name of output file	mxfc_001
4	Name of file with default spectrum	def_spec.flu
5	Highest energy of the solution spectrum	5
6	Requested final chi^2 per DOF (max.)	1.0
7	Temperature and temperature reduction factor parameters	1.0,0.85
8	Energy bin structure for unfolding, Solution spectrum bins	3,2
9	Choice of scaling the default spectrum	1
10	Choice of changing the MXD_FC33 scale factor	0

The Code and Input Files.

The code was initially written for 'unfolding' the spectrum from a multi-sphere neutron spectrometer though it is also applicable to this layered spectrometer because of the essentially identical operation of the two devices. The following section will describe the input files to run the MAXED program.

MAXED was written in Fortran 90 and compiled with the Compaq Visual Fortran compiler. The program UMGPlot, which is used to visualize the results of MAXED, was written using the programming environment ComponentOne Studio for ActiveX. MAXED has the option to run using a control file or alternatively can be run interactively. The unfolding accomplished for this report was done using a control file. The control file is 10 lines in length and specifies each of the parameters needed to successfully run MAXED; these designators are specified in Table 8.

The temperature and temperature reduction factor parameters in item 07 (Table 8) are parameters used by the simulated annealing optimization subroutine. The temperature parameter can be set to 1.0 in almost all cases. The value of 0.85 is recommended for the simulated annealing temperature reduction factor parameter [40]. In item 08, there are several options for the energy bin structure; these options

are outlined in Table 9. For record 9, the options are specified by the binary 0 or 1; '0' meaning to not apply a scale factor and '1' meaning to scale the default spectrum. Line 10 is designated equivalently to line 09 (binary).

Table 9. Available options for line 08 of the control file.

Option	Description
0	Use a fine energy bin structure
1	Four bins per decade
2	Energy bin structure of the default spectrum
3	Energy bin structure of the response functions

The control file is just the first of four necessary files to run the algorithm. A file with the spectrometer's data is supplied by the user and requires fields for the number of measurements and a description of each measurement. The file with the measured data is outlined in Table 10. Line number 03 (a-g) is repeated for each measurement (the number of measurements specified in line 2).

The '2x' in line 02 of Table 10 simply identifies two spaces. The next logical step would be to define the response functions. The method for inputting the response functions is very similar to that of the measured data. The format for the file is specified in Table 11. Line 03 requires the specification of energy units (this is the

Table 10. Measured data file line designators.

Line Number	Description	Value Used
1	Header (80 characters)	Spectrometer Data
2	Number of measurements and correction factor	8 2x 0
3a	8 Character ID	0W0
3b	Moderator thickness (cm)	1.25
3c	Measured data	2.878E+04
3d	Uncertainty due to statistics (absolute units)	1.696E+02
3e	Uncertainty due to statistics (percentage)	0.59
3f	Other uncertainties (percentage)	2.0
3g	A "flag" to describe the data	0

Table 11. Response functions file line designators.

Line Number	Description	Value Used
1	Header (80 characters)	Response Functions
2	Header (80 characters)	Response Functions
3	Energy bin edges in response function, units of E	22 2x 1
4	The energy bin edges in the response function	1.000E-08 2x 1.000E-07 ...
5	Dummy variable (DV)	0
6	Number of response functions	8
7a	Response function ID, comments	0W0
7b	DV, units of response function, 7 DVs	1.000E+00, 0,...,0
7c	The responses for the layer	4.784E+05 2x 3.047E+05 ...

first time units has come into the algorithm). Table 12 outlines the values to specify certain units of energy. A '1' was used throughout the unfolding algorithm to specify that each spectrometer measurement was defined in terms of MeV. The purpose of this file is to input the response functions for use in the unfolding procedure. Records 7a,b and c will be repeated for all response functions in this file (the number specified in line 06).

Option	Description
0	eV
1	MeV
2	keV

Table 12. Available options for specifying units of energy.

The final file describes the default spectrum. The default spectrum supplies the a priori information which is crucial for the 'few channel' case, where the number of detectors is much smaller than the number of energy bins used for the unfolding. The approach used in MAXED can be justified on the basis of arguments that originate in information theory and allows for the inclusion of a priori information in a well-defined and mathematically consistent way [41]. In addition to having a sound theoretical basis, this approach has other features that have proven to be useful from a more practical point of view: it makes use of the estimated variance for each detector's count

Table 13. Default spectrum functions file line designators.

Line Number	Description	Value Used
1	Header (80 characters)	Default Function
2	Form of default spectrum, Units of energy	2,1
3	DV, number of bins, max energy	2 2x 47 2x 10.00E+00
4	Energy bin edge, bin magnitude	1.000E-08 2x 0.0E+00 ...

rate in the unfolding process, appropriately weighting the data from each detector. The algorithm leads to a solution spectrum that is always a non-negative function and can be written in closed form [41]. The default spectrum file layout is outlined in Table 13.

The 'form of the default spectrum' as specified in line 02 of the default spectrum file can be defined by several values as outlined in Table 14. The default spectrum defined for this unfolding was defined as *fluence rate per bin* since it was concentrated around the thermal and 2.45 MeV energy regions. Record 04 is repeated for each bin edge and bin.

Option	Description
1	$d\phi/dE$
2	Fluence rate per bin
3	$(E\ d\phi)/dE$

Table 14. Available options for specifying the 'form of the default spectrum'.

The Algorithm.

The MAXED algorithm used in MXD_FC33 is a maximum entropy algorithm which can be described in terms of a set of input parameters, a set of output parameters and the equations relating these quantities [42]. In practice, the algorithm is formulated in discrete terms with n energy bins that are labeled with index i. As-

suming m detectors that we label with index k, a set of admissible spectra are defined using two restrictions:

$$N_k + \epsilon_k = \sum_i R_{ki} f_i \tag{46}$$

and

$$\sum_k \frac{\epsilon_k^2}{\sigma_k^2} = \Omega, \tag{47}$$

where:

N_k is the measurement,

ϵ_k is the difference between the measured and predicted value for detector k,

R_{ki} is the response function for detector k,

f_i is the solution spectrum,

σ_j is the estimated standard uncertainty and

Ω is a parameter set by the user to obtain a specific Chi-squared value.

Equation (46) is an integral equation that relates the measurement to the detector's response function and the neutron spectrum, allowing for a measurement error. Equation (47) is a constraint for handling the ϵ_k and assumes that the Chi-squared statistic of the solution is equal to a value determined a priori by the user. From the array of admissible spectra, the ideal response is one that maximizes the entropy S of the distribution:

$$S = -\sum_i \left[f_i ln\left(\frac{f_i}{f_i^{DEF}}\right) + f_i^{DEF} - f_i \right], \tag{48}$$

where f_i^{DEF} is the default spectrum that contains the a priori information. The maximization of S with constraints given by Equations (46) and (47) is equivalent to

maximization of a potential function $Z(\lambda_k)$ with respect to a set of m parameters λ_k [43]. The solution spectrum f_i and the solution for ϵ_k can be written in terms of λ_k:

$$f_i = f_i^{DEF} exp\left[-\sum_k \lambda_k R_{ki}\right] \tag{49}$$

and

$$\epsilon_k = \frac{\lambda_k \sigma_k^2}{2}\left(\frac{4\Omega}{\sum_j (\lambda_j \sigma_j)^2}\right)^{1/2}. \tag{50}$$

To find the values of λ_k that maximize Z, the simulated annealing algorithm for the few-channel case is applicable here. The algorithm requires the input of N_k, σ_k, f_i^{DEF}, R_{ki} and Ω and calculates output parameters λ_k. Since the maximum entropy solution can be written in closed form, one can use Equations (46-49) to calculate the effect of small changes in the input parameters [40]. Any change in the input parameters will lead to a change in the output parameters λ_k, which in turn will lead to a change in the f_i and the ϵ_k calculated from Equations (48) and (49).

5.3 Unfolded Spectrum- Final Results

To obtain an unfolded spectrum, it is first necessary to compile a library of response functions. 22 Geant4 simulations of 1.0×10^7 neutrons were run in order to span the entire applicable energy range with a resolution of 0.5 MeV from 0→5 MeV. The library of functions is plotted and shown in Fig. 49; two plots were used because of the wide range in energies covered. The functions were applied in the MAXED format previously described with a specified energy resolution of 0.5 MeV. A higher resolution spectrum would have been possible, however, only at the cost of the statistics. An under-defined solution is only made possible because of the maximum entropy application of MAXED.

After applying the MAXED software and unfolding the spectrometer data from

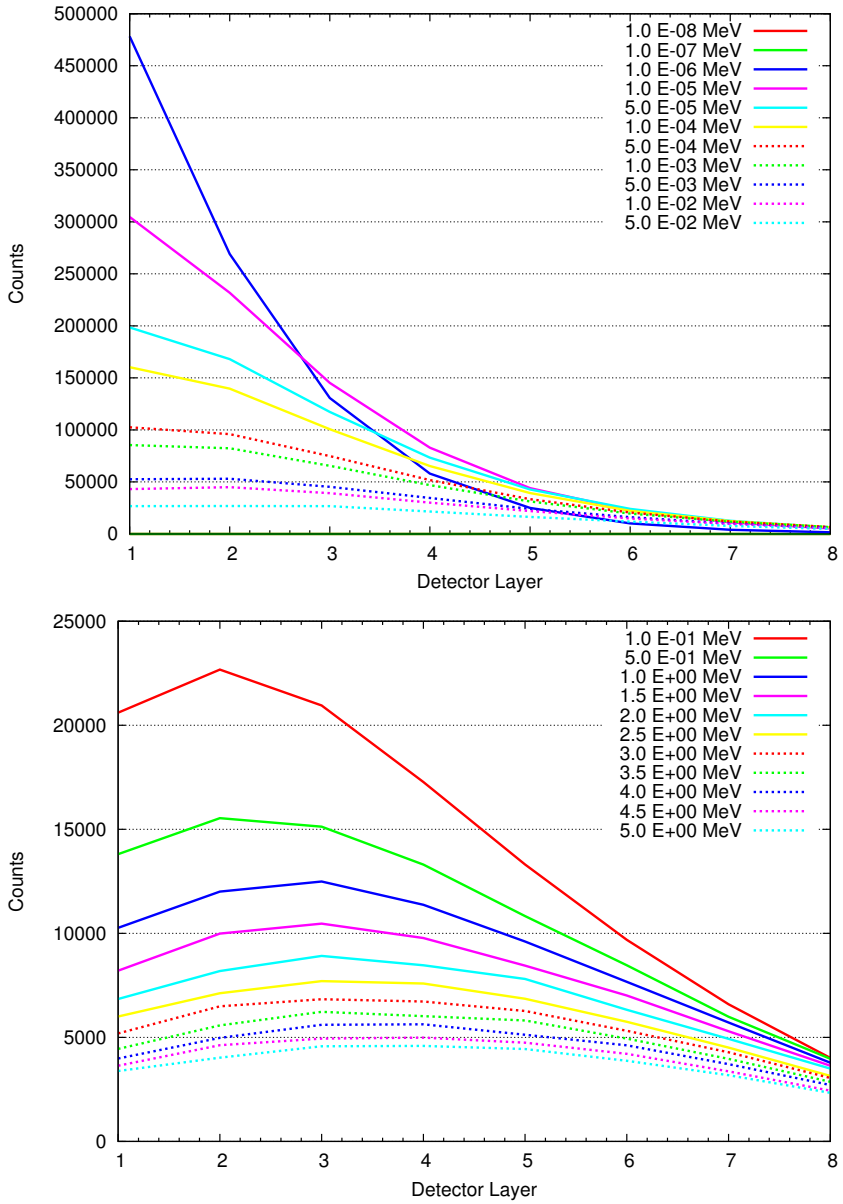

Figure 49. Library of response functions as a result of running 22 Geant4 simulations, each with 1.0×10^7 neutrons. Fig. A (top) is the first set of 11 functions showing 1-11 of 22. The first two functions (*red* and *green*) do not appear in the figure because neutrons of this energy are primarily stopped by the cadmium and do not register many counts. Fig. B. (bottom) is the second set of 11 functions showing 12-22 of 22.

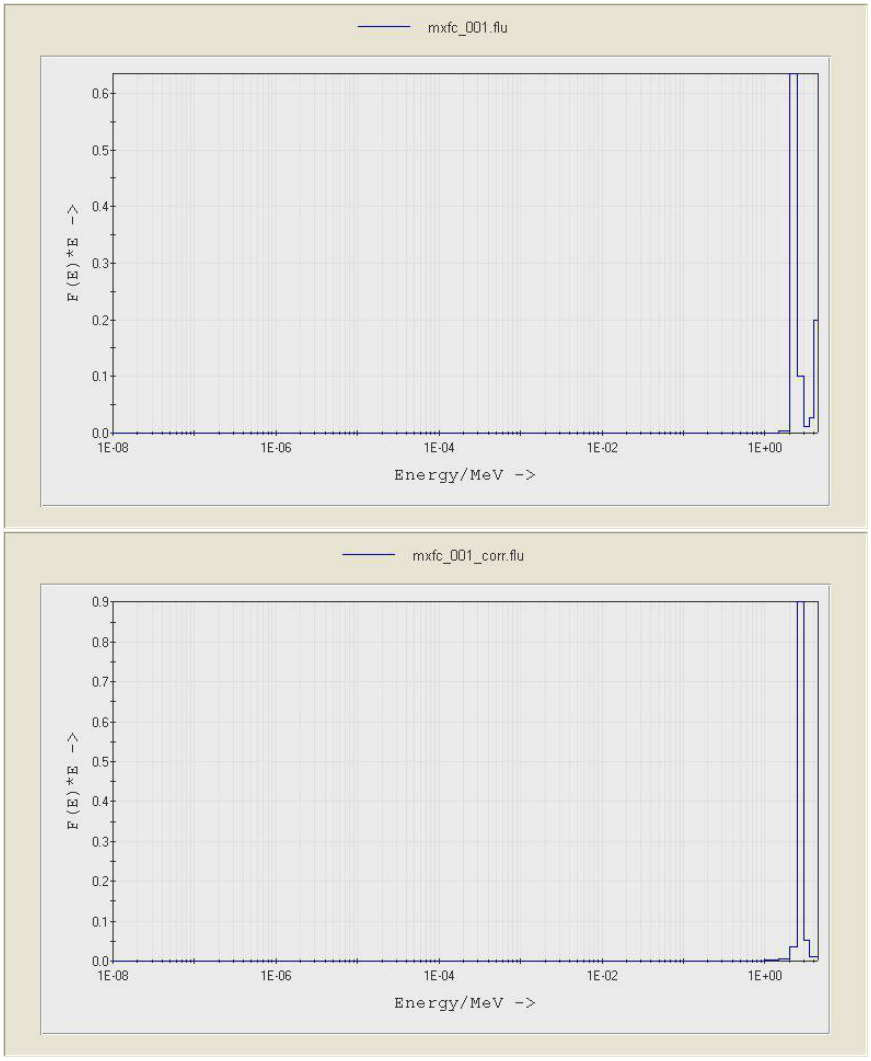

Figure 50. Fig. A (top) shows the unfolded energy spectrum using MAXED and the experimental spectrum shown in Fig. 47. The unfolding was accomplished using a library of response functions derived from multiple Geant4 simulations (shown in Fig. 49). The peak above 4 MeV is a result of the unfounded peak in layer 08 of the experimental data. With the exception of the >4 MeV peak, the histogram is concentrated between 2→3 MeV, as expected. Fig. B. (bottom) shows the unfolded energy spectrum using MAXED and the experimental spectrum shown in Fig. 47. The unfolding was accomplished using a library of response functions derived from multiple Geant4 simulations (shown in Fig. 49). This unfolding is identical to that of Fig. A (above) with the exception of the 'weight' of importance placed on layer 08. Layer 08 was essentially disregarded in the unfolding procedure, yielding an energy spectrum that would be expected from the mono-energetic D+D neutron source.

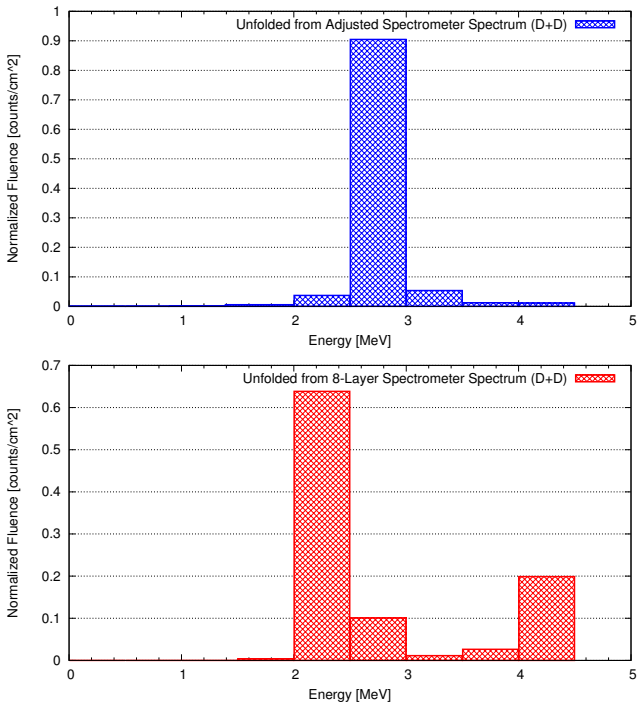

Figure 51. Unfolded energy spectra of the D+D neutron source located at AFIT building 194 as determined by the aforementioned spectrometer. The top figure shows the spectrum from the experimental spectrometer data of the fourth commissioning run with a 95% error applied to layer 08 in order to discount the unexplained peak in counts and the bottom figure shows the uncorrected data from the same run.

the final commissioning run (#4), the spectrum shown in Fig. 50A (top) resulted. Looking carefully, it is evident that there is a peak on the far right side of the figure. This peak is a result of the count increase in layer 08 of the final commissioning run. This increase in counts has not been accounted for in the simulations or otherwise; it is likely a result of a physical phenomenon such as neutrons reflecting within the cadmium case of back wall of the D+D shielding and being detected in the back layer of the spectrometer. To disregard this peak, the layer 08 value was input into the unfolding code with 95% uncertainty resulting in a new unfolded spectrum shown in Fig. 50B (bottom).

This spectrum looks much more like the expected spectrum (a mono-energetic peak at 2.45MeV). Figure 51 shows a comparison of the two unfolded spectra. The top figure represents the data of the corrected spectrum and the bottom figure represents the data of the uncorrected spectrum. Interpolating amidst the two figures, the energy of the peak is between the 2 $\rightarrow$ 2.5 MeV energy bin and the 2.5 $\rightarrow$ 3.0 MeV energy bin, which is appropriate considering the actual energy is $\approx$2.45 MeV. The Chi-squared value of the corrected spectrum to that of a 2.45 MeV mono-energetic peak is 0.374/D.O.F., indicating that the mono-energetic peak shown in Fig. 50B is statistically probable and should not be rejected as a possible source spectra. Chi-squared statistics are used because the unfolding problem is essentially under-defined; there are many solutions that can potentially fit the response library. Each identifiable source must be modeled in order to provide the necessary response libraries for the unfolding algorithm. In the case of a poly-energetic source, which was the next endeavor with the spectrometer, the experimental spectrum must be unfolded against a library of known responses (the poly-energetic source must be modeled). If the spectrometer were to be used to identify an unknown source of neutrons, the experimental spectrum would be collected and unfolded against a variety of known libraries. After unfolding against each of the known libraries, the neutron spectra with the best statistical fit to the experimental spectrum will be assumed to be the source of the neutrons, assuming the statistics are within the acceptable range of the Chi-squared test.

The problem of identifying poly-energetic neutron sources is explored in the next section. The same eight-layer spectrometer is used to identify an un-shielded PuBe source at a range of $\sim$1 meter.

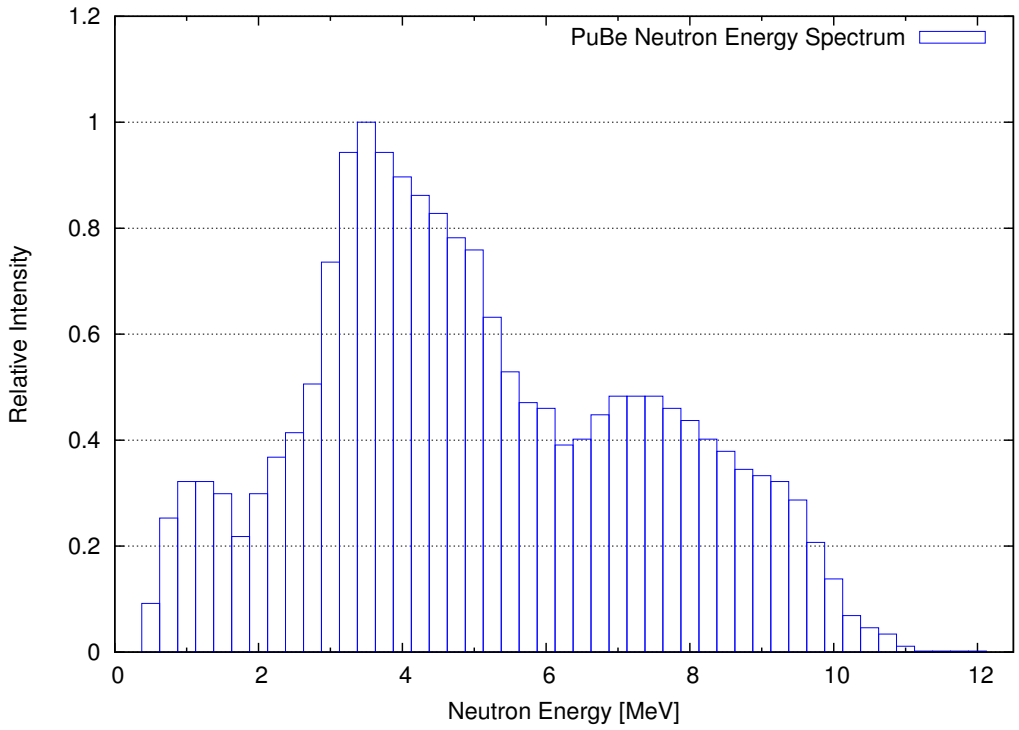

Figure 52. Typical neutron energy spectrum of a Plutonium-Beryllium spontaneous fission/(α,n) neutron source [1].

5.4 Post-Commissioning Spectrometer Tests

This section explores the applicability of the eight-layer spectrometer to identify poly-energetic neutrons sources. The ability to identify more-complex neutron signatures is pertinent for the use of the spectrometer in Department of Homeland Security applications where a primary goal in the organization is to differentiate neutrons emitted from varying SNMs and neutrons that exist as a result of the cosmic background. A minimalistic approach has been taken to identify the neutron sources with a spectrometer consisting of only eight layers. This provides only eight data points to the unfolding algorithm, which is used to determine the probability that an experimentally derived spectrum matches the spectrum of a known SNM.

Testing the spectrometer with a poly-energetic neutron signature was accom-

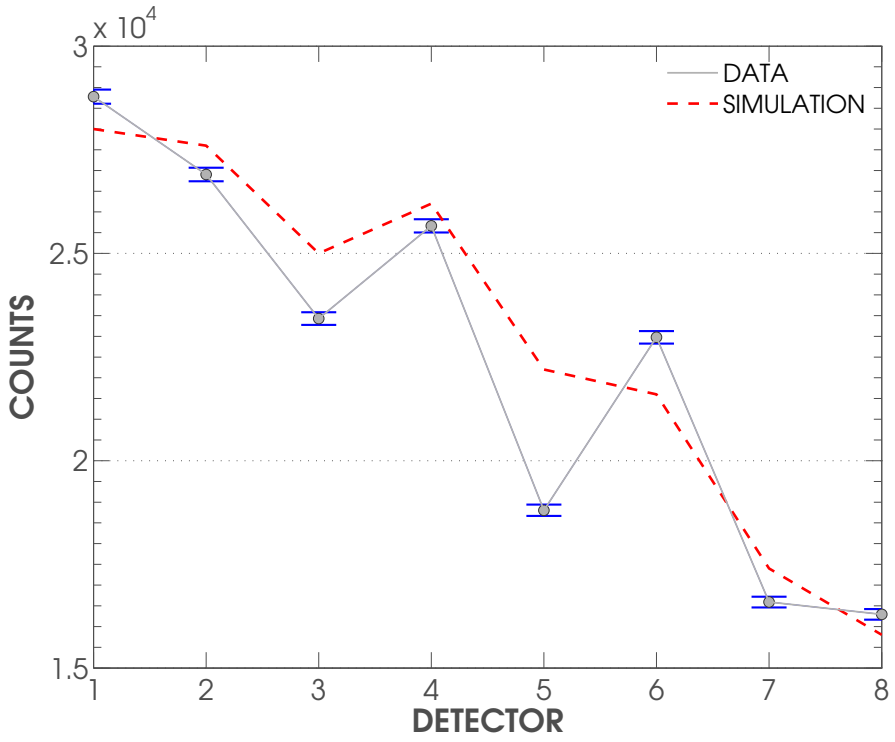

Figure 53. PuBe testing results using the eight-layer spectrometer. The spectrum was created following 52 hours of data collection with the 4888 mCi source placed at a distance of eight inches from the front face of the spectrometer (which was surrounded by a 1 mm cadmium shell). The experimental results appear to match the simulation results well with an adjusted R-squared value of 0.8842 and the total counts varying by only 2.37 %. Additionally, the crests and troughs of the two curves align in corresponding detectors.

plished with an un-shielded PuBe source in the basement of building 470. The response library created for the D+D commissioning tests is still applicable to this scenario since the spectrometer was not modified; the energy range of the library, however was expanded to 10 MeV (up from 5 MeV) in order to cover the majority of neutrons ejected from the PuBe source. The neutron energy spectrum of the PuBe source is shown in Fig. 52. The spectrum was obtained using foil activation and contains neutrons that are both spontaneously fissioned from the ^{239}Pu (although minimal) and as a result of the (α,n) reaction via [44]:

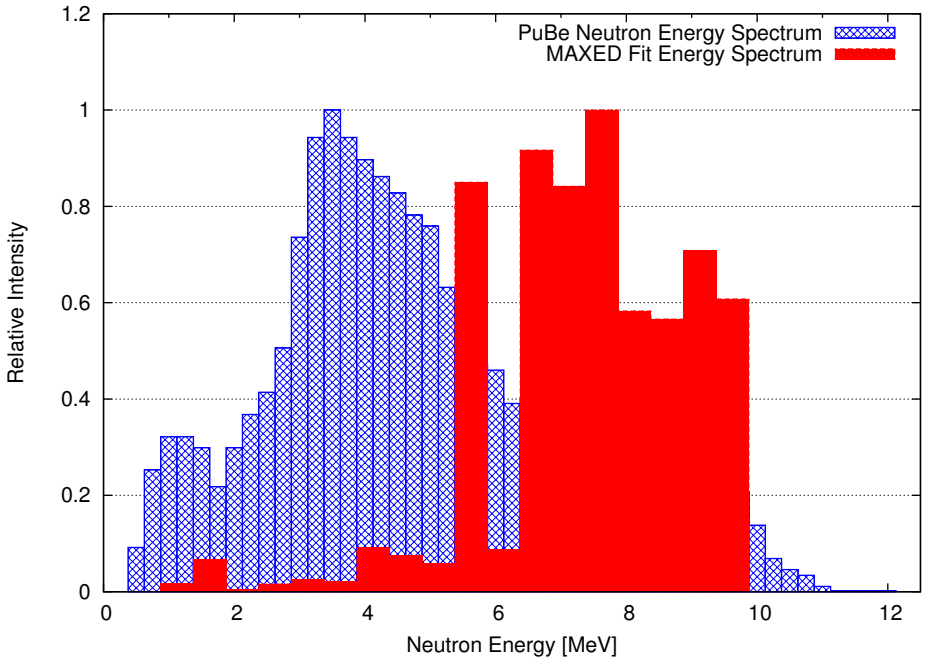

Figure 54. MAXED was used to unfold the spectrometer's eight point data into a neutron spectrum using the libraries shown in Fig. 49 (extended to 10 MeV). The default spectrum, shown in *blue*, is the input spectrum of the PuBe source, in which MAXED tried to fit the output spectrum to, which is shown in *red*. The resultant Chi-squared value is 0.9622/D.O.F., which corresponds to a chance probability of 0.3266.

$$^{4}_{2}\mathrm{He} + ^{9}_{4}\mathrm{Be} \longrightarrow ^{12}_{6}\mathrm{C} + ^{1}_{0}\mathrm{n}. \tag{51}$$

The PuBe source used for testing had a born-on date of 23 June 1960 and an initial activity of 4895 mCi. With the large half-life ($T_{1/2}$) of ≈24,100 years [44], the activity during testing was approximately the same as the original at 4888 mCi. The closest point of the PuBe source was placed eight inches from the front-face of detector 01 in the spectrometer and the experimental setup was identical to the commissioning test setup shown previously in Fig. 39. After 52 hours (26 hours with each half) of data collection with the source, the results were analyzed and plotted against the Geant4 simulations; this plot is shown in Fig. 53. The two curves appear to follow the same trend, with the crests and troughs matching in corresponding detectors and

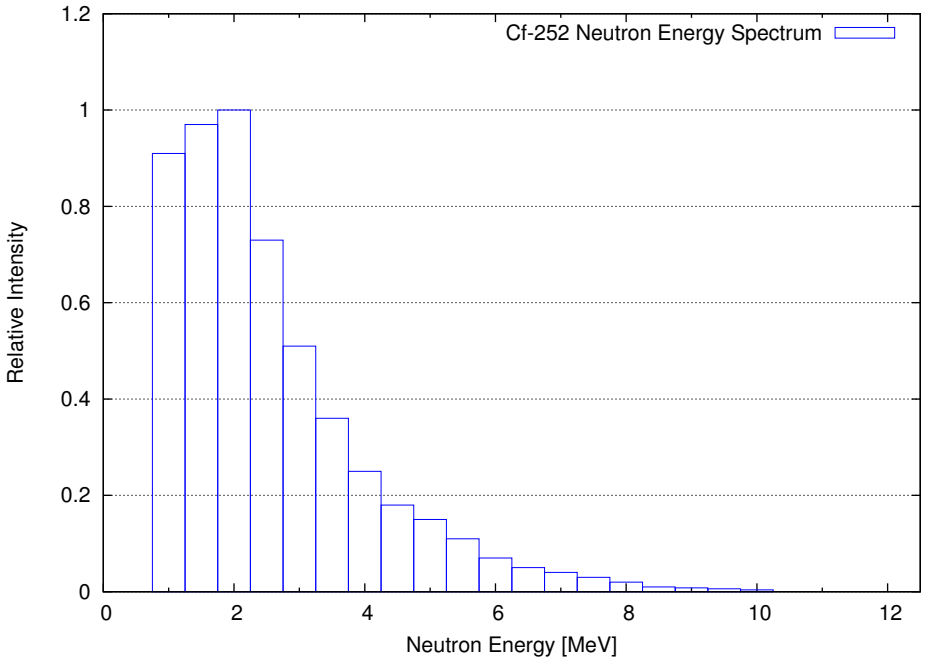

Figure 55. Typical neutron energy spectrum of a californium-252 (^{252}Cf) spontaneous fission neutron source [2].

an R-squared value between the experimental and simulation data of 0.8842. The peaks of the two curves were not aligned in this plot; instead, the data was scaled to maximize the R-squared value. By scaling the simulation results, the resultant difference in counts between the two curves is only 2.37 %. The error bars depict only the counting error ($\sqrt{n}$) and do not take into account the instrumentation and discrimination error as this was not quantified.

Preparing MAXED, the input files were updated to depict the spectrum of the PuBe source (Fig. 52), the libraries were updated to range from 0 $\rightarrow$ 10 MeV and the experimental data was logged; execution of the program resulted in Fig. 54. Using only eight data points, the unfolded spectrum identifies that the source of neutrons is on the same order of magnitude as the default PuBe spectrum. Whether this accuracy is acceptable or not depends on the application of the spectrometer. The Chi-squared value of the output spectrum (the unfolded spectrum) to that of

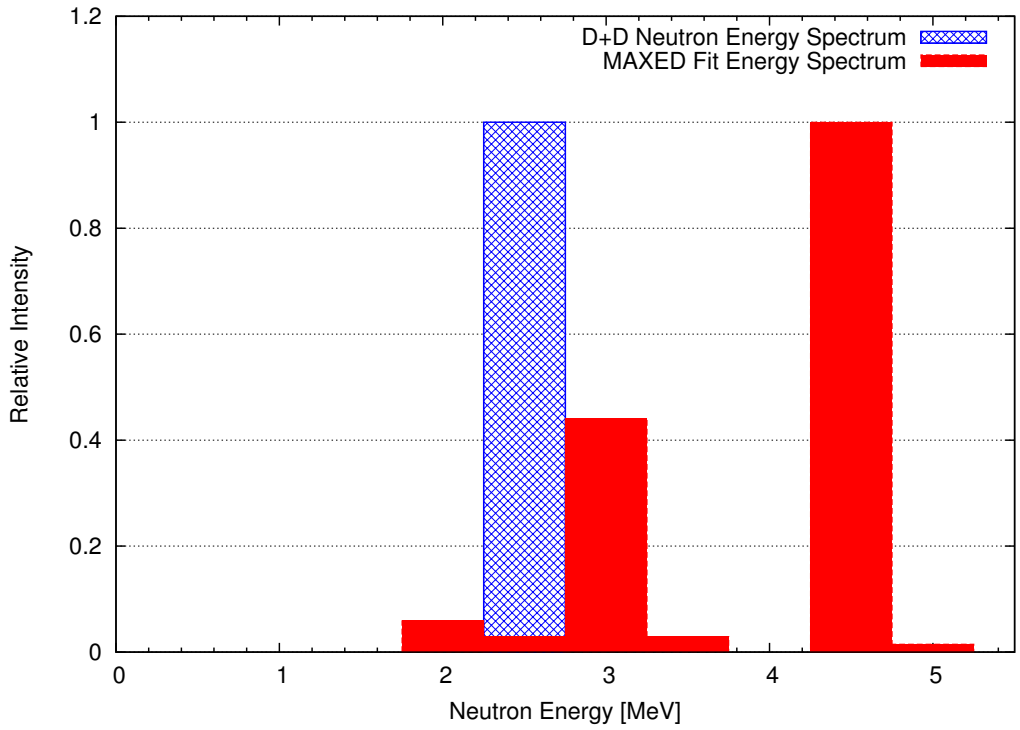

Figure 56. MAXED was used to unfold the spectrometer's eight point data into a neutron spectrum using the libraries shown in Fig. 49 (extended to 10 MeV). The default spectrum, shown in *blue*, is the input spectrum of the D+D neutron generator, in which MAXED tried to fit the output spectrum to, shown in *red*. The resultant Chi-squared value is 1.910/D.O.F., which corresponds to a chance probability of 0.1669.

the default spectrum is 0.9622/D.O.F., which corresponds to a chance-probability of 0.3266. The name 'chance-probability' in this case is a bit deceiving, it is essentially the probability that the deviation between the experimental and expected spectra is a result of only chance. In radiation detection problems, this is often an acceptable fit as values between 0.05 and 0.95 are typically deemed adequate; however, when trying to identify a specific SNM which has a neutron spectrum on the same order of magnitude as PuBe, this would not be sufficient. As shown in Fig. 54, the unfolding favors neutrons from 5.5 $\rightarrow$ 10 MeV.

Fortunately, identifying specific SNM does not necessarily require that the unfolded spectrum exactly fit the source spectrum. Using the minimalistic approach

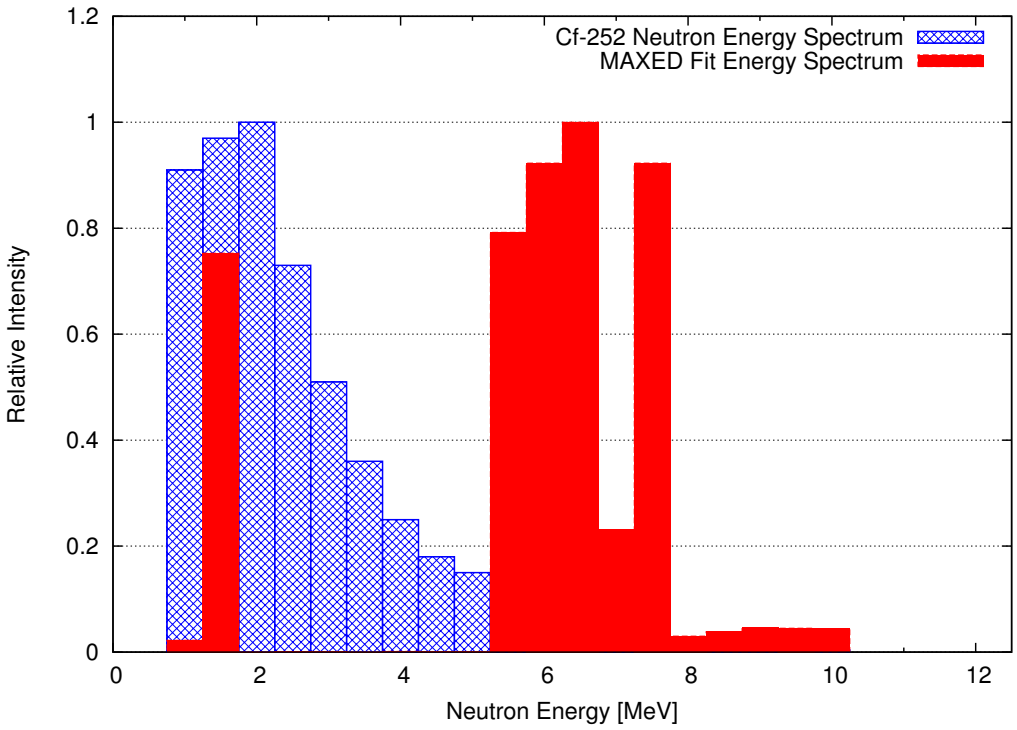

Figure 57. MAXED was used to unfold the spectrometer's eight point data into a neutron spectrum using the libraries shown in Fig. 49 (extended to 10 MeV). The default spectrum, shown in *blue*, is the input spectrum of the Cf-252 source, in which MAXED tried to fit the output spectrum to, shown in *red*. The resultant Chi-squared value is 1.032/D.O.F., which corresponds to a chance probability of 0.3096.

taken here, it is not likely that the exact spectrum will be de-convoluted with only eight data points. MAXED was used to unfold the spectrometer data against several different default spectra to analyze which of the source spectra resulted in the best statistical fit. Since the D+D neutron spectrum was already formatted into MAXED, this spectrum was used in addition to the common californium-252 (^{252}Cf) spontaneous fission neutron spectrum. The ^{252}Cf spectrum is shown in Fig. 55. The first unfold was accomplished against the D+D mono-energetic neutron spectrum and the results are shown in Fig. 56. Again, the output spectrum is shown in *blue*. The unfolding algorithm appears to have gotten the best statistical fit with a peak at $4 \rightarrow 5.0$ MeV, however the Chi-squared value of the output spectrum is almost double that of

the PuBe spectrum at 1.910/D.O.F. The next unfold was against the ^{252}Cf spectrum and the results are shown in Fig. 57. The resultant output spectrum is similar to that of the PuBe output spectrum in that the peak is dominant between 5.5 $\rightarrow$ 8.0 MeV, and much of the data is within an order of magnitude. The Chi-squared value of the ^{252}Cf output spectrum is 1.032/D.O.F. While the PuBe source does indeed have the best statistical fit of the three cases evaluated herein, the fits of both the PuBe and the ^{252}Cf are within 7% and cannot be differentiated with certainty. If the sources were not labeled, one may be able to use the eight-layer spectrometer to identify a source based on statistics and accurate response libraries; however, this would likely come with many 'false identifications'. The results of the unfolding comparison are shown in Table 15.

Table 15. Unfolding results using eight-layer spectrometer data against three different default spectrums.

Default Spectrum	χ^2/ D.O.F.	Chance-Probability
PuBe	0.9622	0.3266
D+D	1.910	0.1669
^{252}Cf	1.032	0.3096

Looking back up to Fig. 53, even though the plot has been scaled to maximize the R-squared value, not one of the experimental data points fall within the error limits of the simulated data points. Many of the features of the source neutrons are lost when the minimalistic approach is taken. This problem would likely be solved using a spectrometer with more layers, however the detection problem often comes down to determining the accuracy that is necessary to resolve the energy, type, speed, mass, etc. of the intended particle. In a deployable situation where the device size matters, the minimalistic approach is often desirable; however there are trade-offs and, in this case, the energy resolution of the neutron energy spectrum is severely limited.

VI. Conclusions

The results of this research appear to be promising; 2.45 MeV mono-energetic neutrons have been identified successfully after unfolding experimental data produced by an eight-layer spectrometer consisting of alternating layers of paraffin wax and LiF thin-film semiconductor neutron detectors. The materials used to produce the spectrometer are all fairly inexpensive and the spectrometer itself is both durable and portable. The LiF detectors used in the spectrometer construction are robust and have been shown to achieve neutron detection efficiencies upwards of 25% while readily discriminating against background γ-ray radiation [18].

In order to determine the field applicability of the spectrometer, an attempt was made to show that the spectrometer can achieve enough resolution to differentiate common SNM neutron signatures with sufficient accuracy. Following poly-energetic PuBe source testing, it is not likely that the eight-layer spectrometer will be adequate for identifying SNM with signatures within an order of magnitude. The eight-layer spectrometer was able to statistically differentiate the PuBe source from both a Cf-252 and D+D neutron source, however the unfolded spectra were only accurate within an order of magnitude. The MAXED fits between the PuBe unfolded spectra and the Cf-252 unfolded spectra varied by only 7%. The ability to differentiate the different SNM signatures with confidence at large stand-off distances is paramount because of the background neutron radiation and moderation/reflection occurring in the atmosphere. Further studies should be conducted with a spectrometer of more layers (12, 16, 32, etc.) to determine the point at which the common SNMs can be identified with low uncertainties; this may also involve incorporating many detectors on each layer of the spectrometer for an increased detection efficiency and better counting statistics.

Thin-film semiconductor detectors are state of the art with respect to neutron detection and offer several benefits for homeland security applications. Semiconductor

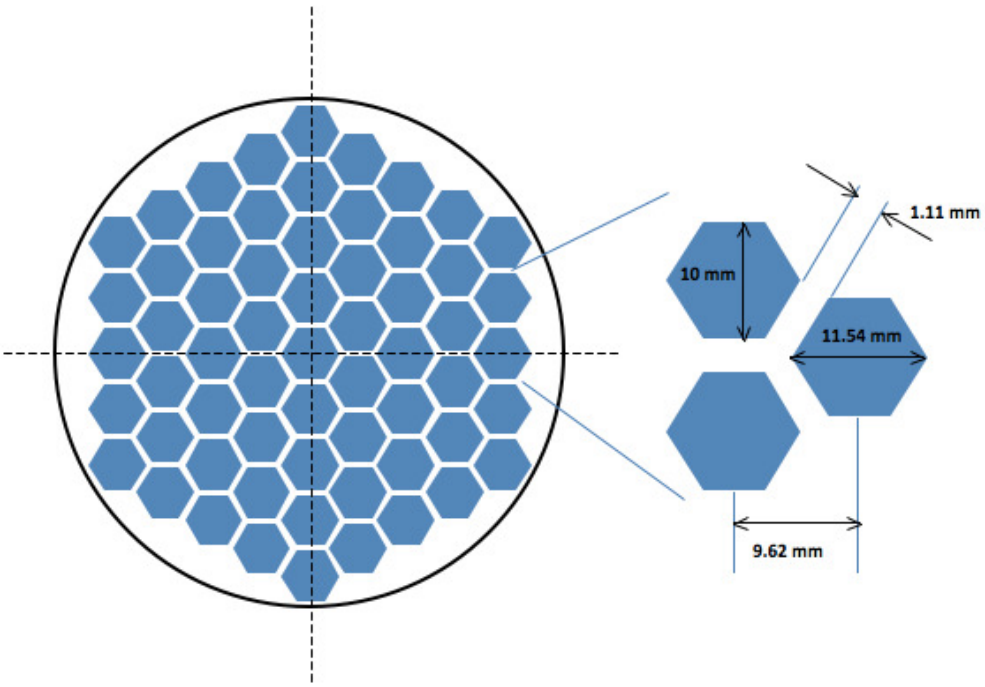

Figure 58. Hex design for the improved pixelation and symmetry of the neutron spectrometer. The future design will have built-in preamplifiers to simplify the electronics.

detectors offer the advantage of being small in size as opposed to BF_3 tubes (which can extend to meters in length), do not contain pressurized gases, do not require high voltages and in some cases, they can operate on the intrinsic built-in voltage and do not require an external voltage at all. Several materials have been proposed for use as a neutron converter film; the converter materials are either coated on the semiconductor as a film or packed into perforations. Lithium fluoride was used for this research because of the higher-energy reaction products (2.055 and 2.73 MeV), allowing for a thicker neutron conversion layer and simplifying the process for discriminating against background radiation. One disadvantage of lithium, compared to both boron and gadolinium is the lower thermal neutron detection cross section (detection efficiency). This decrease in efficiency is a disadvantage indeed, however, it can be compensated for by using multi-layer detectors.

As with most radiation problems, simulations play an important role in validating

a physical model. Geant4 simulations were used throughout this research to model the response of neutrons as they interact and penetrate through the eight-layer spectrometer. The simulations helped not only to guide in the optimized thickness of moderating material, but also in developing the response library vital to the MAXED unfolding algorithm. A useful application of the model was also revealed using the visualization macro to view the particles as they were tracked through the geometry of the spectrometer; if modeled correctly, areas of reflection/interaction can be foreseen, potentially aiding in the troubleshooting and optimizing of the device.

Future designs have been proposed to improve pixelation of the detectors within the layers of the spectrometer. Hex-shaped features allow for a maximum number of pixels on the improved wafers while achieving good symmetry and low detection dead-space. Features like this can allow the spectrometer to be used not only for neutron energy analysis, but can provide directional information as well. The design shown in Fig. 58 is currently being built by S.M.A.R.T. Laboratories and incorporates built-in pre-amplifiers. Other proposals to improve the spectrometer design include optimizing moderator thickness to tailor the spectrometer to a specific energy, increasing the number of layers and even using variable moderator thicknesses from layer-to-layer to concentrate the energy resolution in a specific range.

VII. Appendix A- Additional Plots

This appendix includes additional plots not presented in the body of the report. Several tests were performed with the LiF detectors and with the spectrometer that provided supporting information in order to guide the research to its resultant path. Some of the plots are more informative than others and very little formatting has been accomplished.

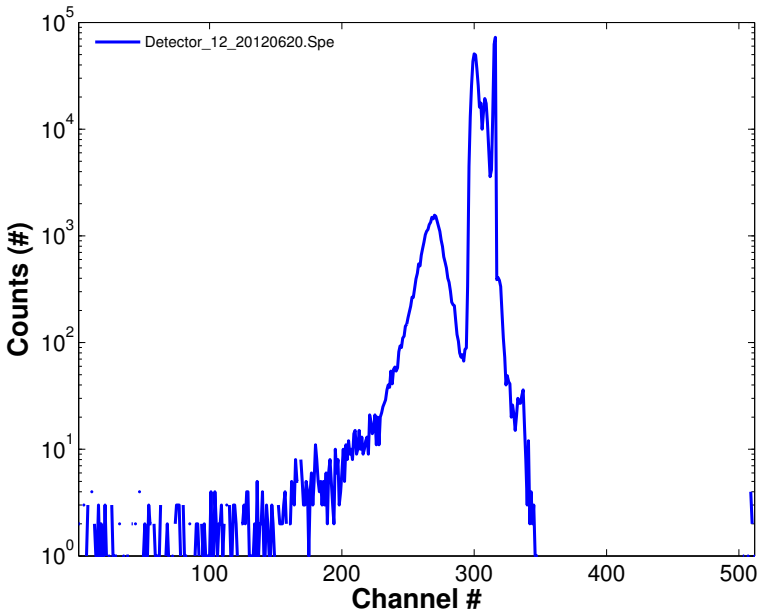

Figure 59. A 12 hour test with binary detector 12 in the graphite pile at FS-7. Total counts can be found by integrating the area under the curve over a specific range. This is the type of signal that will be output by the new devices currently being fabricated by S.M.A.R.T. Laboratories. This type of device is easy to work with because of the binary output signal, the device simply needs to be calibrated for efficiency differences from device-to-device (or pixel-to-pixel).

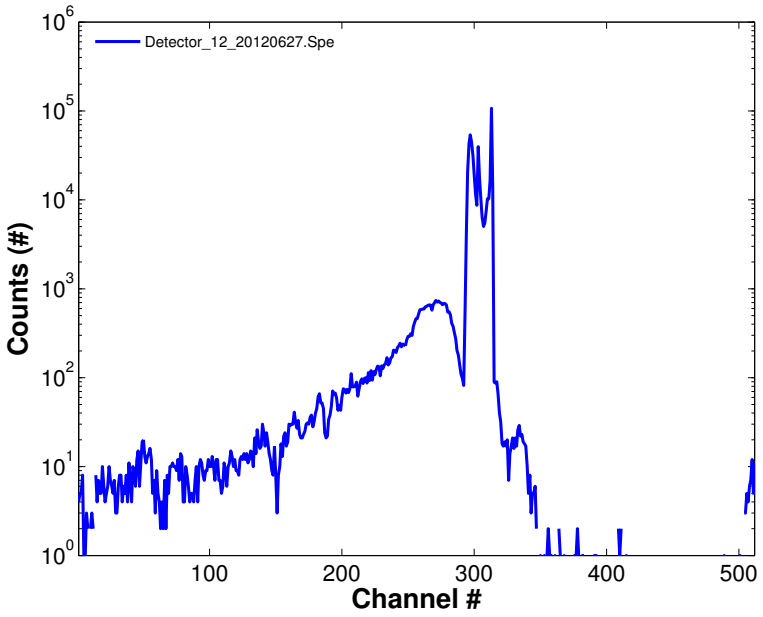

Figure 60. A 12 hour test with binary detector 12 (1m wire as opposed to a 3m wire in Fig. 59) in the graphite pile at FS-7. The first peak was reduced as a result of using a shorter lead wire from the actual detector, this is potentially a result of less noise pick-up from the extended length of cable.

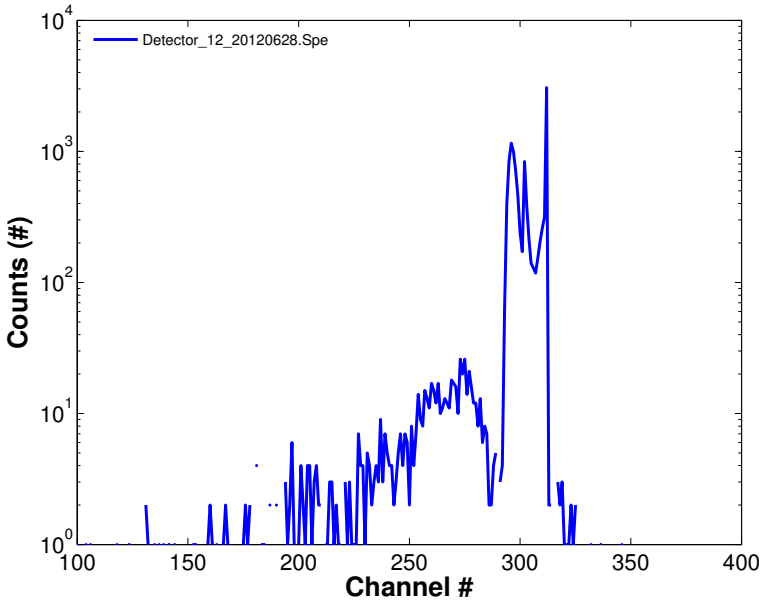

Figure 61. A 12 hour test with binary detector 12 (1m cable length) in the graphite pile at FS-7, wrapped in Cd. This test was useful to determine how the detector reacts to the thermal neutron flux. The trough stayed approximately stable at channel 300, whereas the magnitude of the primary peak decreased two orders of magnitude. This reduction in signal is a result of the thermal neutron flux.

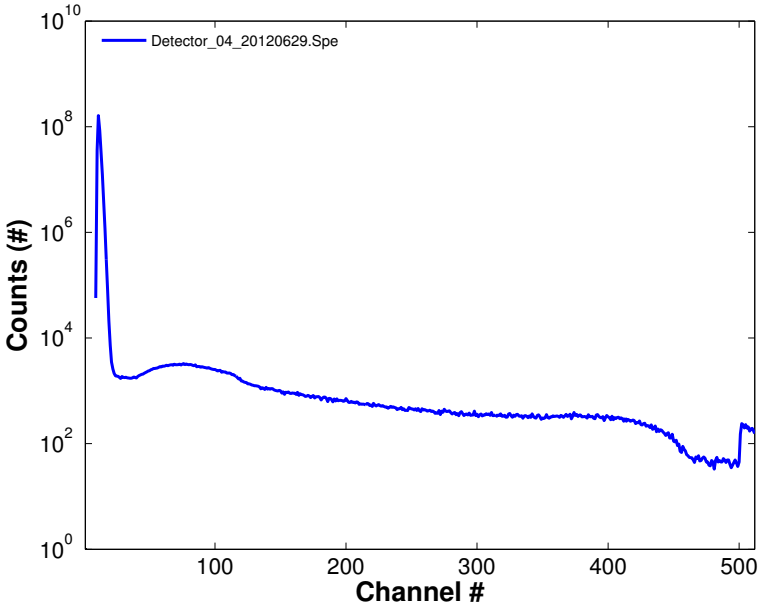

Figure 62. 12 hour test of detector 04 in the graphite pile at FS-7, without Cd. Not all of the tests gave elegant results. It took several runs to get the instrumentation configured. Many of the expected features are still evident in the plot.

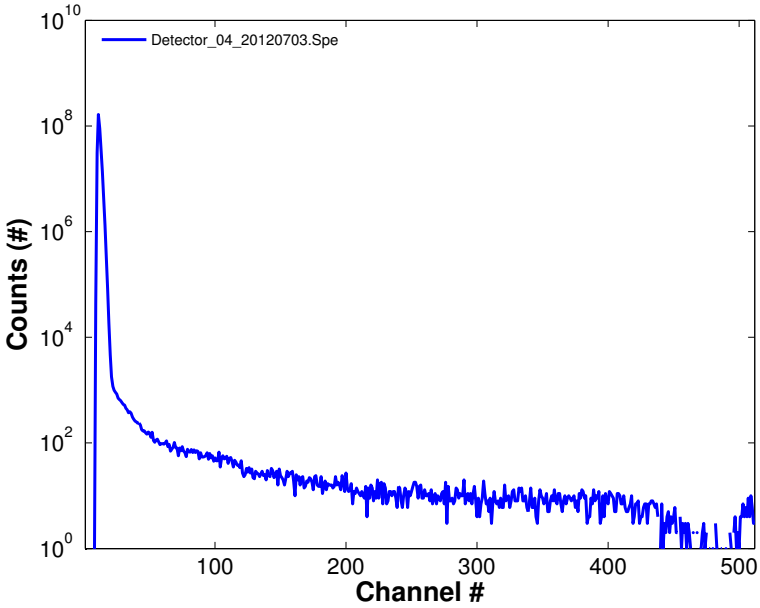

Figure 63. 12 hour test of detector 04 in the graphite pile, with Cd. Comparing this figure to Fig. 62, the reduction in signal (two orders of magnitude), is proof that the detectors have a good response to thermal neutrons.

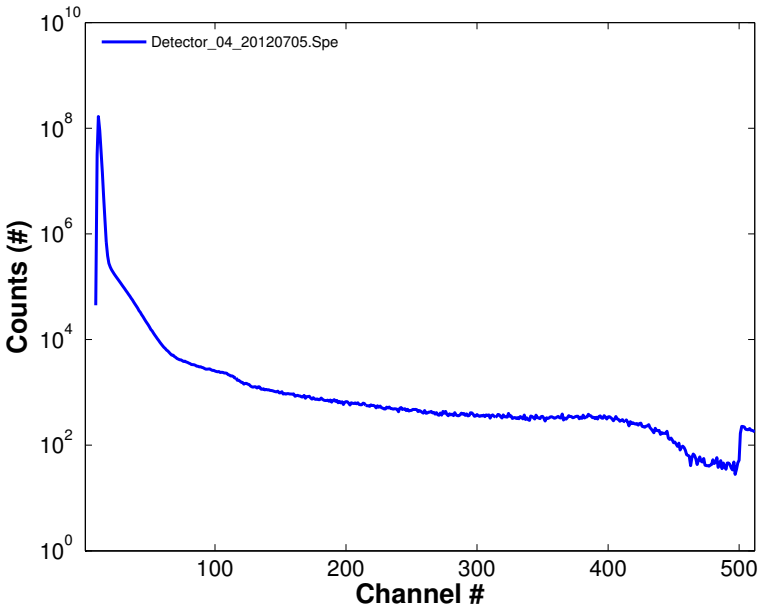

Figure 64. 12 hour test of detector 04 in the graphite pile, without Cd and with a Co-60 source for evaluation of γ-ray response. Again, comparing this figure to Fig. 62 shows how the detector response changes as a result of exposure to a Co-60 γ-ray source. There is very little change in signal past the discrimination point.

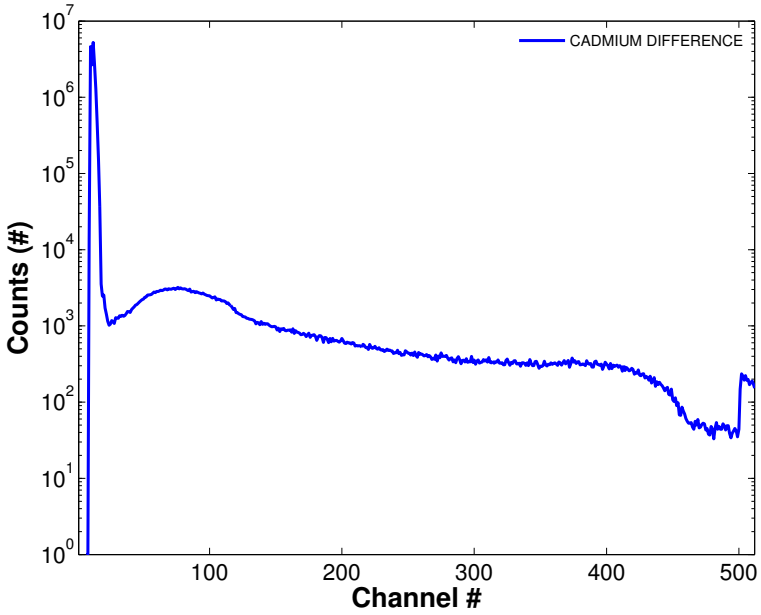

Figure 65. Detector 04's response to the thermal neutrons. Test was conducted over a 12 hour period in FS-7 of the graphite pile. This figure is a result of taking the difference between Fig. 62 and Fig. 63. It is apparent that the bulk of the original signal is a result of the thermal neutron flux.

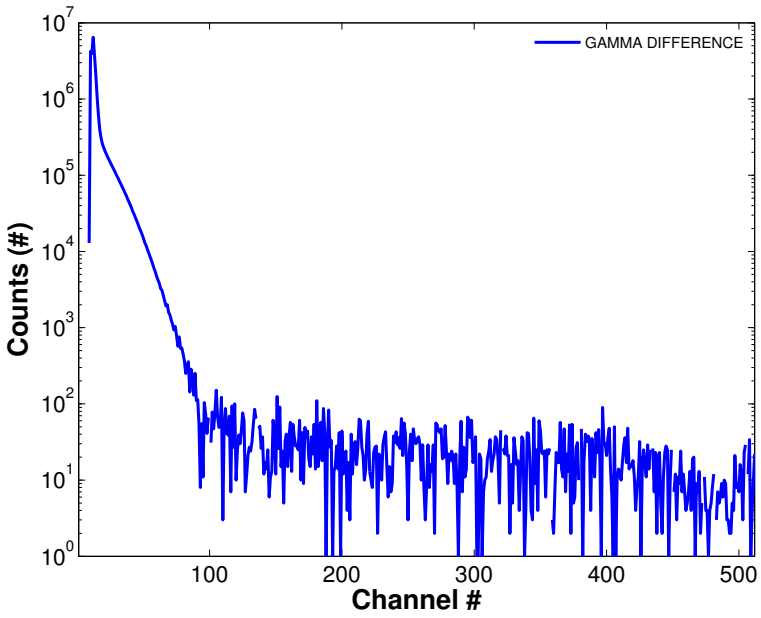

Figure 66. Detector 04's response to the Co-60 γ-rays. Test was conducted over a 12 hours period in FS-7 of the graphite pile. The signal is essentially just noise, except for the addition to the first 100 channels.

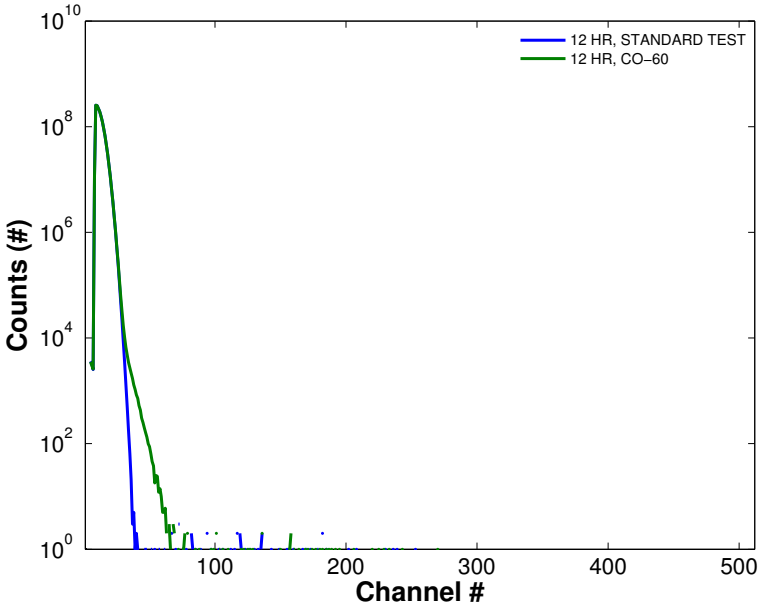

Figure 67. Two tests conducted with detector 06 removed and isolated from the graphite pile. The first test was conducted with the Co-60 source present and the second was performed with the source removed. The *blue* line represents only background and the *green* line represents the Co-60 source present. Test was conducted for 12 hours.

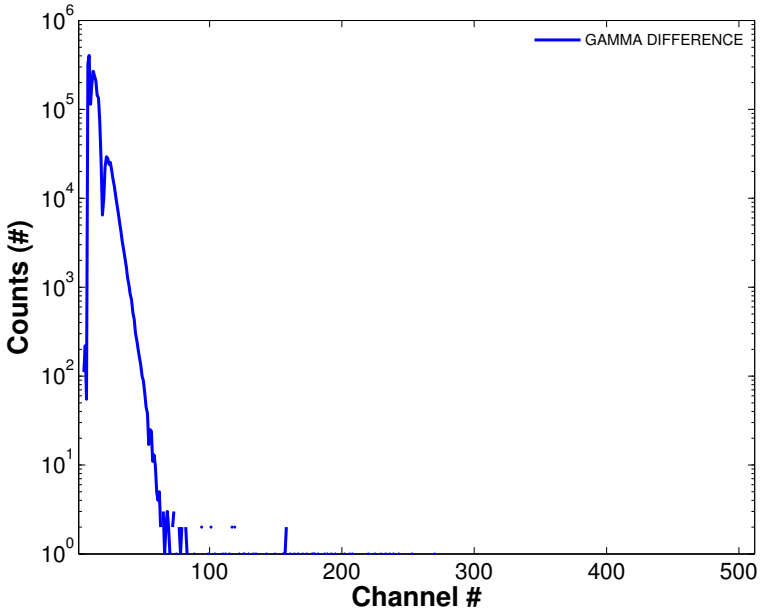

Figure 68. Gamma-ray response of detector 06. The detector was isolated from the graphite pile for the duration of the test. This figure is a result of subtracting the *blue* line from the *green* line in Fig. 67. The signal from the γ-rays is evident in only the first 100 channels.

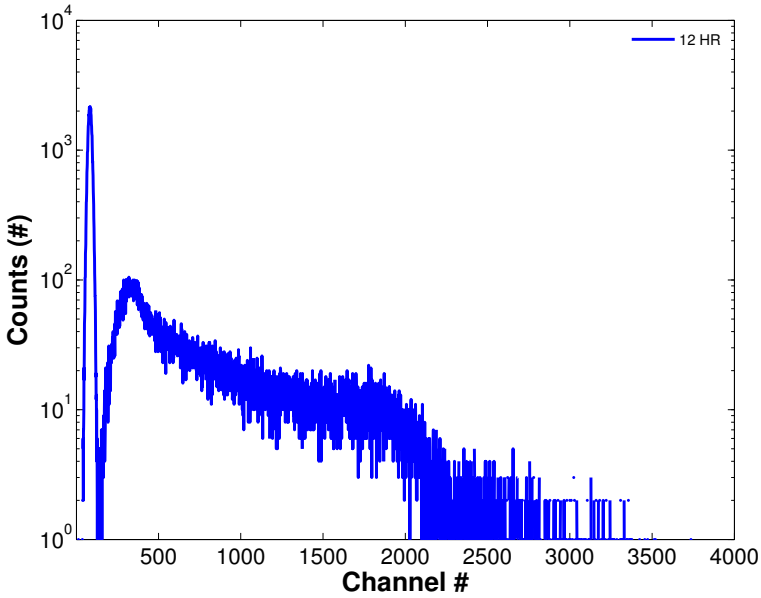

Figure 69. Results of 12 hour test conducted in the thermal neutron pile with detector #04. Amplification was set at 100x and the detector was in position FS-7. This is how the signal looks when not smoothed using the Savitzky-Golay smoothing method.

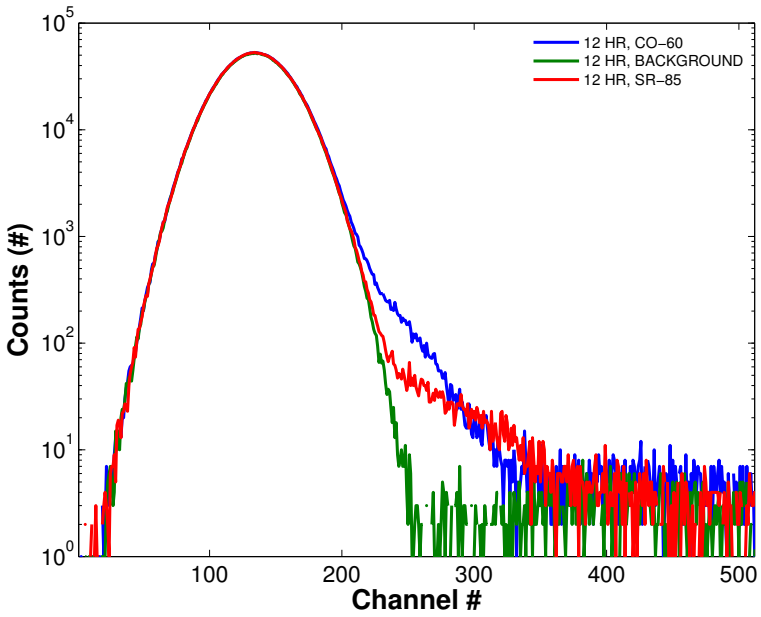

Figure 70. Results of 12 hour γ-ray sensitivity test. Three separate runs were conducted: one for background, one with a Sr-85 source and one with a Co-60 source. Detectors #01, 04, 06 and 08 were used with an amplification setting of 100x. A definitive response to the γ-rays is witnessed in the semiconductor, however the effects are evident only below channel 500. This allows for easy discrimination from the Li+neutron reaction products.

VIII. Appendix B- Foil Activation Physics

The foil activation process that was used to determine the thermal neutron flux of the graphite pile in the basement of building 470 on WPAFB starts with the reaction of a neutron and indium nucleus:

$$^{115}_{49}\mathrm{In} + \mathrm{n} \rightarrow ^{116}_{49}\mathrm{In}.$$

This unstable nucleus decays via β^- emission. The change in radioactive nuclei, as a result of the neutron irradiation, is given by:

$$\frac{d\mathrm{N}^{'}}{dt} = \phi_{th}\mathrm{N}\sigma_{act} - \lambda\mathrm{N}^{'}.$$

$\mathrm{N}^{'}$ is the number of radioactive nuclei present,

t is the time [sec],

ϕ is the thermal neutron flux [cm^{-2}-sec^{-1}],

N is the number of target nuclei in the sample,

σ_{act} is the activation cross section and

λ is the decay constant [sec^{-1}].

When a sample is irradiated to saturation, $d\mathrm{N}^{'}/dt$ approaches zero. As the number of radioactive nuclei stabilizes, the rate of activation is equal to the rate of decay:

$$A_s = \lambda\mathrm{N}_s^{'} = \phi_{th}\mathrm{N}\sigma_{act}.$$

$N_s^{'}$ is the number of radioactive nuclei at saturation. From this relationship, if A_s can be measured while N and σ_{act} are calculated, then ϕ_{th} can be determined from known information [32]. Upon taking several corrections into account, indium foil activation

was used in 2009 by J.D Daniel and S.R. McHale [32] to determine that the thermal neutron flux at position FS-7 is 2664 cm^{-2}-sec^{-1} with an anticipated increase of $\approx$ 2% per year.

Bibliography

1. L. Stewart, "Neutron spectrum and absolute yield of a plutonium-beryllium source," *Physical Review*, vol. 98, no. 3, pp. 740–743, 1954.

2. HTSL, "Californium-252," *QSA Global*, 2010. [Online]. Available: http://www.qsa-global.com/sources/industrial-isotopes/californium-252.aspx

3. S. R. McHale, "The effects of rare earth doping on gallium nitride thin films," Ph.D. dissertation, Air Force Institute of Technology, 2011.

4. DTRA and U. S. Strategic Command Combating WMD, "Nuclear detection and forensics," vol. 2012, no. 11/12, 2012.

5. Subcommittee on Standards, "A national strategy for cbrne standards," Committee on Homeland and National Security, Tech. Rep., May 2011. [Online]. Available: http://www.whitehouse.gov/sites/default/files/microsites/ostp/chns_cbrne_standards_final_24_aug_11.pdf

6. S. A. M. El-Mongy and W. A. M. El-Gamal, "Determination of pu-239 for nuclear material safeguards verification purposes," in *Radio Science Conference, 1999. NRSC '99. Proceedings of the Sixteenth National*, 1999, pp. H10/1–H10/7, iD: 1.

7. K. S. Krane, *Introductory Nuclear Physics*, 2nd ed. United States of America: John Wiley and Sons, Inc., 1988.

8. National Nuclear Data Center (NNDC), "Chart of the Nuclides." [Online]. Available: http://www.nndc.bnl.gov/chart/chartNuc.jsp

9. "National Institute of Standards and Technology (NIST)." [Online]. Available: http://www.nist.gov/index.html

10. C. J. Bridgman, "Introduction to the physics of nuclear weapons effects," *Defense Threat Reduction Agency*, vol. 8725, Fort Belvoir, VA 2001.

11. A. A. Bickley, J. W. McClory, G. K. Demaree, W. H. Miller, T. M. Oakes, and J. C. Petrosky, "Design optimization of a layered boron based solid state neutron spectrometer," *IEEE Nuclear Science Symposium Conference Record*, vol. 2011, pp. 4872–4876, 2011.

12. G. F. Knoll, *Radiation Detection and Measurement*. New York: Wiley, 1979, glenn F. Knoll.; Includes indexes.

13. S. Normand, B. Mouanda, S. Haan, and M. Louvel, "Discrimination methods betwen neutron and gamma rays for boron loaded plastic scintillators," *Nuclear Instruments and Methods in Physics Research Section A: Accelerators, Spectrometers, Detectors and Associated Equipment*, vol. 484, pp. 342–350, 2002.

14. R. J. Hu, J. H. Kim, S. H. Ahn, B. Hong, M. Ito, T. I. Kang, B. I. Kim, H. C. Kim, K. B. Lee, K. S. Lee, S. Park, M. S. Ryu, and K. S. Sim, "Characteristics of boron-loaded plastic scintillators for neutron measurements," *Journal of the Korean Physical Societies*, vol. 50, no. 5, pp. 1482–1488, 2007.

15. A. N. Caruso, "The physics of solid-state neutron detector materials and geometries," *Journal of Physics: Condensed Matter*, vol. 22, no. 443201, 2010.

16. L. Ovechikina, K. Riley, S. Miler, Z. Bell, and V. Nagarkar, "Gadolinium loaded plastic scintillators for high efficiency neutron detection," *Elsevier*, pp. 161–170, 2009.

17. D. S. McGregor, M. D. Hammig, Y. H. Yang, H. K. Gersch, and R. T. Klann, "Design considerations for thin film coated semiconductor thermal neutron detectorsi: Basics regarding alpha particle emitting neutron reactive films," *Nuclear Instruments and Methods in Physics Research Section A: Accelerators, Spectrometers, Detectors and Associated Equipment*, vol. 500, no. 13, pp. 272–308, 3/11 2003.

18. D. S. McGregor, S. L. Bellinger, D. Bruno, W. L. Dunn, W. J. McNeil, E. Patterson, B. B. Rice, J. K. Shultis, and T. Unruh, "Perforated diode neutron detector modules fabricated from high-purity silicon," *Radiation Physics and Chemistry*, vol. 78, no. 10, pp. 874–881, 10 2009.

19. W. J. McNeil, S. L. Bellinger, T. C. Unruh, C. M. Henderson, P. Ugorowski, B. Morris-Lee, R. D. Taylor, and D. S. McGregor, "1-d array of perforated diode neutron detectors," *Nuclear Instruments and Methods in Physics Research Section A: Accelerators, Spectrometers, Detectors and Associated Equipment*, vol. 604, no. 12, pp. 127–129, 6/1 2009.

20. J. K. Shultis and D. S. McGregor, "Efficiencies of coated and perforated semiconductor neutron detectors," in *Nuclear Science Symposium Conference Record, 2004 IEEE*, vol. 7, 2004, pp. 4569–4574 Vol. 7, iD: 1.

21. D. S. McGregor, S. L. Bellinger, W. J. McNeil, and T. C. Unruh, "Microstructured high-efficiency semiconductor neutron detectors," in *Nuclear Science Symposium Conference Record, 2008. NSS '08. IEEE*, 2008, pp. 446–448, iD: 1.

22. S. L. Bellinger, W. J. McNeil, T. C. Unruh, and D. S. McGregor, "Characteristics of 3d micro-structured semiconductor high efficiency neutron detectors," *Nuclear Science, IEEE Transactions on*, vol. 56, no. 3, pp. 742–746, 2009, iD: 1.

23. S. Bellinger, W. J. McNeil, and D. S. McGregor, "Improved fabrication technique for micro-structured solid-state neutron detectors," *Cambridge Journal, MRS Proceedings*, vol. 1164, no. 1164-L06-01, 2009.

24. C. J. Solomon, J. K. Shultis, W. J. McNeil, T. C. Unruh, B. B. Rice, and D. S. McGregor, "A hybrid method for coupled neutron-ion transport calculations for 10b and 6lif coated and perforated detector efficiencies," *Nuclear Instruments and Methods in Physics Research Section A: Accelerators, Spectrometers, Detectors and Associated Equipment*, vol. 580, pp. 326–330, 2007.

25. J. K. Shultis and D. S. McGregor, "Design and performance considerations for perforated semiconductor thermal-neutorn detectors," *Nuclear Instruments and Methods in Physics Research Section A: Accelerators, Spectrometers, Detectors and Associated Equipment*, no. 606, pp. 608–636, 2009.

26. Q. Jahan, E. Patterson, B. B. Rice, W. L. Dunn, and D. S. McGregor, "Neutron dosimeters employing high-efficiency perforated semiconductor detectors," *Nuclear Instruments and Methods in Physics Research Section B*, no. 263, pp. 183–185, 2007.

27. B. W. Cooper, S. L. Bellinger, A. N. Caruso, R. G. Fronk, W. H. Miller, T. M. Oakes, J. K. Shultis, T. J. Sobering, and D. S. McGregor, "Neutron energy spectrum with microstructured semiconductor neutron detectors," *IEEE Nuclear Science Symposium Conference Record*, vol. R, no. 16, p. 6, 2011.

28. J. Clinton, "Optimization and characterization of a novel self powered solid state neutron detector," Ph.D. dissertation, Rensselaer Polytechnic Institute, 2011.

29. G. Lutz, *Semiconductor Radiation Detectors*, 2nd ed. Munich, Germany: Springer, 1999. [Online]. Available: http://lib.semi.ac.cn:8080/tsh/dzzy/ebooks/full/fn217.pdf

30. V. B. Zeghbroeck, "Semiconductor Fundamentals." [Online]. Available: http://ecee.colorado.edu/~bart/book/book/chapter2.html

31. C. Kittel, *Introduction to Solid State Physics*, 8th ed. Wiley, 2004.

32. J. D. Daniel and S. R. McHale, "Calculation of thermal neutron flux via indium foil dosimetery," 2009.

33. J. Allison, K. Amako, J. Apostolakis, H. Araujo, P. A. Dubois, M. Asai, G. Barrand, R. Capra, S. Chauvie, R. Chytracek, G. A. P. Cirrone, G. Cooperman, G. Cosmo, G. Cuttone, G. G. Daquino, M. Donszelmann, M. Dressel, G. Folger, F. Foppiano, J. Generowicz, V. Grichine, S. Guatelli, P. Gumplinger, A. Heikkinen, I. Hrivnacova, A. Howard, S. Incerti, V. Ivanchenko, T. Johnson, F. Jones, T. Koi, R. Kokoulin, M. Kossov, H. Kurashige, V. Lara, S. Larsson, F. Lei, O. Link, F. Longo, M. Maire, A. Mantero, B. Mascialino, I. McLaren, P. M. Lorenzo, K. Minamimoto, K. Murakami, P. Nieminen, L. Pandola, S. Parlati, L. Peralta, J. Perl, A. Pfeiffer, M. G. Pia, A. Ribon, P. Rodrigues, G. Russo, S. Sadilov, G. Santin, T. Sasaki, D. Smith, N. Starkov, S. Tanaka, E. Tcherniaev,

B. Tome, A. Trindade, P. Truscott, L. Urban, M. Verderi, A. Walkden, J. P. Wellisch, D. C. Williams, D. Wright, and H. Yoshida, "Geant4 developments and applications," *Nuclear Science, IEEE Transactions on*, vol. 53, no. 1, pp. 270–278, 2006, iD: 1.

34. S. Agostinelli, J. Allison, K. Amako, J. Apostolakis, H. Araujo, P. Arce, M. Asai, D. Axen, S. Banerjee, G. Barrand, F. Behner, L. Bellagamba, J. Boudreau, L. Broglia, A. Brunengo, H. Burkhardt, S. Chauvie, J. Chuma, R. Chytracek, G. Cooperman, G. Cosmo, P. Degtyarenko, A. Dell'Acqua, G. Depaola, D. Dietrich, R. Enami, A. Feliciello, C. Ferguson, H. Fesefeldt, G. Folger, F. Foppiano, A. Forti, S. Garelli, S. Giani, R. Giannitrapani, D. Gibin, J. J. G. Cadenas, I. Gonzlez, G. G. Abril, G. Greeniaus, W. Greiner, V. Grichine, A. Grossheim, S. Guatelli, P. Gumplinger, R. Hamatsu, K. Hashimoto, H. Hasui, A. Heikkinen, A. Howard, V. Ivanchenko, A. Johnson, F. W. Jones, J. Kallenbach, N. Kanaya, M. Kawabata, Y. Kawabata, M. Kawaguti, S. Kelner, P. Kent, A. Kimura, T. Kodama, R. Kokoulin, M. Kossov, H. Kurashige, E. Lamanna, T. Lampn, V. Lara, V. Lefebure, F. Lei, M. Liendl, W. Lockman, F. Longo, S. Magni, M. Maire, E. Medernach, K. Minamimoto, P. M. de Freitas, Y. Morita, K. Murakami, M. Nagamatu, R. Nartallo, P. Nieminen, T. Nishimura, K. Ohtsubo, M. Okamura, S. O'Neale, Y. Oohata, K. Paech, J. Perl, A. Pfeiffer, M. G. Pia, F. Ranjard, A. Rybin, S. Sadilov, E. D. Salvo, G. Santin, T. Sasaki, N. Savvas, Y. Sawada, S. Scherer, S. Sei, V. Sirotenko, D. Smith, N. Starkov, H. Stoecker, J. Sulkimo, M. Takahata, S. Tanaka, E. Tcherniaev, E. S. Tehrani, M. Tropeano, P. Truscott, H. Uno, L. Urban, P. Urban, M. Verderi, A. Walkden, W. Wander, H. Weber, J. P. Wellisch, T. Wenaus, D. C. Williams, D. Wright, T. Yamada, H. Yoshida, and D. Zschiesche, "Geant4A Simulation Toolkit," *Nuclear Instruments and Methods in Physics Research Section A: Accelerators, Spectrometers, Detectors and Associated Equipment*, vol. 506, no. 3, pp. 250–303, 7/1 2003.

35. D. B. Pelowitz, "Mcnpx users manual," Los Alamos National Laboratory, Tech. Rep. 2.6.0, 2008. [Online]. Available: http://www.scribd.com/doc/74880584/2-6-0-Users-Manual

36. "(AIDA)– Abstract Interfaces for Data Analysis." [Online]. Available: http://aida.freehep.org/index.thtml

37. W-Ie-Ne-R, "Nimbox NAD4 Manual," *Plein and Baus GmbH*, 2004. [Online]. Available: http://www.wiener-d.com/documents/manuals/Manual_NIMbox_All.pdf

38. National Instruments, "The benefits of programming graphically in ni labview," National Instruments, Tech. Rep., 2002.

39. Adelphi Technology Incorporated, "DD108 Neutron Generator," p. 2. [Online]. Available: http://adelphitech.com/products/dd108.html

40. P.-T. Bundesanstalt, "Umg 3.3- unfolding with maxed and gravel," *ORNL US-DOE*, vol. PSR-529, 2004.

41. M. Reginatto, P. Goldhagen, and S. Neumann, "Spectrum unfolding, sensitivity analysis and propagation of uncertainties with the maximum entropy deconvolution code maxed," *Nuclear Instruments and Methods in Physics Research Section A: Accelerators, Spectrometers, Detectors and Associated Equipment*, vol. 476, pp. 242–246, 2002.

42. M. Shigetaka, T. Hideki, K. Jun, and I. Tetsuo, "Fundamental study on neutron spectrum unfolding using maximum entropy and maximum likelihood method," *Progress in Nuclear Science and Technology*, vol. 1, pp. 233–236, 2011.

43. M. Reginatto and P. Goldhagen, "Maxed, a computer code for the deconvolution of multisphere neutron spectrometer data using the maximum entropy method," *Environmental Measurements Laboratory USDOE*, vol. EML-595, 1998. [Online]. Available: http://www.nbl.doe.gov/htm/EML_Legacy_Website/reports/eml595.pdf

44. Z. Harvey, "Neutron flux and energy characterization of a plutonium-beryllium isotopic neutron source by monte carlo simulation with verification by neutron activation analysis," *UNLV*, 2010.

REPORT DOCUMENTATION PAGE

Form Approved
OMB No. 0704–0188

1. REPORT DATE *(DD–MM–YYYY)*	2. REPORT TYPE	3. DATES COVERED *(From — To)*
21–03–2013	Master's Thesis	Sep 2011 — Mar 2013

4. TITLE AND SUBTITLE

NEUTRON SPECTROSCOPY
USING LiF THIN-FILM DETECTORS

5a. CONTRACT NUMBER

5b. GRANT NUMBER

5c. PROGRAM ELEMENT NUMBER

6. AUTHOR(S)

Ford, Michael, 2d Lt., USAF

5d. PROJECT NUMBER

5e. TASK NUMBER

5f. WORK UNIT NUMBER

7. PERFORMING ORGANIZATION NAME(S) AND ADDRESS(ES)

Air Force Institute of Technology
Graduate School of Engineering and Management (AFIT/ENP)
2950 Hobson Way
WPAFB OH 45433-7765

8. PERFORMING ORGANIZATION REPORT NUMBER

AFIT-ENP-13-M-10

9. SPONSORING / MONITORING AGENCY NAME(S) AND ADDRESS(ES)

Air Force Office of Scientific Research
AFIT Faculty Research Council
2950 Hobson Way
Wright Patterson AFB, OH 45433

10. SPONSOR/MONITOR'S ACRONYM(S)

AFOSR

11. SPONSOR/MONITOR'S REPORT NUMBER(S)

2012-059

12. DISTRIBUTION / AVAILABILITY STATEMENT

APPROVED FOR PUBLIC RELEASE; DISTRIBUTION UNLIMITED.

13. SUPPLEMENTARY NOTES

14. ABSTRACT

A stacked array of segmented micro-structured semiconductor neutron detectors (MSNDs) has been fabricated to perform as a neutron spectrometer simultaneously capable of differentiating fast and thermal neutrons. The MSND devices consist of thin-film perforated diodes constructed from LiF powder back-filled into an etched silicon wafer. Geant4 simulations demonstrate than an eight-layer spectrometer consisting of alternating layers of MSND and hydrogenous moderator can successfully resolve neutron energies at a resolution dependent upon the number of layers and the thickness of the adjacent moderating materials. The simulated spectrometer response was compared to that obtained experimentally with mono-energetic neutrons from a D+D neutron generator. The commissioning tests of the spectrometer reveal that the energy of a mono-energetic neutron source can be identified to within ± 1 MeV. Following the commissioning tests, the spectrometer was used to characterize the poly-energetic neutron spectrum of a plutonium-beryllium neutron source.

15. SUBJECT TERMS

Neutron, Detection, Spectroscopy, Spectrometer

16. SECURITY CLASSIFICATION OF:			17. LIMITATION OF ABSTRACT	18. NUMBER OF PAGES	19a. NAME OF RESPONSIBLE PERSON
a. REPORT	b. ABSTRACT	c. THIS PAGE			LTC Stephen R. McHale, AFIT/ENP
U	U	U	UU	137	19b. TELEPHONE NUMBER *(include area code)* (937) 255-3636, x4438; stephen.mchale@afit.edu